# Coastal and Offshore Science and Engineering

an International
open-access Journal

7/2025
ISSN 2785-7972

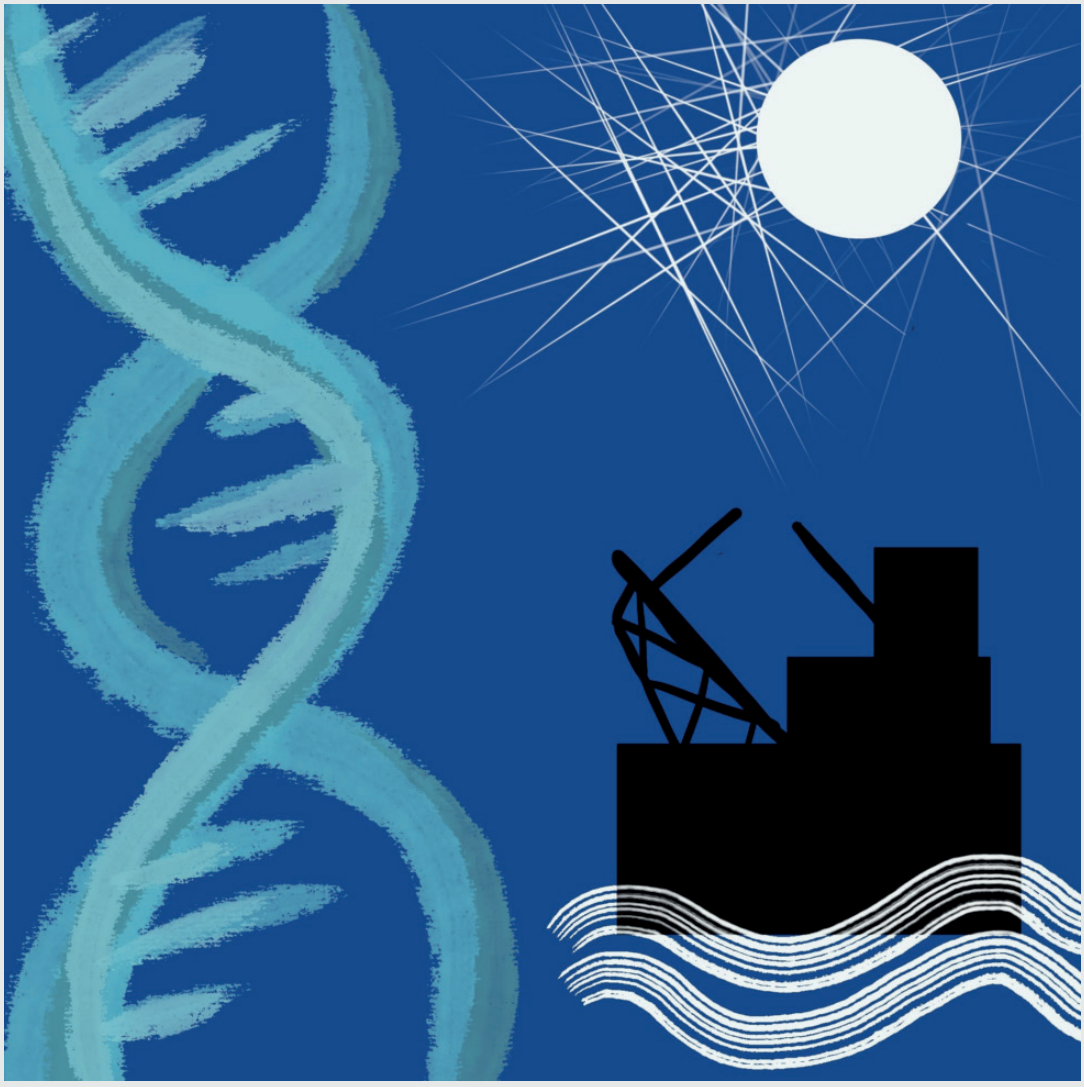

STUDiUM EDiTORE

eCAMPUS UNIVERSITÀ

eCAMPUS UNIVERSITY PRESS

# COSE

## COASTAL AND OFFSHORE SCIENCE AND ENGINEERING

An International open-access Journal

**Year IV - VOL. 7 - 2025**

ISSN : 2785-7972

Coastal and Offshore Science and Engineering is an internationally peerreviewed open access journal of coastal science and engineering published every 6 months online by STUDIUM. Readers of the Journal include engineers, geologists, ecologists, geographers, oceanographers, scholars and specialists who interest in coastal development, ecology, management and protection. The Journal provides new insights on coastal, port and offshore processes, function, design, performance, management, monitoring and restoration from an integrated, multi-/inter- disciplinary, multi-trophic and sustainable perspective. Coastal and Offshore Science and Engineering welcomes research and field case papers based on a wide range of topics by means of field, laboratory and experimental campaigns and remote sensing technology as well as mathematical and numerical modeling. The purpose is to encourage the development and application of holistic initiatives and novel concepts, methods, models and technologies; to elucidate the impact of multiple stressors (climate change, invasive species); to enhance knowledge about the engineering, geology and ecology and integrity of the coastal and offshore systems.

# INDEX

# Frontiers in Coastal Hydrodynamics, Advanced Numerical Modelling, and Multi-Scale Experimental Analysis

Volume I-2025 of Coastal and Ocean Science and Engineering (COSE*)* brings together five cutting-edge contributions that collectively reflect the evolution of coastal and ocean engineering towards increasingly integrated, data-driven, and physics-informed approaches.

The five contributions included in this Volume were originally presented at the 11th edition of the Short Course/Conference on Applied Coastal Research (SCACR), held in Dubrovnik, Croatia, from 24 to 26 September 2025. SCACR events are designed to promote the exchange of state-of-the-art advances in coastal and port engineering by combining scientific knowledge, methodological innovation, and practical application. Bringing together MSc and PhD students, experimental and field researchers, theorists, and numerical modellers, SCACR has become a vibrant hub for the global coastal and marine engineering community.

This Special Issue captures a significant moment for the discipline: advanced computational models are converging with high-fidelity hydraulic experiments, enabling researchers to explore coastal processes with a level of detail, accuracy, and scalability that would have been unthinkable only a decade ago.

The articles gathered here illustrate how the field is moving beyond traditional paradigms—such as purely empirical design rules or isolated laboratory testing—towards unified frameworks that combine nonlinear wave dynamics, multidirectional wave decomposition, fully three-dimensional sediment morphodynamics, phase-resolving diffraction modelling, and rigid-body simulations of large armour units. Together, these studies represent a decisive step towards predictive coastal engineering supported by multiphysics models and validated through rigorous experimentation.

What emerges is a clear vision of the future of coastal science: a discipline in which hydraulic laboratories, numerical wave basins, and high-performance computing environments operate in synergy, continuously exchanging data, validation, and conceptual advances.

This editorial provides an overview of the scientific contributions of each paper and highlights the broader transformations they collectively signal for the field.

## 1. Advances in Hydraulic Model Testing: Towards High-Resolution Physical Insight

The opening contribution by Andersen, Eldrup, and Iversen revisits the foundations of hydraulic physical modelling with renewed emphasis on precision, reproducibility, and experimental fidelity. The paper synthesises recent developments in wave generation, absorption techniques, instrumentation, calibration procedures, and uncertainty quantification.

The authors describe state-of-the-art approaches for generating highly controlled multidirectional wave fields and highlight advances in active and passive absorption systems, modern wave-gauge configurations, non-intrusive measurement techniques, and the integration of physical models with real-time numerical support tools.

Their work underscores a central message: physical modelling is not being replaced by numerical modelling—rather, it is being strengthened, refined, and integrated with it. This hybrid perspective establishes the conceptual foundation for the subsequent contributions in this Volume.

## 2. Multidirectional Nonlinear Wave Decomposition: From Theory to Experimental Validation

Iversen et al. present one of the most technically sophisticated contributions of the Volume: the first experimental validation of the NL-SORS (Nonlinear Single-Summation Oblique Reflection Separation) method, a significant advancement in wave-field analysis for short-crested, nonlinear sea states.

Although methods for separating incident and reflected wave fields have long existed for long-crested or linear conditions, the decomposition of nonlinear multidirectional waves has remained a persistent challenge. The NL-SORS method addresses this gap through a robust frequency-domain least-squares framework capable of estimating incident, reflected, bound, and free wave components with high stability.

This contribution is particularly notable for:

- Demonstrating the method using physical rather than synthetic data;
- Establishing robustness across varying degrees of directional spreading and nonlinearity;
- Enabling reconstruction of full three-dimensional directional spectra and wave trains.

The study represents a major step forward for physical modelling facilities, which increasingly require accurate wave-field decomposition in order to relate structural response to truly incident wave conditions.

## 3. High-Fidelity Modelling of Local Scour Around Circular Structures

Ebrahimi, Wang and Bihs present a detailed and rigorous investigation of local scour using the open-source REEF3D CFD framework. The study stands out for its implementation of:

- Fully three-dimensional RANS modelling;
- Dynamic free-surface capture using the level-set method;
- A sediment transport module coupled with morphological evolution;
- A direct-forcing immersed boundary method for enhanced numerical stability.

The authors address one of the most fundamental—and notoriously complex—problems in coastal engineering: predicting the formation and temporal evolution of scour holes around piles and piers. By validating the model against experimental data, including scour depth and spatial patterns, the study demonstrates that the enhanced REEF3D implementation reproduces scour geometry with remarkable accuracy.

Beyond its immediate application, the work highlights a broader trend: high-resolution sediment morphodynamics is becoming computationally feasible and increasingly integral to design-level studies.

## 4. Diffraction Modelling with a Three-Dimensional Non-Hydrostatic Solver: Bridging Analytical Theory and Real-World Harbours

Becker, Wang and Bihs provide a comprehensive assessment of wave diffraction around breakwaters using the non-hydrostatic model REEF3D::NHFLOW. The study employs a two-level validation strategy:

1. Analytical benchmarking against the classical Sommerfeld solution, achieving excellent agreement and a very low RMSE (0.012);
2. Application to a real harbour (Sirevåg, Norway), where NHFLOW reveals significantly different wave penetration patterns compared with the spectral model SWAN.

The results demonstrate that phase-resolving models provide fundamentally different—and in many cases more physically realistic—insights into wave propagation within harbour basins, particularly with regard to energy penetration near openings and the role of diffraction in shaping nearshore wave climates.

The study makes a compelling case for incorporating non-hydrostatic solvers into the design workflow for port engineering and coastal infrastructure exposed to complex wave fields.

## 5. Coupled CFD–DEM Modelling of Large Armour-Unit Interactions

The final contribution by Larkermani et al. extends numerical modelling into a domain of central importance for breakwater engineering: the simulation of motion, interaction, collision, and stability of individual large armour units.

The authors introduce a high-fidelity CFD–DEM framework integrating:

- A Navier–Stokes solver with high-order WENO discretisation;
- A Direct Forcing Immersed Boundary Method for realistic fluid–solid interaction;
- A multi-level collision detection algorithm;
- Six-degrees-of-freedom rigid-body motion;
- A viscoelastic contact model.

This fully resolved CFD–DEM approach enables the capture of rocking, displacement, interlocking, collision dynamics, and complex rearrangements of armour units under hydrodynamic loading.

The implications are profound: this methodology opens the door to a new generation of breakwater design based not solely on empirical coefficients, but on physically resolved simulations approaching prototype scale.

## Collective Themes and Emerging Directions

Across these five contributions, several unifying themes emerge:

1. *The fusion of experimental and numerical hydrodynamics*

Physical model tests are increasingly complemented by real-time numerical support, advanced wave decomposition techniques, and data-assimilation frameworks.

2. *The rise of open-source, high-fidelity modelling ecosystems*

The REEF3D suite features prominently in four of the five papers, underscoring the growing importance of transparent, reproducible, and community-driven modelling platforms.

3. *A growing focus on nonlinear, multidirectional, and multiphase processes*

Coastal systems are inherently complex—and the tools used to study them now reflect that complexity more faithfully than ever before.

4. *Engineering applications grounded in physics-based understanding*

From scour evolution to harbour wave penetration and armour-unit dynamics, each contribution strengthens design-level capabilities through mechanistic insight.

5. *A shared trajectory towards predictive coastal engineering*

The advances presented here collectively move the discipline towards models that are not merely descriptive, but predictive—capable of anticipating structural performance, morphological evolution, and coastal risk under future conditions.

## Concluding Remarks

Volume I-2025 of COSE, a special issue, offers a compelling snapshot of the intellectual energy currently driving coastal and ocean engineering. It showcases a community committed to methodological rigour, innovation, and openness—and to developing tools and insights that directly support coastal resilience in an era of accelerating environmental change.

It is also noteworthy that all five papers included in this Volume were first presented at SCACR 2025 in Dubrovnik. Their inclusion reflects not only the scientific quality of the event but also its role as an incubator of emerging ideas, interdisciplinary collaboration, and the next generation of coastal engineers. The scientific dialogue fostered at SCACR aligns strongly with the themes highlighted in this Special Issue, reinforcing the importance of community-driven knowledge exchange.

These contributions will undoubtedly serve as reference points for ongoing advances in hydrodynamics, sediment processes, numerical modelling, and coastal infrastructure design.

We hope that readers will find in this Volume both inspiration and practical guidance, and that the work presented here will continue to stimulate scientific dialogue and interdisciplinary collaboration.

*Roberto Tomasicchio*
University of Salento, Italy
*Felice D'Alessandro*
University of Milan, Italy
*Dalibor Carević*
University of Zagreb, Croatia
*Damjan Bujak*
University of Zagreb, Croatia

DOI: https://doi.org/10.53256/COSE_250101

# Recent Advances in Hydraulic Model Testing Techniques

T. Lykke Andersen[a,*], M. R. Eldrup[a] and S. K. Iversen[a]
[a]*Department of the Built Environment, Aalborg University, Denmark*

[*]*Department of the Built Environment, Thomas Manns Vej 23, 9220 Aalborg Ø, Denmark, tla@build.aau.dk*

ABSTRACT: Over the past four decades, numerous hydraulic laboratories capable of generating irregular waves have been established. Most of these facilities employ wave generation and analysis procedures originally developed for linear or mildly nonlinear irregular waves. However, such procedures are often insufficient to accurately reproduce the highly nonlinear wave conditions associated with the design of coastal structures. This paper presents an overview of recent advances in hydraulic model testing techniques that enable the accurate generation and analysis of highly nonlinear irregular waves. The three principal topics addressed are: generation of highly nonlinear waves using piston-type wavemakers combined with cyber-physical modelling; active absorption of reflected waves; and analysis of highly nonlinear long-crested and short-crested waves. These methods have already been applied in several commercial and research projects at Aalborg University. Their practical implementation and performance are demonstrated through selected examples presented in this paper.

KEYWORDS: Nonlinear waves, short-crested waves, wave generation, active absorption, wave analysis, cyber-physical modelling.

## 1 INTRODUCTION

Coastal structures are frequently designed for wave conditions in which the significant wave height at the structure toe is large relative to the local water depth. In many cases, this ratio approaches the depth-limited condition, implying that waves are strongly nonlinear and may break on the foreshore. The degree of nonlinearity increases further when the wavelength, relative to the water depth at the toe, is also large—for example, for waves with long peak periods. Under such conditions, the highest waves become highly asymmetric, exhibiting narrow, steep crests and broad troughs.

The generation and analysis of these waves in physical models cannot be accurately performed using conventional methods based on linear or mildly nonlinear wave theory. Instead, it is essential to apply nonlinear wave generation and analysis techniques to ensure that the modelled waves faithfully represent prototype conditions. This is crucial to avoid unrealistic structural responses caused by spurious free harmonics arising from the application of inappropriate wavemaker theory.

The present paper reviews recent advances in three key areas that are essential for the accurate modelling of nonlinear waves in physical (and numerical) models:

- Generation of highly nonlinear waves in shallow water using piston-type wavemakers;
- Simultaneous active absorption of reflected waves during nonlinear wave generation;
- Analysis of nonlinear waves, including reflection separation.

The current state of the art, including recent developments in these three areas, is presented below. Subsequently, examples demonstrating the application of the proposed methods are provided.

## 2 GENERATION OF HIGHLY NONLINEAR IRREGULAR WAVES

Biésel and Suquet (1951) solved the linear wavemaker problem analytically for various wavemaker types. A second-order solution was presented by Sand (1982) for the subharmonics and later extended to include superharmonics by Sand and Mansard (1986). Schäffer (1993) reformulated the theory in a simplified form and incorporated additional terms to account for interactions caused by evanescent modes. This method was subsequently extended to short-crested waves by Schäffer and Steenberg (2003). Eldrup and Lykke Andersen (2019a) proposed a correction to this approach in order to avoid introducing excessive second-order energy when the theory is applied outside the formal validity range of second-order wave theory.

An ad hoc unified generation theory for highly nonlinear irregular waves in shallow water was proposed by Zhang et al. (2007). In this approach, the wavemaker control signals are determined from input generated by a numerical wave model. The coupling to the physical model is based on shallow-water wave generation theory, supplemented by a dispersive correction derived from linear wavemaker theory. The method was later extended by Yang et al. (2014; 2021) to incorporate second-order coupling effects for long-crested and short-crested waves, respectively.

To avoid the generation of spurious free harmonics, it is essential to apply a wavemaker theory that is valid for the water depth at which the wavemaker is installed. If an inappropriate theory is used, spurious harmonics may be generated and can significantly affect the reproduced wave field, as demonstrated by Schäffer (1993) and Eldrup and Lykke Andersen (2019a). A lower-order wavemaker theory may be applied if the bathymetry is constructed to provide sufficient water depth at the wavemaker. However, if only linear or second-order wavemaker theory is available, a substantial portion of the bathymetry may need to be constructed between the wavemaker and the tested structure—particularly for gently sloping foreshores.

In shorter facilities, such as those at Aalborg University, this is often impractical. In larger facilities, it may be feasible but requires significant construction effort. Consequently, many laboratories have implemented transition slopes to reduce the extent of bathymetry construction. However, Eldrup and Lykke Andersen (2024) demonstrated that transition slopes can introduce unwanted free harmonics, thereby producing effects similar to those observed when linear wavemaker theory is used to generate nonlinear waves. In many cases, it is therefore necessary—or at least preferable—to reproduce highly nonlinear waves directly at the wavemaker using appropriate nonlinear generation techniques and the correct bathymetry between the wavemaker and the model.

The validity range of various wavemaker theories was investigated by Eldrup and Lykke Andersen (2019a). Their findings are presented in the classical Le Méhauté (1976) diagram shown in Fig. 1.

The diagram is plotted assuming $H_{max} = 2H_{m0,}$ and the indicated breaking limitation corresponds to breaking of $H_{max}$. The diagram also includes typical sea states generated at the wavemaker in coastal engineering projects, as listed in Table 1. In this example, the water depth at the wavemaker *(h)* is selected such that the spectral wave height corresponds to 30% of the local depth. This is a commonly applied criterion and ensures that wave breaking does not occur at the wavemaker.

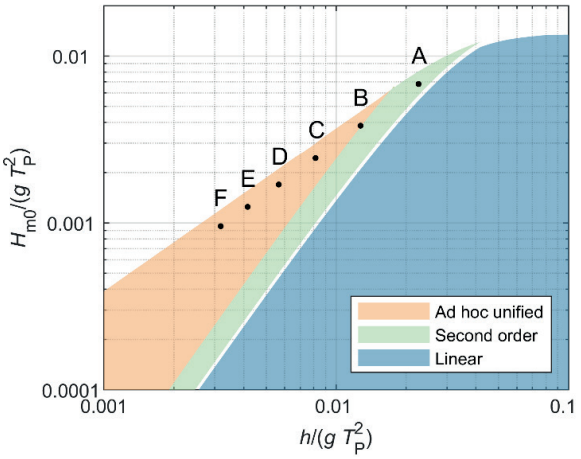


Figure 1. Validity ranges of wavemaker theories according to the limits provided by Eldrup and Lykke Andersen (2019a).

Fig. 1 shows that second-order wavemaker theory is sufficient for sea state A. Sea state B lies only marginally outside the second-order validity range. For the remaining sea states, the ad hoc unified generation method is required. This indicates that, for accurate wave generation in coastal engineering projects, either a sufficiently long foreshore must be included in the physical model to ensure adequate water depth at the wavemaker, or advanced hybrid wave generation techniques must be employed, combining numerical and physical modelling within a cyber-physical framework.

This cyber-physical modelling approach has been extensively applied at Aalborg University over the past decade for long-crested waves. In the present study, it is also applied to short-crested waves. For short-crested wave generation, the numerical model domain must be significantly larger to prevent the physical wavemaker from being located within a diffraction zone of the numerical model. As a result, the computational effort becomes substantial—even when using Boussinesq-type wave models—particularly for long-duration time series.

Table 1. Typical sea states generated in coastal physical models.

| | Origin | $h$ [m] | $H_{m0}$ [m] | $T_p$ [s] | $\frac{h}{gT_p^2}$ | $\frac{H_{m0}}{gT_p^2}$ |
|---|---|---|---|---|---|---|
| A | Wind | 18.0 | 5.40 | 9.0 | 0.0227 | 0.0068 |
| B | Wind | 18.0 | 5.40 | 12.0 | 0.0127 | 0.0038 |
| C | Wind | 18.0 | 5.40 | 15.0 | 0.0082 | 0.0024 |
| D | Wind | 18.0 | 5.40 | 18.0 | 0.0057 | 0.0017 |
| E | Swell | 12.5 | 3.75 | 17.5 | 0.0042 | 0.0012 |
| F | Swell | 12.5 | 3.75 | 20.0 | 0.0032 | 0.0010 |

## 3 ACTIVE ABSORPTION

Active absorption consists of applying a correction signal to the wavemaker paddles in order to minimise wave re-reflection at the wavemaker. This is essential when testing structures that produce significant reflections, such as caisson breakwaters or steep rubble-mound breakwaters. Under mildly reflective conditions, the system is primarily used to control long-wave energy, which is difficult to dissipate adequately through passive absorption alone.

Various active absorption systems have been proposed based on measurements of different physical quantities in either the far field or the near field. A comprehensive review of these systems is provided by Schäffer and Klopman (2000).

In the following, only systems based on near-field surface elevation measurements are considered. This type of system is preferred by most hydraulic laboratories because it is relatively simple and can achieve high efficiency over a broad frequency range. In such systems, one or more wave gauges are mounted on each moving paddle, and the measured signals are processed through analogue or digital filters to generate correction signals for the wavemakers.

The pioneering work of Milgram (1965; 1970) demonstrated such a system in a wave flume in which the passive absorber was replaced by an active absorber. Schäffer et al. (1994) presented a similar system to that proposed by Milgram (1965; 1970), but applied it simultaneously with wave generation. The system was subsequently extended by Schäffer and Skourup (1996) to account for wave directionality through the use of a causal two-dimensional infinite impulse response (IIR) filter. Schäffer and Jakobsen (2003) further updated the system to allow active absorption simultaneous with nonlinear wave generation.

Lykke Andersen et al. (2016) proposed a similar system but incorporated into the transfer function the possibility that the wave gauge may be positioned with a gap relative to the moving paddle. They demonstrated that a causal finite impulse response (FIR) filter can be used as an alternative to the IIR filters applied in earlier studies. Furthermore, Lykke Andersen et al. (2018) evaluated the performance of this system for nonlinear waves. The results are presented in Fig. 2 in terms of the re-reflection coefficient of the paddle. The performance curve was established in a wave flume equipped with wavemakers at both ends. The reflection coefficient was determined using the methods described by Lykke Andersen et al. (2017) for regular waves, Lykke Andersen et al. (2019) for bichromatic waves, and Eldrup and Lykke Andersen (2019b) for irregular waves. These methods are described in the following section.

The results demonstrate that, in shallow water, the active absorption system exhibits nearly identical efficiency for bound wave components and free wave components. This applies to superharmonics in regular waves, as well as to both subharmonics and superharmonics in bichromatic waves. A similar behaviour was verified for the second-order superharmonic peak in highly nonlinear irregular waves.

Some deviations from the theoretical curve based on linear wavemaker theory are observed in Fig. 2 in the frequency range 1.0–1.3 Hz. During these tests, cross-mode activity was observed, which influenced both the active absorption performance and the reflection analysis results.

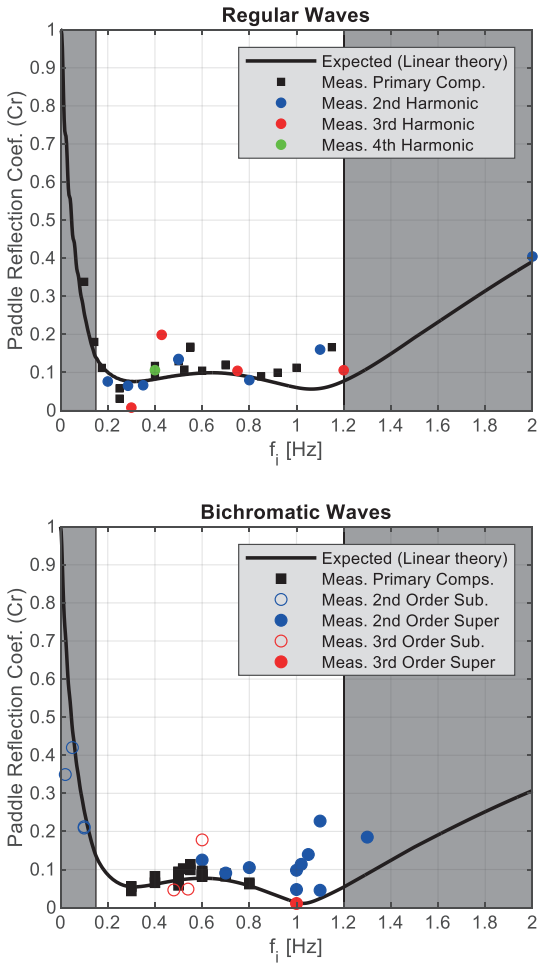


Figure 2. Measured reflection coefficient of the absorbing paddle compared with the theoretical curve based on linear wavemaker theory.

## 4 SEPARATION OF INCIDENT AND REFLECTED WAVES

A key aspect of physical modelling is the determination of the incident wave field present in the facility. The separation of waves into incident and reflected components requires both a mathematical description of the surface elevation and an appropriate solution procedure. Traditionally, the applied mathematical models have been based on linear wave theory; however, more recently, methods valid for nonlinear waves have been proposed.

Historically, different approaches have been applied to long-crested and short-crested waves, and they are therefore described separately below. Nevertheless, recent developments have introduced methods for short-crested waves that are founded on the same principles as state-of-the-art approaches for long-crested waves.

### 4.1 *Long-crested waves*

The separation of long-crested waves into incident and reflected components has traditionally been based on measurements of surface elevations at multiple locations. Most established methods rely on linear wave theory and assume a horizontal seabed. Representative approaches include the two-gauge method of Goda and Suzuki (1976), the three-gauge method of Mansard and Funke (1986), and the generalised method for an arbitrary number of gauges proposed by Zelt and Skjelbreia (1992).

However, waves under design conditions for coastal structures are typically highly nonlinear, as illustrated in Fig. 1 for the wavemaker location. At the toe of the structure, the degree of nonlinearity is even greater, and waves may also be breaking. Under such conditions, separation methods based on linear wave assumptions may lead to inaccurate results.

More recently, separation methods based on nonlinear wave assumptions have been proposed, including those by Figueres and Medina (2004) and Eldrup and Lykke Andersen (2019b). The latter demonstrated that their nonlinear method outperforms both traditional linear methods and the approach proposed by Figueres and Medina (2004).

The method by Eldrup and Lykke Andersen (2019b) employs different mathematical representations of the wave field in the subharmonic, primary, and superharmonic frequency regions. In the subharmonic and superharmonic regions, both bound and free wave components are included. These components propagate with different celerities and can therefore be separated using measurements from a multi-gauge array. The only exception occurs in extremely shallow water, where bound and free components have nearly identical celerities, making reliable separation difficult.

Ridder et al. (2023) proposed a minor modification to this method to improve the assessment of when reliable separation of bound and free components is feasible and when the mathematical model should be simplified to include only one of the two components.

Lykke Andersen and Eldrup (2021) extended the mathematical formulation to account for the shoaling of nonlinear regular waves. However, Lykke Andersen and Eldrup (2024) showed that the complex shoaling behaviour of nonlinear irregular waves makes it challenging to extend the method to irregular waves propagating over sloping foreshores. In cases involving steep foreshores, it may therefore be necessary to calibrate the waves without the structure in place.

A similar approach may be required when significant wave breaking occurs.

### 4.2 *Short-crested waves*

For short-crested waves, the traditional objective has been to determine the directional spectrum from measured cross-spectra obtained using an array of wave gauges. In practice, only a limited number of gauges are typically available, and therefore additional assumptions must be introduced into the mathematical model.

For example, in the BDM method proposed by Hashimoto and Kobune (1988), it is assumed that the directional spreading function is continuous and smooth, and that no phase-locked reflections are present. In contrast, the MLM method by Isobe and Kondo (1984) assumes that the spreading function follows a $\cos^2 s$ distribution and that phase-locked reflections occur from a known reflection line. A common limitation of all cross-spectral methods is that they cannot provide the incident wave time series, which is often of primary interest in physical modelling applications.

An alternative class of methods exploits the fact that most hydraulic laboratories generate waves using the single summation method. Under this approach, only one primary component is present at each frequency. The directions of these individual primary components are defined in the wave generation software such that the overall directional spreading function satisfies the target specification.

The first method to utilise this information in wave analysis was the linear approach proposed by Draycott et al. (2016). However, its applicability is limited by the assumption that the reflected wave direction is directly opposite to the incident direction. To overcome this limitation, Iversen et al. (2024) developed the SORS method, which allows arbitrary reflection directions for each component.

More recently, Iversen et al. (2025a) extended this approach to nonlinear waves, building on the same principles as the method by Eldrup and Lykke Andersen (2019b). A significant advantage of the resulting NL-SORS method is that it enables reconstruction of both incident and reflected time series for nonlinear short-crested waves.

The method assumes that the primary incident directional spectrum is narrow-banded in both frequency and direction, which permits accurate estimation of bound harmonics. Iversen et al. (2025a) quantified the errors associated with cases that do not fully satisfy this assumption. They found that errors in the superharmonic region are generally small, whereas errors in the subharmonic region may be more significant.

## 5 APPLICATION OF METHODS FOR SHORT-CRESTED WAVES ON A MILDLY SLOPING FORESHORE

The generation of highly nonlinear waves with simultaneous active absorption is demonstrated using the cases listed in Table 1 for which ad hoc unified generation is required, cf. Fig. 1. Cases C and D were reproduced at a Froude scale of 1:36, whereas cases E and F were reproduced at a Froude scale of 1:25. In the numerical model, a 1:80 foreshore slope was applied for all cases. The mean wave direction ($\theta_0$) was perpendicular to the wavemaker in all tests. A directional spreading function of the form $\cos^{2s}(\theta)$ was adopted with s = 50 for all cases. In addition, for sea states C and D, simulations were also performed with s = 15. The frequency spectrum was defined by a JONSWAP spectrum with a peak enhancement factor $\gamma$ = 3.3. Table 2 summarises the test conditions in model scale. The input wave height in the numerical model was iteratively adjusted until the target wave height reported in Table 2 was achieved at the interface between the numerical and physical models. A similar iterative adjustment was not performed for the directional spreading parameter. Consequently, the s-values reported in the table correspond to those defined at the generation line in the numerical model. Due to wave refraction within the numerical domain, the spreading at the interface between the numerical and physical models is reduced (i.e. higher effective s-values).

Each test series had a repeat period of 327.68 s, corresponding to $2^{14}$ data points at a sampling frequency of 50 Hz. The total test duration was set to 390 s to allow for a 10 s ramp-up period, a 10 s ramp-down period, and sufficient time for the establishment of a steady wave field.

Table 2. Test cases with short-crested waves (model scale).

| | $h$ [m] | $H_{m0}$ [m] | $T_p$ [s] | $\theta_0$ [°] | $s$ [-] |
|---|---|---|---|---|---|
| C1 | 0.50 | 0.15 | 2.5 | 0 | 15 |
| D1 | 0.50 | 0.15 | 3.0 | 0 | 15 |
| C2 | 0.50 | 0.15 | 2.5 | 0 | 50 |
| D2 | 0.50 | 0.15 | 3.0 | 0 | 50 |
| E2 | 0.50 | 0.15 | 3.5 | 0 | 50 |
| F2 | 0.50 | 0.15 | 4.0 | 0 | 50 |

## 5.1 *Numerical Model*

The numerical model applied in the cyber-physical modelling framework was the Celeris model developed by Tavakkol and Lynett (2017), modified to incorporate a wave-generating boundary condition with time-series input prescribed at each boundary grid point. This modification enabled second-order wave generation to be applied, thereby significantly reducing the required computational domain compared to linear wave generation. In addition, the sponge-layer formulation was refined to improve absorption efficiency. The numerical model layout is illustrated in Fig. 3.

The spatial discretisation of the numerical model consisted of 50 grid cells per $L_{min}$ in the x-direction (perpendicular to the wave-generating boundary) and 35 grid cells per $L_{min}$ in the y-direction, where $L_{min}$ denotes the linear wavelength in the shallowest part of the model corresponding to the highest primary frequency generated. The temporal discretisation was determined based on a Courant–Friedrichs–Lewy (CFL) number of 0.1.

The sponge layer comprised 900 grid cells at the rear boundary and 700 grid cells along the side boundaries. The length of the 1:80 foreshore slope was selected such that the water depth at the wave-generating boundary satisfied the validity criteria for second-order wavemaker theory, as defined by Eldrup and Lykke Andersen (2019a). Consequently, the slope length was shortest for cases C1 and C2 and longest for case F2. The 1:80 slope terminates at the mean position of the physical wavemaker and is followed by a horizontal plateau, consistent with the configuration in the physical model.

The domain width was selected to minimise diffraction effects. Specifically, the lateral distance from the physical model side wall to the numerical model sponge layer was set to either 3.5 or 5.0 times the distance between the numerical and physical generation boundaries (denoted $x_1$ in Fig. 3). The larger factor was applied for cases C1 and D1, while the smaller factor was used for the remaining cases. As a result, the numerical domain width exceeded its length in all simulations.

The primary spectral components were generated using the single-summation method, which enables application of the NL-SORS method described by Iversen et al. (2025a). The direction of each primary component was selected randomly in accordance with the prescribed directional spreading function.

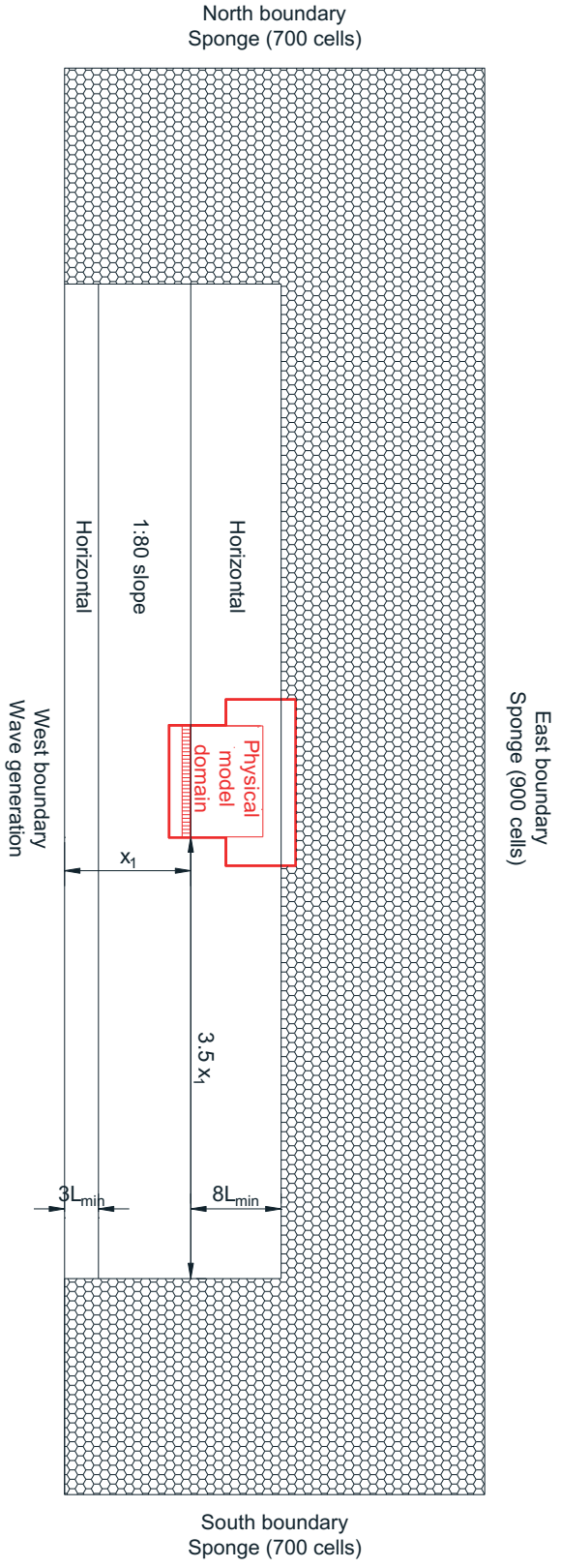


Figure 3. Numerical model layout and location of the physical wave basin and wavemaker (shown in red). The layout is shown to scale for Test C2.

## 5.2 *Physical Model*

The coupling between the numerical model and the physical model boundary was implemented using the linear coupling approach proposed by Zhang et al. (2007). The improved coupling method suggested by Yang et al. (2021) was not applied in the present study.

Corner reflection was not incorporated in the setup. Consequently, diffraction and reflection zones are expected to develop near the sidewalls (cf. Dalrymple, 1989). To minimise their influence on the analysis, the wave gauge array was positioned close to the wavemaker, yet outside the region affected by significant near-field disturbances. Specifically, the first gauge was located at a distance of three water depths from the mean position of the wavemaker. The array consisted of 11 gauges arranged in accordance with the configuration recommended by Iversen et al. (2025a). In addition, 26 supplementary gauges were installed to provide a more detailed characterisation of the wave field.

The bathymetry in the physical model was horizontal. Although this does not represent a typical coastal configuration, it was selected to avoid the need for constructing a sloping bathymetry for validation purposes and to satisfy the constant-depth assumption required by the method of Iversen et al. (2025a). Given the mild slope applied in the numerical model, the horizontal bathymetry in the physical model is not expected to result in significant release of spurious free harmonics.

The experiments were conducted in the Ocean and Coastal Engineering Basin at Aalborg University. The wavemaker is 13 m long and consists of 30 vertically hinged paddle segments. The basin is equipped with efficient passive absorption along the rear wall and portions of the sidewalls. Figures 4 and 5 present the physical model layout and the configuration of the wave gauge positions.

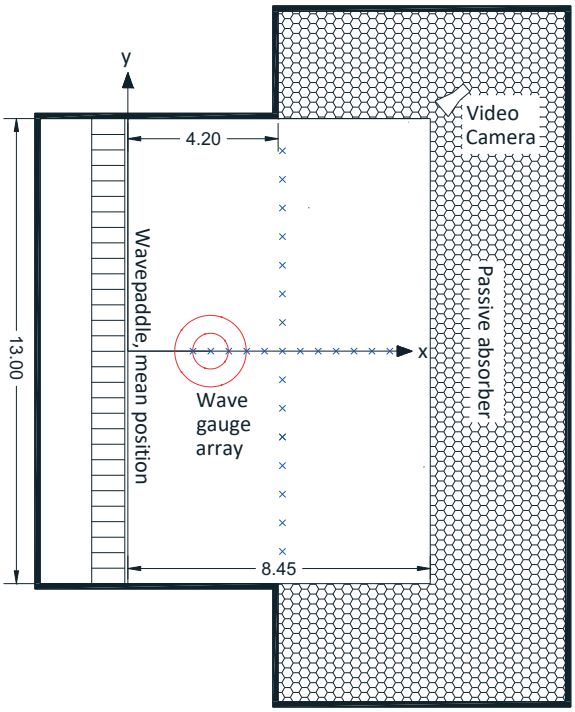


Figure 4. Physical model layout. The NL-SORS array is shown in red (see details in Fig. 5), and the additional 26 gauges are shown in blue, spaced at 0.5 m in the x-direction and 0.8 m in the y-direction.

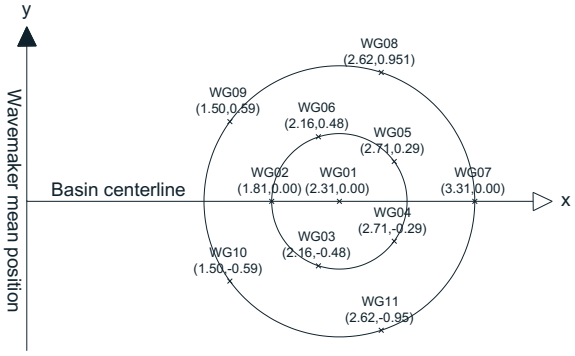


Figure 5. Configuration of the applied wave gauge array. Inner diameter: 1 m; outer diameter: 2m.

### 5.3 *Results*

Fig. 6 presents a qualitative comparison of the wave field within the basin domain in both the numerical and physical models for sea state F2, which represents the most nonlinear condition (cf. Table 2). The snapshot corresponds to the occurrence of one of the highest waves at the centre of the basin, characterised by a narrow, high crest and a wide trough. Due to the long wave periods, significant refraction occurs in the numerical model, resulting in reduced directional spreading as the waves propagate into the physical domain. In the physical model, minor disturbances caused by the passive rear-wall absorber are visible ahead of the wave.

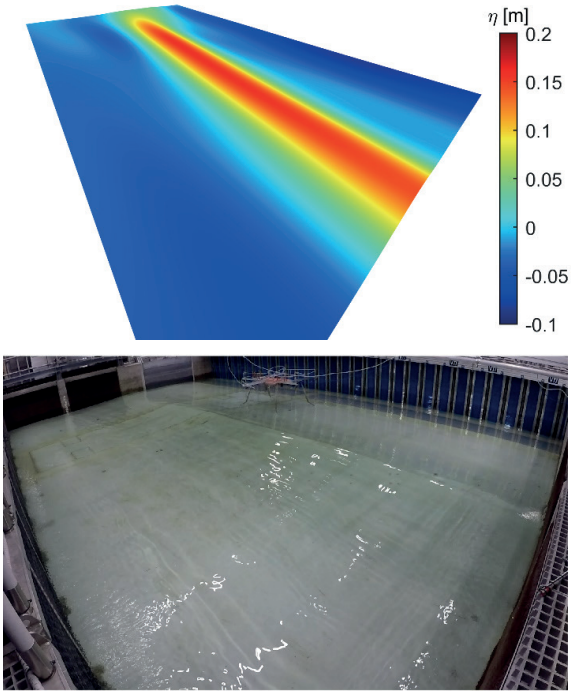


Figure 6. Qualitative comparison of the wave field at the instant corresponding to one of the highest waves in sea state F2 at the centre of the basin. Numerical results are shown for the same area as the physical domain. Camera location as indicated in Fig. 4.

Figure 7 shows the corresponding simulated and measured surface elevations at the same instant for the additional 26 gauges.
The results indicate that the numerical wave field has been reproduced with high fidelity in the physical model for this case.

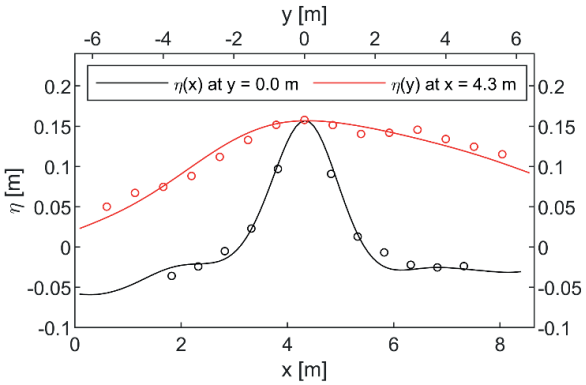


Figure 7. Quantitative comparison corresponding to the instance shown in Fig. 6. Solid lines denote numerical results; circles denote physical measurements.

Figures 8 and 9 present a similar comparison for sea state C1 during one of the largest waves. Sea state C1 has the shortest wave period and the largest directional spreading, making the short-crested characteristics more apparent. Owing to the large directional spreading and the absence of corner reflection, discrepancies increase with distance from the wavemaker, particularly near the sidewalls. Nevertheless, both qualitative and quantitative comparisons demonstrate satisfactory agreement, considering the substantial directional spreading applied in this case.

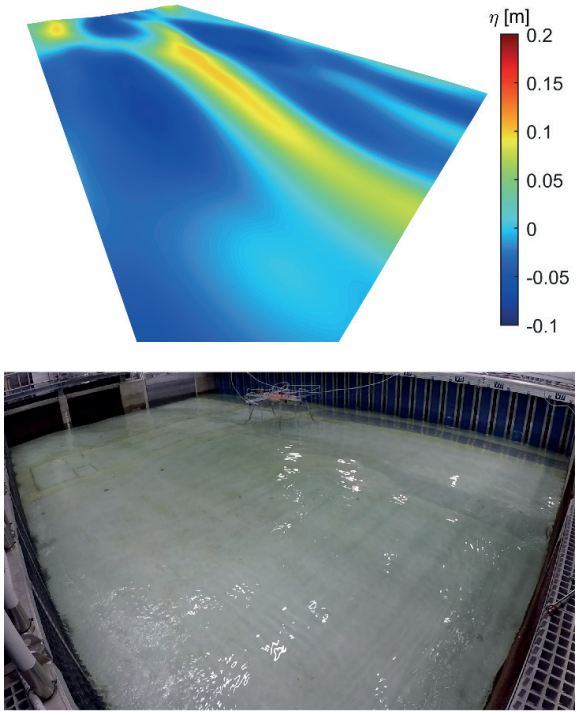


Figure 8. Similar to Fig. 6, but for case C1.

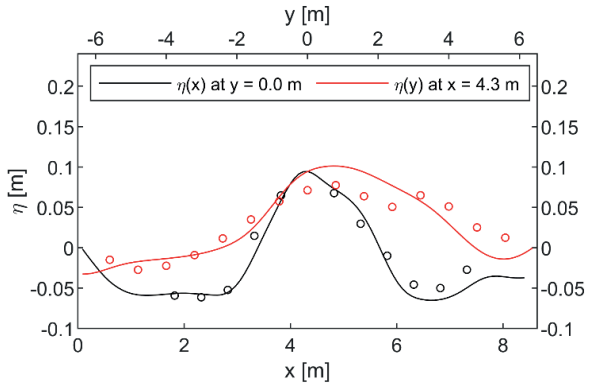


Figure 9. Quantitative comparison corresponding to the instance shown in Fig. 8.

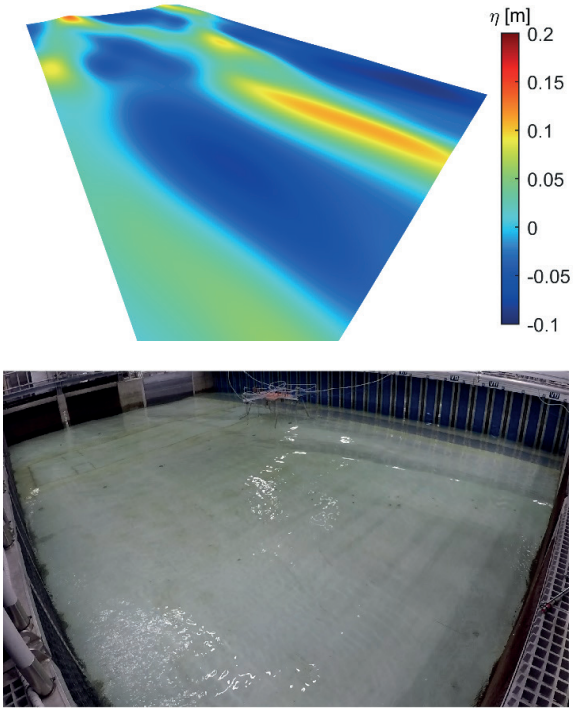


Figure 10. Similar to Fig. 10, but at a random instant with a more directionally spread wave field.

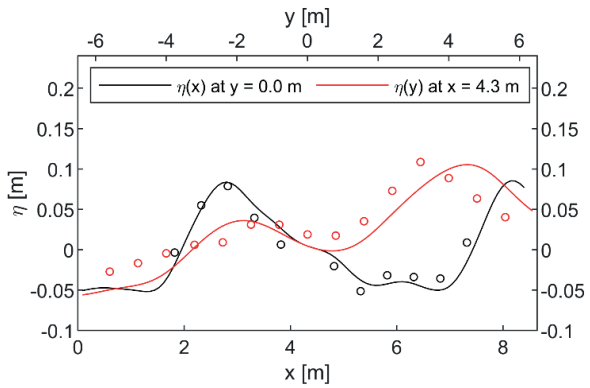


Figure 11. Quantitative comparison corresponding to the instance shown in Fig. 10.

Figures 10 and 11 show the same test case (C1), but at a randomly selected instant characterised by a more pronounced directional spreading of the wave field.

Again, good agreement is observed, particularly near the wavemaker and at the centre of the basin. The accuracy of the coupling between the numerical and physical models was further evaluated through comparison of time series measured at the centre of the circular gauge array, located 2.3 m from the midpoint of the wavemaker. This position is minimally affected by diffraction and reflection from the sidewalls. Figures 12 and 13 present the comparison at the instant of the highest wave in each tested sea state, representing cases with large and small directional spreading, respectively. The time series shown include: (i) the numerically modelled target signal, (ii) the total measured signal in the physical model, and (iii) the incident signal in the physical model obtained using the method of Iversen et al. (2025a). Additional details of this analysis are provided in Iversen et al. (2025b).

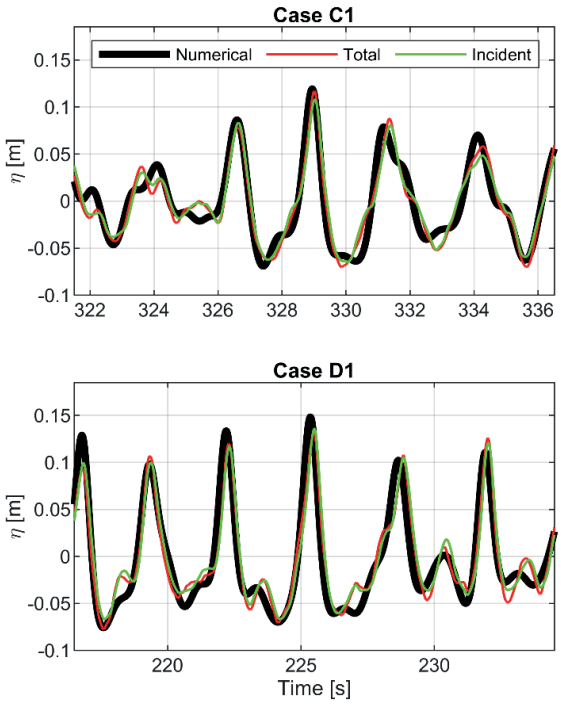


Figure 12. Comparison of time series from the numerical model (black) and physical model (red and green) at the central gauge of the array (WG01) for cases with large directional spreading.

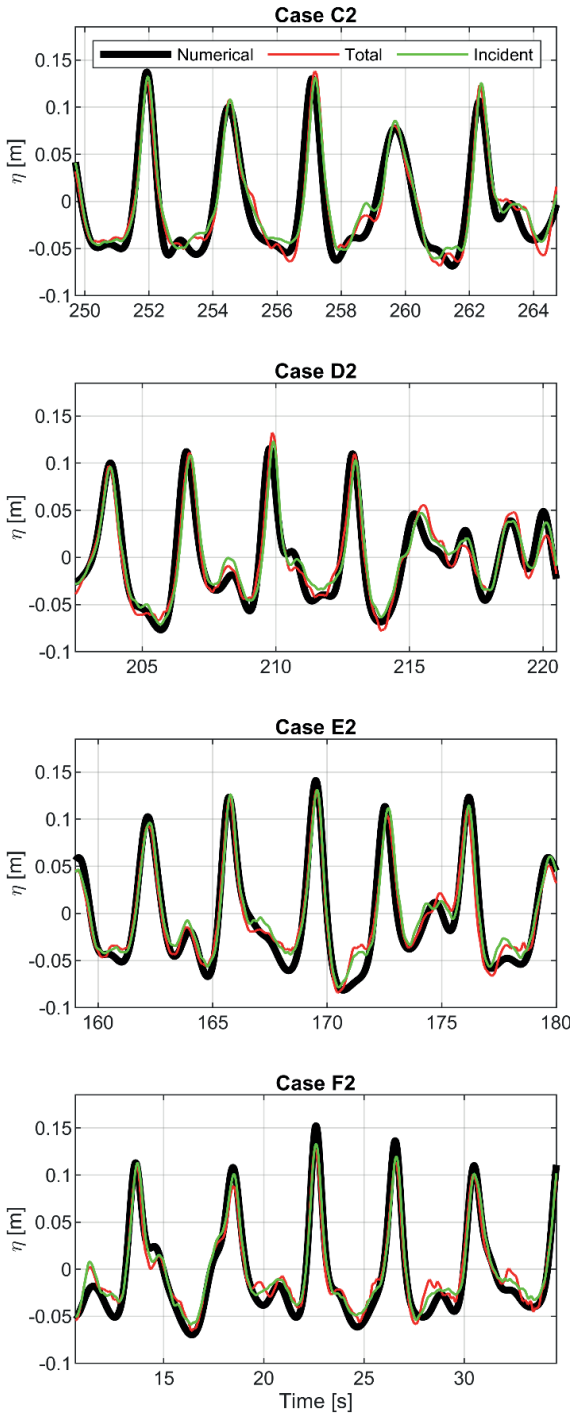


Figure 13. Same as Fig. 12, but for cases with small spreading.

The results demonstrate that it has been possible to shoal the waves in the numerical model into highly nonlinear short-crested conditions and to reproduce them in the physical model using the ad hoc unified generation method. The generated waves exhibit the expected nonlinear characteristics, namely narrow and elevated crests combined with wider and shallower troughs. When compared with the numerical target signals, only minor discrepancies are observed. Such differences are expected due to factors such as leakage beneath and between wavemaker paddles and residual reflections. As a consequence of this leakage, the generated wave heights are approximately 10% lower than the target values, which also leads to the generation of small-amplitude free-wave components. In practice, such leakage effects are typically compensated for during wave generation; however, in the present study, the theoretical transfer function was applied without additional correction. Reflected components were removed from the total measured signal using the method of Iversen et al. (2025a). A detailed analysis of the incident wave components for the present tests is reported in Iversen et al. (2025b).

## 6 CONCLUSIONS

This paper presents three recent developments aimed at ensuring accurate generation and analysis of highly nonlinear waves in the wave basin at Aalborg University. The results demonstrate that these methods are applicable to a wide range of coastal engineering projects. Together, they enable faithful reproduction of prototype nonlinear wave conditions and allow detailed and reliable analysis of the generated wave field.

Waves generation is achieved through a hybrid (cyber-physical) modelling approach that combines numerical and physical modelling. In the present study, a Boussinesq-type numerical model was employed; however, the developed interface to the AwaSys software enables the use of alternative numerical models where appropriate. Wave analysis is performed using the innovative NL-SORS method, which permits separation of bound and free components in nonlinear short-crested waves generated by the single-summation method. This represents a significant advancement in the analysis of complex wave fields in physical model facilities.

The application of the proposed methods was demonstrated through test cases involving nonlinear waves propagating over a simplified foreshore. The results confirm the accuracy of the coupling between the numerical and physical models, as well as the reliability of the analysis procedure. The NL-SORS analysis method and the nonlinear short-crested wave generation procedure are expected to be implemented in the WaveLab and AwaSys software packages developed at Aalborg University.

## ACKNOWLEDGEMENTS

This research did not receive any specific grant from funding agencies in the public, commercial, or not-for-profit sectors.

## REFERENCES

Biésel, F. and Suquet, F. (1951). Les Appareils generateurs de Houle en Laboratoire. *La Houille Blanche, Vol. 6, nos. 2,4 et 5.*

Dalrymple, R.A. (1989). Directional wavemaker theory with sidewall reflection. *Journal of Hydraulic Research, Vol. 27, No.1*, pp. 23-34.

Draycott, S., Davey, T., Ingram, D.M., Day, A., Johanning, L., 2016. The spair method: Isolating incident and reflected directional wave spectra in multidirectional wave basins. *Coastal Engineering, Vol. 114*, pp. 265-283.

Eldrup, M.R. and Lykke Andersen, T. (2019a). Applicability of Nonlinear Wavemaker Theory. *Journal of Marine Science and Engineering, Vol. 7, Special Issue "Selected Papers from Coastlab18 Conference"*

Eldrup, M. R. and Lykke Andersen, T. (2019b). Estimation of Incident and Reflected Wave Trains in Highly Nonlinear Two-Dimensional Irregular Waves. *Journal of Waterway, Port, Coastal, and Ocean Engineering, Vol. 145, Issue 1 (January 2019).*

Eldrup, M. R. and Lykke Andersen, T. (2024). Generation of Highly Nonlinear Waves in a Short Wave Flume. *CoastLab24, Delft, The Netherlands*.

Figueres, M. and Medina, J. R. (2004). Estimating incident and reflected waves using a fully nonlinear wave model. *In Vol. 4 of Coastal Engineering 2004, edited by J. M. Smith, 594–603. Singapore: World Scientific*.

Goda, Y. and Suzuki, Y. (1976). Estimation of incident and reflected waves in random wave experiments. *Proceedings of the 15th Coastal Engineering Conference*, 828‑845.

Hashimoto, N. and Kobune, K. (1988). Directional spectrum estimation from a bayesian approach. *Coastal Engineering Proceedings 1(21),4*, pp. 62–76.

Isobe, M. and Kondo, K. (1984). Method for estimating directional wave spectrum in incident and reflected wave field. *Coastal Engineering* , pp. 467–483.

Iversen, S. K., Lykke Andersen, T. and Frigaard, P. (2024). Directional Spectrum Estimation for Sea States Generated by the Single Summation Method. *Journal of Coastal and Hydraulic Structures, Vol. 4, 15.*

Iversen, S. K., Eldrup, M.R., Lykke Andersen, T. and Frigaard, P. (2025a). The NL-SORS Method for Separation of Nonlinear Multidirectional Waves into Incident and Reflected Wave Trains. *Coastal Engineering, Elsevier.*

Iversen, S. K., Lykke Andersen, T., Alfaro Corrales, F. and Eldrup, M.R. (2025b). Directional Decomposition of Experimental Data with Nonlinear Short-Crested Waves Using the NL-SORS Method. *Coastal and Offshore Science and Engineering - SCACR 2025 special issue.*

Le Méhauté (1976). *An Introduction to Hydrodynamics and Water Waves*. Springer Science & Business Media.

Lykke Andersen, T., Clavero, M., Frigaard, P., Losada, M., Puyol, J. I. (2016). A new active absorption system and its performance to linear and non-linear waves. *Coastal Engineering, Vol.114, August 2016,* Pages 47–60.

Lykke Andersen, T., Eldrup, M. R., Frigaard, P. (2017). Estimation of incident and reflected components in highly nonlinear regular waves. *Coastal Engineering, Vol. 117,* pp. 51-64.

Lykke Andersen, T., Clavero, M., Eldrup, M. R., Frigaard, P., Losada, M. (2018). Active Absorption of Nonlinear Irregular Waves. *Proceedings of the 36th International Conference on Coastal Engineering (ICCE), Baltimore, USA.*

Lykke Andersen, T., Eldrup, M.R., Clavero, M. (2019). Separation of Long-Crested Nonlinear Bichromatic Waves into Incident and Reflected Components. *Journal of Marine Science and Engineering, Vol. 7, Special Issue "Selected Papers from Coastlab18 Conference"*

Lykke Andersen, T. and Eldrup, M. R. (2021). Estimation of incident and reflected components in nonlinear regular waves over sloping foreshores. *Coastal Engineering, Vol. 169.*

Lykke Andersen, T. and Eldrup, M. R. (2024). Applicability of Reflection Separation Algorithms to Nonlinear Irregular Waves over Sloping Foreshores. *CoastLab24, Delft, The Netherlands.*

Mansard, E.P.D. and Funke, E.R. (1980). The measurement of incident and reflected spectra using a least squares method. *Proceedings of the 17th Coastal Engineering Conference*: 154-172.

Milgram, J. H. (1965). Compliant Water Wave Absorbers. *M.I.T. Department of Naval Architecture and Marine Engineering Report no. 65–13*.

Milgram, J. H. (1970). Active water-wave absorbers. *Journal of Fluid Mechanics, Vol. 43, Issue 4,* pp. 845-859.

Ridder, M.P.D,, Kramer, J., Bieman, J.P.D. and Wenneker, I. (2023). Validation and practical application of nonlinear wave decomposition methods for irregular waves. *Coastal Engineering, Vol. 183*.

Sand. S. E. (1982). Long wave problems in Laboratory Models. *Journal of the Waterway, Port, Coastal and Ocean Division, Vol. 108, Issue 4,* pp. 492-503.

Sand, S. E. and Mansard, E.P.D. (1986). Reproduction of Higher Harmonics in Irregular Waves. *Ocean Engineering, Vol. 13, No. 1,* pp. 57-83.

Schäffer, H. A. (1993). Laboratory Wave Generation Correct to Second Order. *Wave Kinematics and Environmental Forces: Papers Presented at a Conference Organized by the Society for Underwater Technology and Held in London, U.K., 24–25 March 1993; Springer: Dordrecht, The Netherlands, 1993;* pp. 115–139.

Schäffer, H. A., Stolborg, T. and Hyllested, P. (1994). Simultaneous Generation and Active Absorption of Waves in Flumes, *International Symposium: Waves – Physical and Numerical Modelling, University of British Columbia, Vancouver, Canada.*

Schäffer, H. A. and Skourup, J. (1996). Active Absorption of Multidirectional Waves, *Proc., 25th Int. Conf. on Coastal Engineering, ASCE, New York.*

Schäffer, H. A. and Klopman, G. (2000). Review of Multidirectional Active Wave Absorption Methods.

*Journal of Waterway, Port, Coastal and Ocean Engineering, Vol. 126, Issue 2*, pp. 88-97.
Schäffer, H. A. and Steenberg, C. M. (2003). Second-order Wavemaker Theory for Multidirectional Waves, *Ocean Engineering, Vol. 30*, pp. 1203-1231.
Schäffer, H. A. and Jakobsen, K. P. (2003). Non-linear Wave Generation and Active Absorption in Wave Flumes, *Long waves symposium , Thessaloniki, Greece, 2003. (in parallel with XXX IAHR Congress).*
Tavakkol, S. and Lynett, P. (2017). Celeris: A GPU-accelerated open source software with a Boussinesq-type wave solver for real-time interactive simulation and visualization. *Computer Physics Communications, Vol. 217*, pp. 117.127.
Vincent, C. L. and Briggs, M. J. (1989). Refraction – Diffraction of Irregular Waves over a Mound. *Journal of Waterway, Port, Coastal and Ocean Engineering, Vol. 115, No. 2,* pp. 269-284.
Yang, Z., Liu, S., Bingham, H. B. and Li, J. (2014). Second-order coupling of numerical and physical wave tanks for 2D irregular waves. Part II: Experimental validation in two-dimensions. *Coastal Enginering, Vol 92,* pp. 61–74.
Yang, Z., Liu, S., Ji, X., Bingham, H. B. and Zhang, H. (2021). A generalized second-order 3D theory for coupling multidirectional wave propagation from a numerical model to a physical model. Part I: Derivation, implementation and model verification irregular waves. *Coastal Engineering, Vol 165*.
Zelt, J.A. and Skjelbreia, J. E. (1992). Estimating Incident and Reflected Wave Fields Using an Arbitrary Number of Wave Gauges. *Proceedings of the twenty-third int. conference on coastal engineering, New York*, pp. 777–789.
Zhang, H., Schäffer, H.A. and Jakobsen, K.P. (2007). Deterministic combination of numerical and physical coastal wave models. *Coastal Engineering, Vol 54,* pp. 171–186.

DOI: https://doi.org/10.53256/COSE_250102

# Directional Decomposition of Experimental Data with Nonlinear Short-Crested Waves Using the NL-SORS Method

S. K. Iversen[a,*], T. Lykke Andersen[a], F. Alfaro Corrales[b] and M. R. Eldrup[a]
[a]*Department of the Built Environment, Aalborg University, Aalborg, Denmark*
[b]*Department of Civil Engineering, Ghent University, Ghent, Belgium*

[*]*Corresponding author: Sarah Krogh Iversen (ski@build.aau.dk)*

ABSTRACT: In physical model testing of coastal structures, the wave conditions acting on the structure are typically assessed from surface elevation measurements, which provide the total sea-surface elevation of the generated sea state. However, to relate structural loading and response to the incident wave field, it is necessary to estimate the incident wave components separately. The NL-SORS method for separation of incident and reflected nonlinear short-crested waves, based on measurements from a wave gauge array, has recently been introduced and validated using synthetic data. In the present study, the method is applied to experimental data covering a range of directional spreading conditions and levels of nonlinearity. For all tested cases, the method demonstrates stability and successfully reconstructs both the decomposed surface elevation time series and the corresponding three-dimensional directional wave spectrum.

KEYWORDS: Wave Analysis, Multidirectional Waves, Incident Waves, Wave Separation, Physical Modelling

## 1 INTRODUCTION

In physical model testing of coastal structures, it is essential to determine the incident waves acting on the structure. In the absence of a structure, incident waves may be measured using a single wave gauge, provided that passive absorption is sufficiently effective. However, for short-crested waves, a single gauge does not provide information on the directional spectrum. When a structure is present, multiple gauges or co-located wave gauges are required to estimate the incident waves by applying wave separation techniques.

Traditional separation methods for long-crested (2D) waves, based on surface elevation measurements at multiple locations, were introduced by Goda and Suzuki (1976) for two wave gauges and by Mansard and Funke (1980) for three wave gauges. These methods were later extended by Zelt and Skjelbreia (1993) to accommodate an arbitrary number of wave gauges. In these approaches, the incident and reflected components are separated based on phase differences between measurement locations.

For nonlinear long-crested waves, the system of equations was extended to include bound nonlinear components by Lin and Huang (2004) for regular waves, while Lykke Andersen et al. (2017) incorporated amplitude dispersion effects. Eldrup and Lykke Andersen (2019) further extended these principles to irregular waves, and de Ridder et al. (2023) improved their practical implementation. Suh et al. (2001) and Draycott et al. (2019) additionally incorporated current effects into the separation framework.

For short-crested waves, incident wave characteristics can only be estimated using multiple gauges combined with appropriate wave separation methods. Many existing approaches for three-dimensional wave analysis are limited to frequency-domain techniques that provide only the directional wave spectrum and do not enable time-domain separation of the wave field. Examples include the Bayesian Directional Method (BDM) by Hashimoto and Kobune (1988), the Maximum Likelihood Method (MLM) by Capon et al. (1976), Isobe et al. (1984), and Krogstad (1988), as well as the Maximum Entropy Method (MEM) by Hashimoto et al. (1994).

Draycott et al. (2016) proposed exploiting knowledge of the single-summation wave generation method in the directional analysis of linear short-crested waves. Iversen et al. (2024) introduced the SORS method to account for oblique reflections, and Iversen et al. (2025) subsequently extended this framework to nonlinear waves. The NL-SORS method was demonstrated by Iversen et al. (2025) using a limited number of numerical simulations; however, it has not yet been validated using physical model test data. Experimental data may contain additional sources of error that could affect the method's performance.

For the corresponding linear formulation, Iversen et al. (2024) demonstrated low sensitivity to error sources such as additional basin wall reflections, measurement noise, wave gauge misplacement, and calibration errors. However, the inclusion of nonlinear effects—such as bound wave components and simplified amplitude dispersion—leads to a more complex system of equations. Consequently, the nonlinear separation procedure is expected to be more sensitive to noise, measurement inaccuracies, and deviations from the assumed mathematical model than conventional linear methods.

In the present paper, the NL-SORS method proposed by Iversen et al. (2025) is applied to physical model test data. The method is first briefly introduced, followed by a description of the sea states considered in the present analysis. The wave generation procedure is described in detail by Lykke Andersen et al. (2025). The decomposed wave fields are then presented and discussed in relation to the applied wave generation. Finally, the main conclusions are provided.

## 2 METHODOLOGY

### 2.1 *Wave Decomposition Using the NL-SORS Method*

The wave decomposition method proposed by Iversen et al. (2025) applies to wave fields generated using the single-summation method and is therefore applicable to both numerical and physical model data produced according to this principle. The method requires a stationary, non-breaking wave field that can be represented as a finite sum of wave components. The incident and reflected wave fields are decomposed using a least-squares approach, minimizing the error between the measured and estimated signals in the frequency domain.

For each Fourier component of the measured surface elevation signals, a mathematical model describes how the observed complex wave amplitudes, $\boldsymbol{\zeta}$, are related to the phase-difference matrix, $\boldsymbol{C}$, and the complex amplitudes of the separated wave components, $\boldsymbol{X}$, through the linear system of equations given in Eq. (1).

$$\boldsymbol{CX} = \boldsymbol{\zeta} \tag{1}$$

The phase-difference matrix $\boldsymbol{C}$ contains information on the wave celerity, the direction of propagation of the wave components at the given frequency, and the spatial positions of the measurement points. In traditional linear two-dimensional (2D) wave separation methods, the phase-difference matrix is constructed using linear dispersion theory and by assuming that reflected waves propagate in the opposite direction to incident waves, as wave propagation is restricted to the $x$-direction.

For linear three-dimensional (3D) separation techniques based on the single-summation assumption, the system of equations is fundamentally similar. However, instead of restricting the reflected waves to propagate in the opposite direction of the incident waves, the direction of propagation of each separated wave component is estimated by fitting the model to the observed Fourier components using a least-squares procedure, as in the traditional 2D methods. Under the single-summation assumption, each frequency component is assumed to have only one incident direction. Estimation of the propagation directions requires a non-collinear wave gauge array with an appropriate geometric configuration, as discussed by Iversen et al. (2025).

For nonlinear separation techniques in both 2D and 3D, the system of equations is extended to include bound nonlinear components, and simplified amplitude dispersion is introduced for the identified subharmonic, primary, and superharmonic frequency regions. As the number of unknown components increases, the number of wave gauges required for a robust decomposition must also increase accordingly.

When applying the NL-SORS method (Iversen et al., 2025), it is assumed that, for each frequency component in the nonlinear regions, the analysed 3D wave field can be represented by a maximum of four components: an incident free, incident bound, reflected free, and reflected bound component. The validity of this assumption was examined in detail by Iversen et al. (2025). Each component may have its own propagation direction, $\theta$, which effectively determines whether it is classified as incident or reflected. The celerity of the bound components is defined based on a narrowband assumption of both the frequency spectrum and the directional spreading function. The system of equations for a total of

$$\begin{bmatrix} e^{\mathrm{i}\omega \boldsymbol{k}_{I,F}^{(n)}(\theta_{I,F}^{(n)})\boldsymbol{x}_1} & e^{\mathrm{i}\omega \boldsymbol{k}_{I,B}^{(n)}(\theta_{I,B}^{(n)})\boldsymbol{x}_1} & e^{\mathrm{i}\omega \boldsymbol{k}_{R,F}^{(n)}(\theta_{R,F}^{(n)})\boldsymbol{x}_1} & e^{\mathrm{i}\omega \boldsymbol{k}_{R,B}^{(n)}(\theta_{R,B}^{(n)})\boldsymbol{x}_1} \\ e^{\mathrm{i}\omega \boldsymbol{k}_{I,F}^{(n)}(\theta_{I,F}^{(n)})\boldsymbol{x}_2} & \vdots & \vdots & \vdots \\ \vdots & \vdots & \vdots & \vdots \\ e^{\mathrm{i}\omega \boldsymbol{k}_{I,F}^{(n)}(\theta_{I,F}^{(n)})\boldsymbol{x}_M} & e^{\mathrm{i}\omega \boldsymbol{k}_{I,B}^{(n)}(\theta_{I,B}^{(n)})\boldsymbol{x}_M} & e^{\mathrm{i}\omega \boldsymbol{k}_{R,F}^{(n)}(\theta_{R,F}^{(n)})\boldsymbol{x}_M} & e^{\mathrm{i}\omega \boldsymbol{k}_{R,B}^{(n)}(\theta_{R,B}^{(n)})\boldsymbol{x}_M} \end{bmatrix} \begin{bmatrix} X_{I,F} \\ X_{I,B} \\ X_{R,F} \\ X_{R,B} \end{bmatrix} = \begin{bmatrix} \hat{\eta}(\boldsymbol{x}_1) \\ \hat{\eta}(\boldsymbol{x}_2) \\ \vdots \\ \hat{\eta}(\boldsymbol{x}_M) \end{bmatrix} \quad (2)$$

$M$ gauge positions is expressed in matrix form as given in Eq. (2).

The superscript $(n)$ denotes the frequency region (subharmonic, primary, or superharmonic) to which the component belongs. The subscripts $I$ and $R$ refer to incident and reflected components, respectively, while $F$ and $B$ denote free and bound components.

In the primary region, the system reduces to two components, as only primary (free) waves are assumed to be present. In the subharmonic and superharmonic regions, the number of components is reduced only if the condition number of the system exceeds a prescribed threshold, as suggested by de Ridder et al. (2023).

The output of the NL-SORS analysis consists of the decomposed complex wave amplitudes, $\boldsymbol{X}$, together with the corresponding propagation directions, $\theta$, of each component. Based on their directions, the components are classified as incident or reflected. From the decomposed components, the 3D directional spectrum can be reconstructed following the procedure described by Draycott et al. (2015). Furthermore, the surface elevation of the separated wave fields can be reconstructed at arbitrary spatial locations, enabling direct correlation between structural response and the incident wave field.

## 2.2 Ad Hoc Unified Wave Generation

In the present study, waves in the physical model are generated using the ad hoc unified wave generation method proposed by Zhang et al. (2007). This approach requires depth-averaged particle velocities as input, which, in the present tests, are obtained from the numerical model Celeris (Tavakkol and Lynett, 2017). In the numerical model, short-crested waves are generated in deeper water at a water depth $h_{\mathrm{deep}}$ using the single-summation method. The waves are subsequently propagated over a gently sloping seabed with a slope of 1:80. The depth $h_{\mathrm{deep}}$ is selected such that second-order wave theory remains valid for wave generation within the numerical domain. The physical model represents a subsection of the full numerical domain, as illustrated in Figure 1.

In the region corresponding to the physical model domain, the seabed is horizontal, and the water depth is denoted by $h$.

The coupled numerical–physical modelling approach enables the generation of highly nonlinear waves in the physical model without the need for transition slopes or the application of wavemaker theories outside their validity range. Both of these alternatives may introduce spurious free-wave components, as demonstrated by Eldrup and Lykke Andersen (2024). Further details regarding the numerical model setup and discretisation are provided by Lykke Andersen et al. (2025).

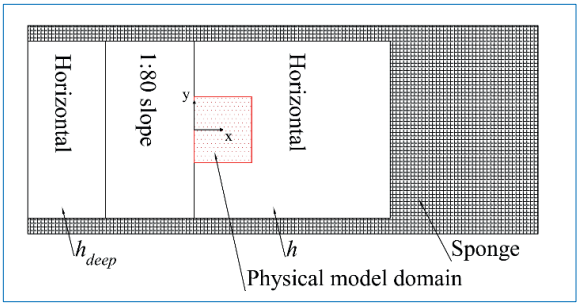


Figure 1. Plan v view of the numerical model setup (not to scale). The mean wave propagation direction is from left to right. Waves in the numerical model are generated along the left boundary.

## 2.3 Physical Model Setup

The physical model tests were conducted at the Ocean and Coastal Engineering Laboratory at Aalborg University, Denmark. The wave basin has an active area of 13 × 8.4 m and is equipped with 30 vertically hinged, individually controlled piston-type wavemakers, enabling accurate generation of three-dimensional (3D) wave fields. Efficient passive absorption is installed along the rear wall and parts of the sidewalls. The experiments were performed over a horizontal seabed and without any structure present. Consequently, wave reflections are expected to be limited and predominantly linear. The wave field was analysed based on surface elevation measurements obtained from an array of wave gauges, as shown in Figure 2.

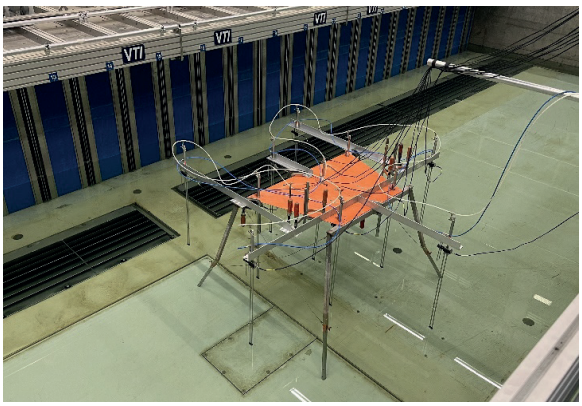

Figure 2. Physical model setup in the wave basin at the Ocean and Coastal Engineering Laboratory, Aalborg University.

The same wave gauge array was used for all tested sea states in the present analysis. The layout of the array and its position within the basin are shown in Figure 3.

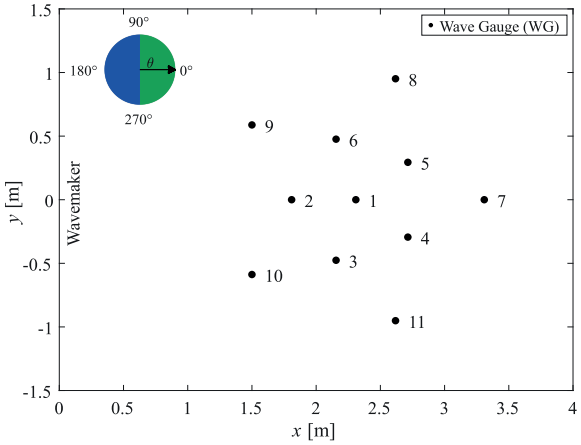


Figure 3. Wave gauge array configuration. Wave gauge 1 is located at the centre of the array. Wave gauges 2–6 are evenly distributed along an inner circle with diameter $D_1 = 1$m. Wave gauges 7–11 are evenly distributed along an outer circle with diameter $D_2 = 2$m. Incident (green) and reflected (blue) wave propagation directions (θ) are indicated.

The basin coordinate system is defined such that the basin centreline coincides with the x-axis (see Figure 1). The wave propagation direction, θ, is defined such that θ = 0° corresponds to the positive x-direction, with positive angles measured counterclockwise.

The waves were generated without corner reflection control. As a result, diffraction and reflection zones are expected near the sidewalls of the basin (cf. Dalrymple, 1989). The wave gauge array was therefore positioned such that the innermost gauges were located just outside the nearfield region, which was conservatively defined as three water depths from the mean wavemaker position.

### 2.4 *Input Sea States*

To evaluate the performance of the decomposition method using physical model data, several multidirectional, nonlinear sea states were tested. The waves were generated using a $\cos^{2s}$ directional spreading function. The test programme included two sea states (Tests 00–01) characterised by broad directional spreading, defined by a small spreading parameter $s = 15$, and four sea states (Tests 02–05) with narrower directional spreading ($s = 50$) and progressively decreasing wave steepness. All sea states were generated in the numerical model at a water depth $h_{\text{deep}}$. The frequency spectrum in all cases followed a JONSWAP distribution with a peak enhancement factor $\gamma = 3.3$. In the physical model, the water depth was constant at $h = 0.5$m, with a horizontal seabed. The wave gauge array configuration was identical to that used by Iversen et al. (2025). Because the same array layout was applied to all tests, the ratios between the array diameters and the wavelength at the spectral peak frequency, $L_p$, are also reported. Iversen et al. (2025) recommended diameter-to-wavelength ratios of 0.15 and 0.30 for optimal performance. The input parameters for the sea states generated in the numerical model are summarised in Table 1.

Table 1: Numerical model input parameters: spectral significant wave height at the physical model wavemaker ($H_{m0}$); peak period ($T_p$); mean wave direction ($\theta_0$); directional spreading parameter ($s$); peak enhancement factor ($\gamma$); water depth in the deep region of the numerical model ($h_{\text{deep}}$); water depth in the physical model domain ($h$); and ratios between the inner ($D_1/L_p$) and outer ($D_2/L_p$) diameters of the wave gauge array and the wavelength at the spectral peak frequency ($L_p$).

| ID | $H_{m0}$ [m] | $T_p$ [s] | $\theta_0$ [°] | $s$ [-] | $\gamma$ [-] | $h_{deep}$ [m] | $h$ [m] | $D_1/L_p$ [-] | $D_2/L_p$ [-] |
|---|---|---|---|---|---|---|---|---|---|
| Test00 | 0.15 | 2.5 | 0 | 15 | 3.3 | 0.635 | 0.5 | 0.19 | 0.38 |
| Test01 | 0.15 | 3.0 | 0 | 15 | 3.3 | 0.756 | 0.5 | 0.16 | 0.31 |
| Test02 | 0.15 | 2.5 | 0 | 50 | 3.3 | 0.746 | 0.5 | 0.19 | 0.39 |
| Test03 | 0.15 | 3.0 | 0 | 50 | 3.3 | 0.746 | 0.5 | 0.16 | 0.31 |
| Test04 | 0.15 | 3.5 | 0 | 50 | 3.3 | 0.859 | 0.5 | 0.13 | 0.26 |
| Test05 | 0.15 | 4.0 | 0 | 50 | 3.3 | 0.972 | 0.5 | 0.12 | 0.23 |

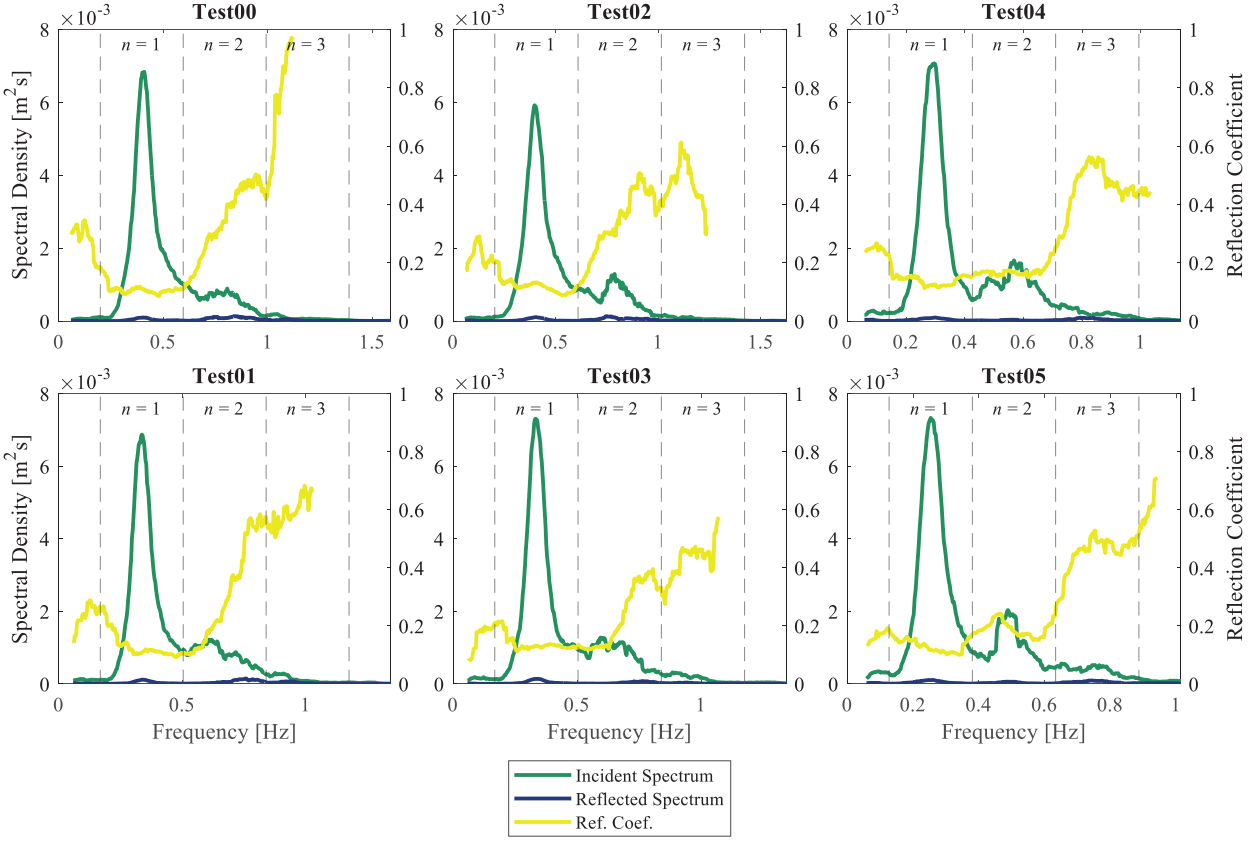


Figure 4. Estimated incident and reflected wave spectra obtained using the NL-SORS method. The left vertical axis represents the spectral density of the decomposed spectra, while the right vertical axis shows the estimated reflection coefficient, calculated as the ratio of reflected amplitude to incident amplitude.

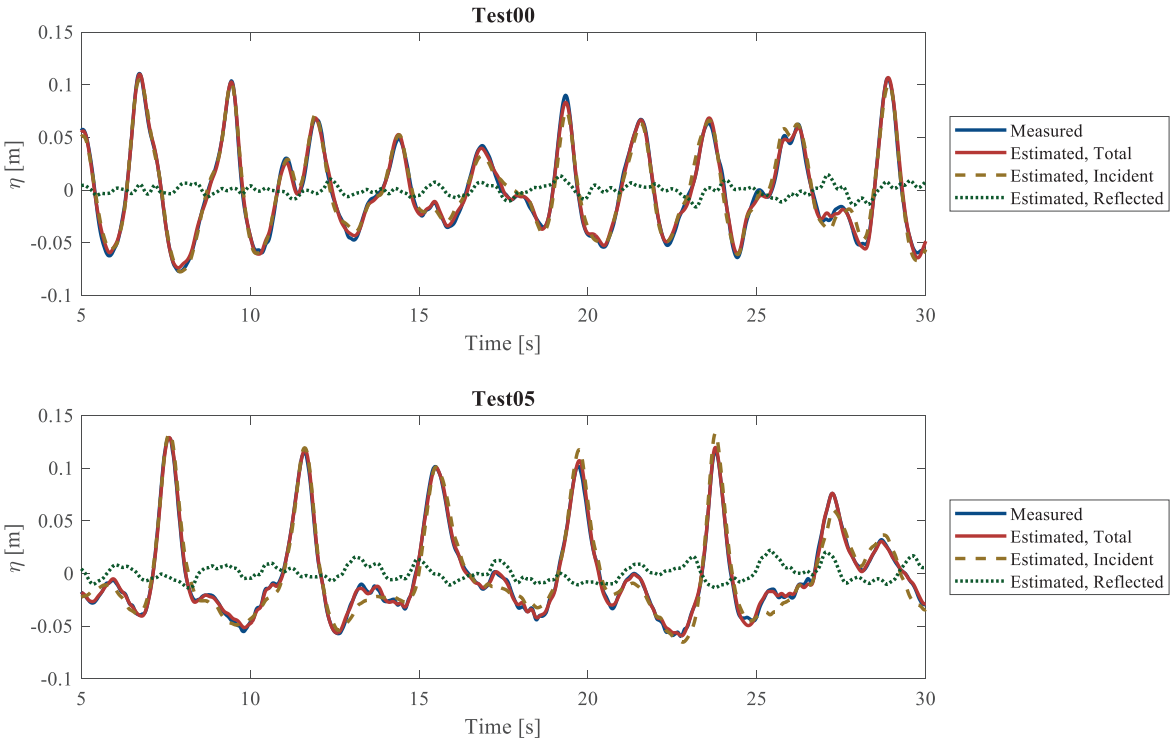


Figure 5. Comparison between estimated and measured surface elevation time series at the location of wave gauge 1 for the most directionally spread sea state, Test00 (top), and the most nonlinear sea state, Test05 (bottom). For both cases, the selected time window contains the largest wave recorded during the test duration.

## 3 RESULTS

The results obtained using the NL-SORS method are presented below. During the physical model tests, no wave breaking was observed. The surface elevation signals revealed a difference in energy levels at WG7 (cf. Figure 3), which may be attributed to diffraction effects within the basin, as WG7 is located furthest from the wavemakers. Since diffraction effects are not accounted for in the applied method, WG7 was excluded from the analysis.

The resulting decomposed wave spectra are shown in Figure 4. The method estimates a low level of reflections in the physical wave basin. In the primary frequency region, the reflection coefficient is approximately 0.12, which is consistent with the expected performance of the passive absorption system. Reflections increase at higher frequencies, which is also anticipated given the characteristics of the passive absorption system composed of vertical layers of expanded metal sheets.

The reconstruction of the surface elevation time series is illustrated in Figure 5 for Test00 and Test05 at the position of wave gauge 1, located at the centre of the array. Test00 represents the most directionally spread and least nonlinear sea state analysed, whereas Test05 is the least directionally spread but most nonlinear case. For Test05, nonlinear features characterised by high, narrow crests and broader, shallower troughs are successfully reproduced by the NL-SORS method. The results demonstrate that, even under conditions of high directional spreading and strong nonlinearity, the reconstructed total surface elevation at the array centre closely matches the measured signal.

A comparison between the reconstructed and measured total surface elevations for all tests is shown in Figure 6. Results obtained using the linear SORS method (Iversen et al., 2024) and the linear SPAIR method (Draycott et al., 2016) are included to highlight the importance of incorporating nonlinear contributions. The reconstruction error is quantified using the relative variance error, averaged over all gauge positions, as summarised in Table 2.

Table 2: Relative variance error of the reconstructed total surface elevation compared with measured signals (mean value over all gauge positions).

| ID | | SPAIR | SORS | NL-SORS |
|---|---|---|---|---|
| Test00 | C1 | 4.17% | 4.77 % | 1.33% |
| Test01 | D1 | 3.11% | 3.15 % | 0.83% |
| Test02 | C2 | 3.41% | 2.78 % | 0.90% |
| Test03 | D2 | 2.38% | 1.99 % | 0.64% |
| Test04 | E2 | 2.00% | 1.57 % | 0.43% |
| Test05 | F2 | 1.84% | 1.33 % | 0.33% |

Based on the variance errors, the reconstruction accuracy improves as directional spreading decreases, as observed when comparing Test00 with Test02 and Test01 with Test03. Furthermore, accuracy improves progressively from Test02 to Test05. This trend may partly result from reduced directional spreading and increased nonlinear transformation during propagation over the numerical model slope. As the slope length increases across these cases, nonlinear waves undergo stronger refraction, which may enhance the consistency of the directional structure within the array.

Additionally, the estimated wave directions influence the spatial variability of surface elevation within the fixed-size array. For longer waves, the relative variation across the array is smaller than for shorter waves. Therefore, the ratio between array dimensions and the peak wavelength should be considered when evaluating method performance. From Test02 to Test05, the peak wavelength increases, reducing the relative distance between the array centre and its outer diameter. Iversen et al. (2025) demonstrated that reconstruction accuracy decreases with increasing distance from the array centre.

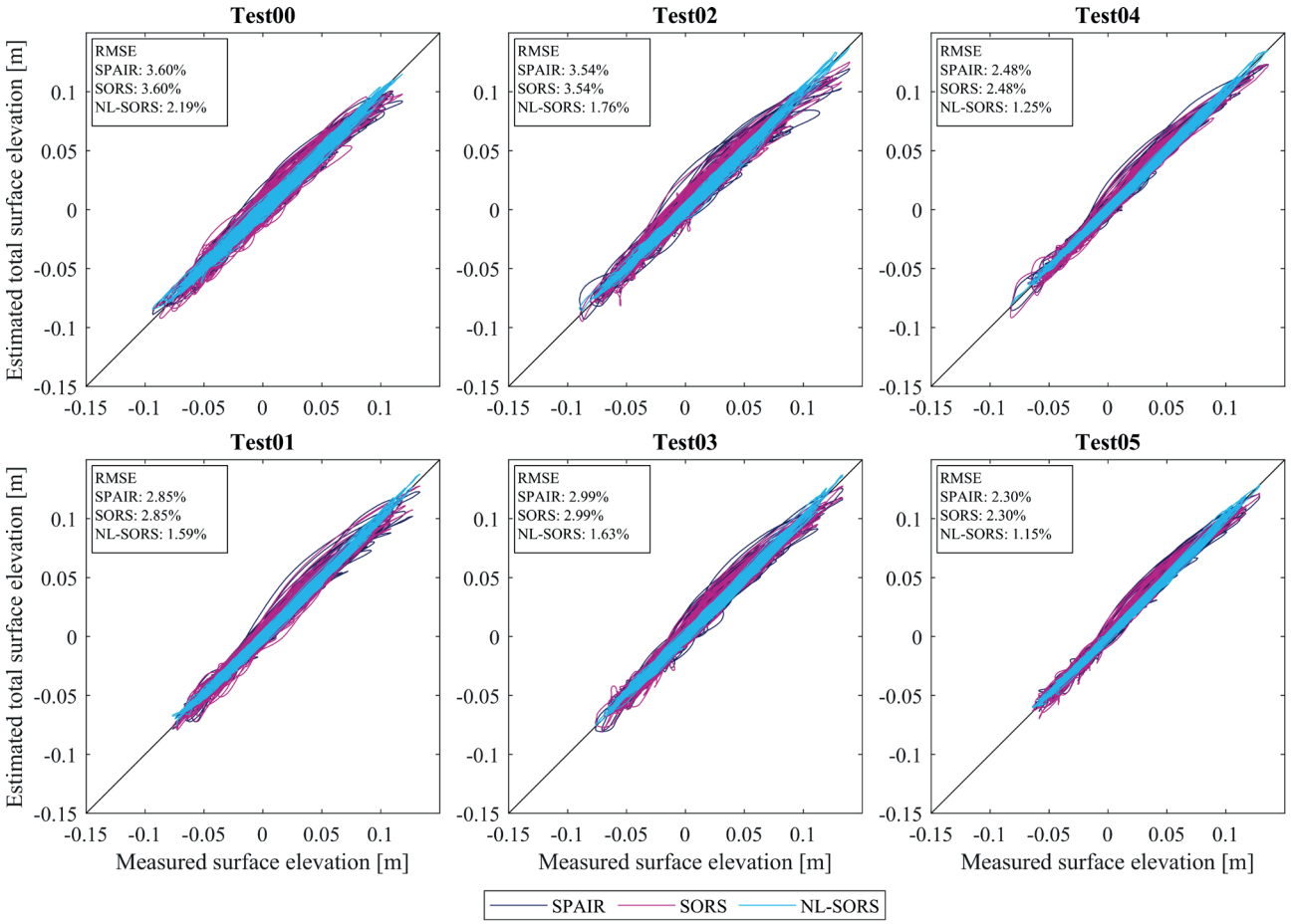


Figure 6. Comparison of the reconstructed total surface elevation and the measured surface elevation at wave gauge position 1 (see Figure 3). A perfect agreement corresponds to the diagonal line. The root-mean-square error (RMSE) is reported relative to the significant wave height.

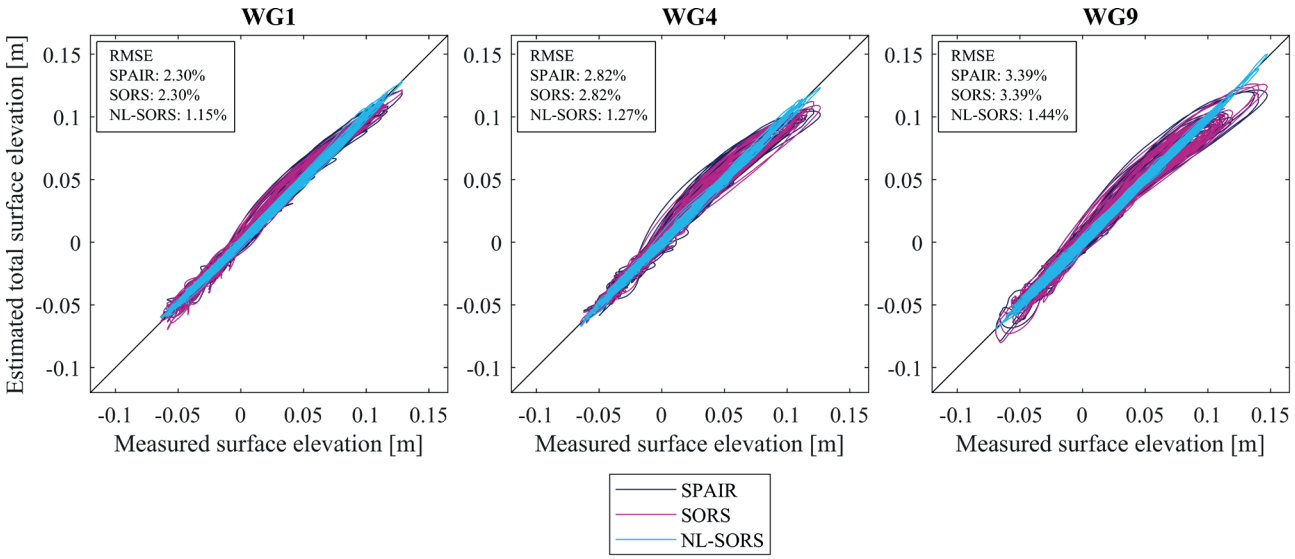


Figure 7. Comparison of the reconstructed and measured total surface elevation for Test05 at three wave gauge locations with increasing distance from the array centre: WG1 (0 m), WG4 (1 m), and WG9 (2 m). A perfect agreement corresponds to the diagonal line.

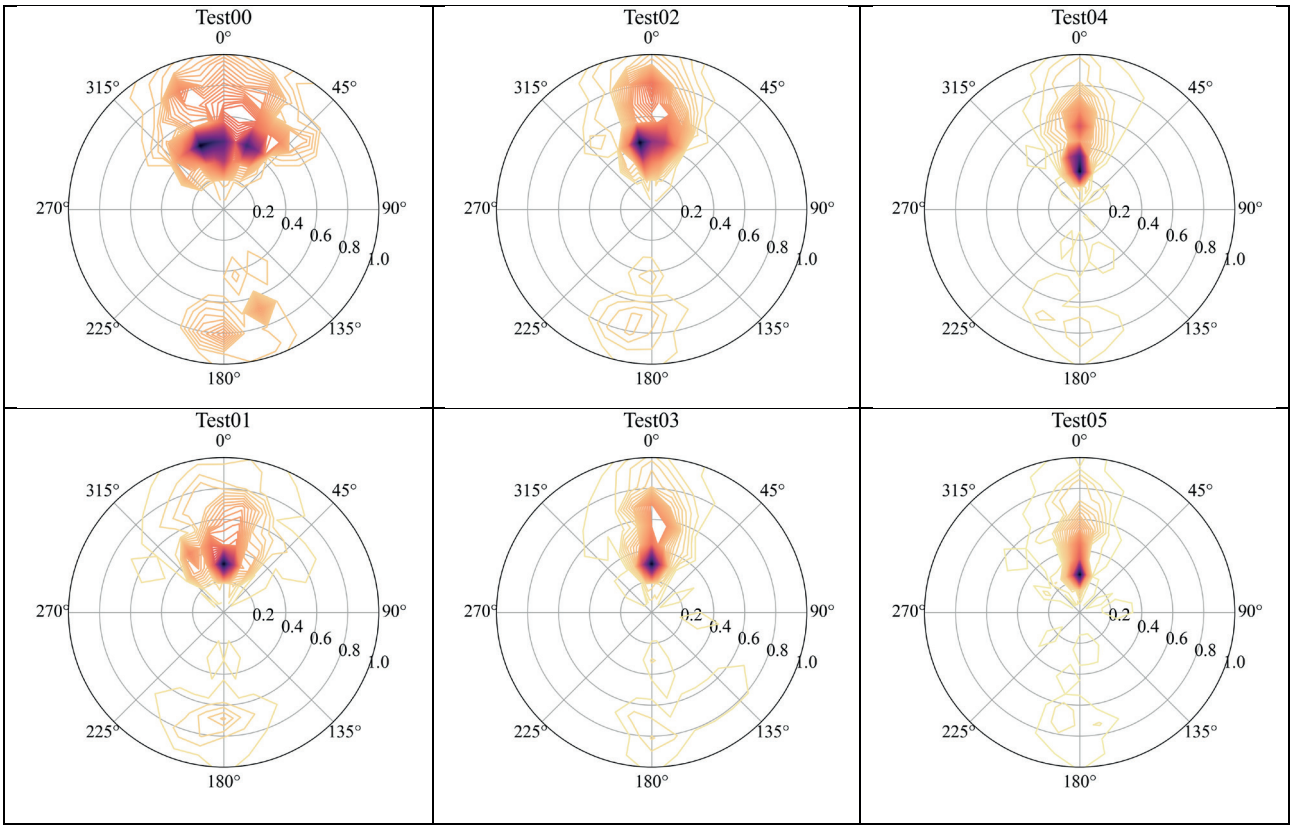


Figure 8. Reconstructed three-dimensional directional spectra obtained using the NL-SORS method. Spectral density is represented by the colour scale of the contour plot, ranging from light yellow/orange (lowest spectral density) to dark purple/blue (highest spectral density). The radial coordinate represents frequency (Hz).

This effect becomes more pronounced for highly nonlinear cases, as uncertainties in the mathematical model primarily relate to the celerity and direction of higher-order bound components. These bound components have lower amplitudes in less nonlinear cases, consistent with the estimated spectra shown in Figure 4. To ensure accurate reconstruction over a larger spatial area, inclusion of nonlinear effects is essential. This conclusion is supported by the present analyses, as illustrated in Figure 7, which compares reconstructed total surface elevations for Test05 at the centre, inner diameter, and outer diameter of the wave gauge array.

In addition to decomposed spectra and reconstructed surface elevation time series, the NL-SORS method enables reconstruction of the estimated three-dimensional directional spectrum (Figure 8). The decomposed wave components are grouped into 36 directional bins and 512 frequency bins, corresponding to averaging over 32 wave components in the frequency domain. The resulting directional spectra confirm that incident and reflected wave directions are identified correctly, and they show that directional spreading decreases with increasing peak wave period.

## 4 DISCUSSION

To further evaluate the performance of the method, the decomposition into free and bound wave components is examined. For Test03, Figure 9 shows a pronounced peak in the spectral density of the bound incident spectrum in the second-order superharmonic region (n = 2), as well as a smaller peak in the third-order superharmonic region (n = 3). This behaviour is expected given the nonlinearity of the sea state. The free (primary) component of the spectrum closely resembles a JONSWAP distribution.

For the most nonlinear sea state, Test05, the increase in energy within the second-order region is even more pronounced (see Figure 4). However, Figure 10 indicates that a larger proportion of superharmonic free energy is estimated, and the spectral shape deviates from the expected JONSWAP form. Since this deviation is most evident for the sea state with the smallest directional spreading, it is unlikely to be caused by the narrow-banded directional spreading assumption of the present method, which should in fact perform more accurately for longer waves (cf. Iversen et al., 2025). Instead, the elevated level of free energy may be related either to limitations in the separation method or to characteristics of the physical wave generation.

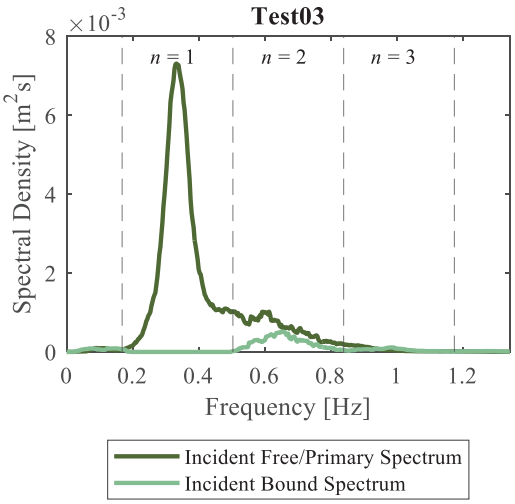


Figure 9. Estimated incident spectrum for Test03 using the NL-SORS method, separated into free (primary) and bound components.

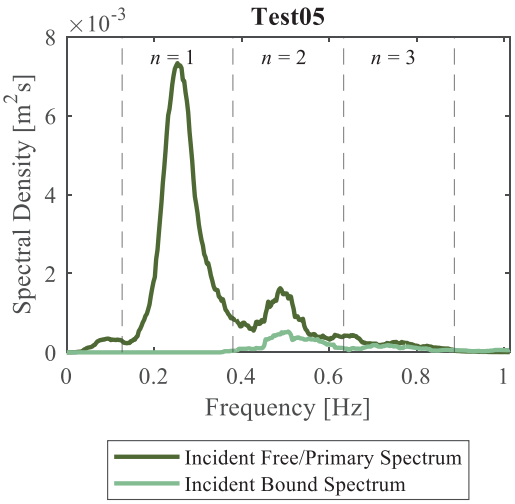


Figure 10. Estimated incident spectrum for Test05 using the NL-SORS method, separated into free (primary) and bound components.

In relation to the separation method, Eldrup and Lykke Andersen (2019) demonstrated that if the celerities of the free and bound components are nearly identical, accurate separation is not possible. This condition may be assessed using Eq. (3) for the *i*th frequency component:

$$\frac{c_B}{c_F} = \frac{k_i}{n \cdot k_i(\omega/n)} > \alpha \qquad (3)$$

Eldrup and Lykke Andersen (2019) suggested a conservative threshold value of α = 1.15, while values in the range 1.05–1.15 may occasionally yield reliable results. The ratios between bound and free celerities in the second-order superharmonic region for the present test cases are summarised in Table 3.

Table 3: Ratio between bound and free wave celerity in the second-order superharmonic region (evaluated at $2f_p$).

| ID | $c_B/c_F$ |
|---|---|
| Test00 | 1.20 |
| Test01 | 1.13 |
| Test02 | 1.21 |
| Test03 | 1.13 |
| Test04 | 1.09 |
| Test05 | 1.07 |

A key distinction between the present NL-SORS method and the two-dimensional application described by Eldrup and Lykke Andersen (2019) is that, in NL-SORS, bound and free components may propagate in different directions, even when both are incident. However, since Test05 was generated with limited directional spreading and experienced significant refraction, the free and bound components may not differ sufficiently in direction or celerity to allow robust separation. In such cases, the allocation between free and bound components may become ambiguous. As shown in Table 3, the celerity ratios approach unity with increasing nonlinearity, which may explain the elevated level of free energy observed for Test05 in Figure 10.

The increased free energy may also be attributed to the physical wave generation. As shown in Figures 11 and 12, the primary spectral energy from the numerical model is not fully reproduced in the physical model for Test05, whereas the agreement is stronger for Test03. This discrepancy may result from energy losses, for example due to leakage beneath and between wavemaker paddles. Consequently, the primary waves in the physical model for Test05 may bind less energy than predicted numerically. As a result, part of the bound energy in the higher-order regions may be released as free waves. The reduction in primary spectral density is not due to wave breaking, as no breaking was observed during the experiments.

The validity of the numerical model should also be considered. If the numerical simulation overestimates the amount of bound energy relative to what can physically be sustained in the basin, excess energy may similarly be released as free components. Furthermore, incomplete absorption of reflections from the basin walls may result in re-reflection at the paddles, causing additional free components within the directional range defined as incident.

Overall, multiple physical mechanisms may influence the observed wave field. It is therefore not possible to conclusively determine whether the elevated free energy in the second-order region arises from limitations of the separation method or from the characteristics of the physical wave generation. Nevertheless, despite potential ambiguities in the free–bound separation, the reconstructed incident time series and spectra appear robust and physically consistent.

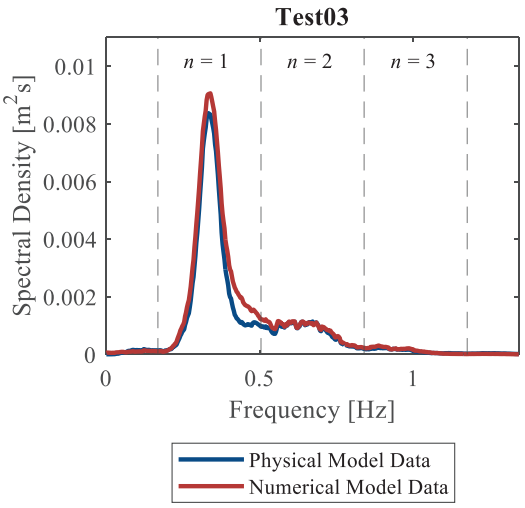


Figure 11. Average measured spectral density for physical and numerical model data, Test03. The average is computed across all gauge positions shown in Figure 3.

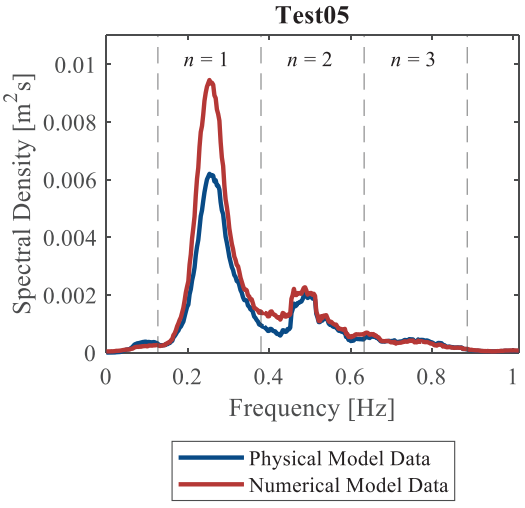


Figure 12. Average measured spectral density for physical and numerical model data, Test05. The average is computed across all gauge positions shown in Figure 3.

## 5 CONCLUSIONS

A method for the directional separation of nonlinear, short-crested waves generated using the single-summation method was presented by Iversen et al. (2025), who demonstrated its performance using synthetic data from a numerical model. In the present study, the method has been evaluated using experimental data obtained from physical model tests conducted in the wave basin of the Ocean and Coastal

Engineering Laboratory at Aalborg University. The waves were generated using ad hoc unified wave generation, whereby the wavemakers were driven by results from numerical simulations of waves propagating over a mild slope. Two sea states with large directional spreading and four sea states with smaller directional spreading and increasing nonlinearity were investigated.

For the longest and most nonlinear test case, results indicate that, in the second-order superharmonic region, free energy may either be physically released or inaccurately estimated by the separation method. Such discrepancies may arise because the celerities of the free and bound components are nearly identical, which limits the ability of the method to distinguish between them. The applied wave generation technique and the performance of the basin's absorption system require further evaluation before definitive conclusions can be drawn regarding the capability of the method to reliably separate free and bound components in highly nonlinear sea states.

Based on the present analysis, it is concluded that the NL-SORS method is stable when applied to experimental data and that the reconstructed surface elevation time series exhibit high accuracy for all tested sea states within the spatial extent of the wave gauge array.

## ACKNOWLEDGEMENTS

This work was supported by the Danish Energy Agency under the Energy Technology Development and Demonstration Program (EUDP), contract number 64022-1062, Niels Bohrs Vej 8D, 6700 Esbjerg, Denmark.

## REFERENCES

Capon, J., Greenfield, R.J., Kolker, R.J. (1976). Multidimensional maximum-likelihood processing of a large aperture seismic array. *Proc. IEEE 55*, 192–211.

Dalrymple, R.A. (1989). Directional wavemaker theory with sidewall reflection. *Journal of Hydraulic Research*, 27, 1, 23-34.

Draycott, S., Davey, T., Ingram, D.M., Lawrence, J., Day, A., Johanning, L. (2015). Using a phase-time-path-difference approach to measure directional wave spectra in Flowave. *EWTEC Conference Proceedings*.

Draycott, S., Davey, T., Ingram, D.M., Day, A., Johanning, L. (2016). The SPAIR method: Isolating incident and reflected directional wave spectra in multidirectional wave basins. *Coastal Engineering 114*, 265–283.

Draycott, S., Pillai, A.C., Ingram, D.M., Johanning, L. (2019). Resolving combined wave-current fields from measurements using interior point optimization. *Coastal Engineering*.

Eldrup, M.R., Lykke Andersen, T. (2019). Estimation of incident and reflected wave trains in highly nonlinear two-dimensional irregular waves. *Journal of Waterway, Port, Coastal and Ocean Engineering 145(1)*.

Eldrup, M. R. and Lykke Andersen, T. (2024). Generation of Highly Nonlinear Waves in a Short Wave Flume. *CoastLab24, Delft, The Netherlands.*

Goda, Suzuki (1976). Estimation of incident and reflected waves in random wave experiments. *Proceedings of the 15th Coastal Engineering Conference*, 828‑845.

Hashimoto, N., Kobune, K. (1988). Directional spectrum estimation from a bayesian approach. *Coastal Engineering Proceedings 1(21),4*, 62‑76.

Hashimoto, N., Nagai, T., Asai, T. (1994). Extension of the maximum entropy principle method for directional wave spectrum estimation. *Proceedings of 24th International Conference on Coastal Engineering, Kobe, Japan*, 232–246.

Isobe, M., Kondo, K., Horikawa, K. (1984). Extension of mlm for estimating directional wave spectrum. Proc. Sympo. *On Description and Modelling of Directional Seas A-6.*

Iversen, S.K., Andersen, T.L., Frigaard, P. (2024). Directional spectrum estimation for sea states generated by the single summation method. *Journal of Coastal and Hydraulic Structures 4, 36*.

Iversen, S. K., Eldrup, M. R., Lykke Andersen, T., Frigaard, P. (2025). The NL-SORS Method for Separation of Nonlinear Multidirectional Waves into Incident and Reflected Wave Trains. *Coastal Engineering*.

Krogstad, H.E. (1988). Maximum likelihood estimation of ocean wave spectra from general arrays of wave gauges. *Modelling, Identification and Control 9*, 373–381.

Lin, C.Y., Huang, C.J. (2004). Decomposition of incident and reflected higher harmonic waves using four wave gauges. *Coastal Engineering 51*, 395‑406.

Lykke Andersen, T., Eldrup, M.R., Frigaard, P. (2017). Estimation of incident and reflected components in highly nonlinear regular waves. *Coastal Engineering 119*, 51‑64.

Lykke Andersen, T., Eldrup, M. R., Iversen, S. K. (2025). Recent Advances in Hydraulic Model Testing Techniques. *SCACR 2025.*

Mansard, E.P.D., Funke, E.R. (1980). The measurement of incident and reflected spectra using a least squares method. *Proceedings of the 17th Coastal Engineering Conference*: 154-172.

de Ridder, M.P., Kramer, J., den Bieman, J.P., Wenneker, I. (2023). Validation and practical application of nonlinear wave decomposition methods for irregular waves. *Coastal Engineering 183*.

Suh, K.D., Park, W.S., Park, B.S. (2001). Separation of incident and reflected waves in wave-current flumes. *Coastal Engineering 43*, 149‑159.

Tavakkol, S. and Lynett, P. (2017). Celeris: A GPU-accelerated open source software with a Boussinesq-type wave solver for real-time interactive simulation and visualization. *Computer Physics Communications*, 217, 117-127.

Zelt, J.A., Skjelbreia, J.E. (1993). Estimating incident and reflected wave fields using an arbitrary number of wave gauges. *Coastal Engineering*: 777-789.
Zhang, H., Schäffer, H.A. and Jakobsen, K.P. (2007). Deterministic combination of numerical and physical coastal wave models. *Coastal Engineering*, 54, 171–186.

DOI: https://doi.org/10.53256/COSE_250103

# MODELING OF LOCAL SCOUR AROUND CIRCULAR STRUCTURES USING THE OPEN-SOURCE CFD TOOLBOX REEF3D

Tina Ebrahimi[a,*], Widar. W. Wang[a], Hans Bihs[a]
[a]*Norwegian University of Science and Technology, Høgskoleringen 7A, 7491 Trondheim, Norway*

[*]*Corresponding author: tina.ebrahimi@ntnu.no (Tina Ebrahimi)*

ABSTRACT: The presence of a structure in the marine environment can significantly alter the surrounding flow field. When the flow encounters a structure, such as a bridge pier, a complex three-dimensional velocity field develops. In front of the pier, a downward-directed flow forms due to stagnation pressure, generating a horseshoe vortex as the vertical flow interacts with the seabed. In addition, a vortex street develops in the wake region behind the pier. This complex flow field governs both the depth and spatial pattern of the resulting scour hole. A comprehensive three-dimensional numerical model implemented in the open-source CFD toolbox REEF3D is employed to simulate local scour around marine structures under steady current conditions. The approach is based on the solution of the Reynolds-averaged Navier–Stokes (RANS) equations, closed with the k–ω turbulence model, and coupled with a sediment transport model. In this study, dynamic free-surface evolution is captured using an interface-capturing level-set method. Furthermore, to enhance numerical stability and accurately represent the structure geometry, a direct-forcing immersed boundary method is applied. The objective of the study is to evaluate how accurately the numerical simulations reproduce both the temporal evolution and the final geometry of the scour hole observed in laboratory experiments. The time-dependent development of the scour pattern under an oscillatory free surface is simulated. A comparison between numerical results and experimental measurements is performed to assess model accuracy. The results indicate that the simulated maximum scour depth agrees with the experimental value within a few percent, and the overall scour morphology is reproduced with good fidelity. These findings demonstrate that the proposed modelling framework provides a robust basis for investigating complex scour processes and can be extended to more challenging hydraulic conditions.

KEYWORDS: Local scour, Free surface, Level set method, Direct forcing method, CFD, REEF3D.

# 1 INTRODUCTION

Marine structures can significantly alter local flow patterns, generating complex three-dimensional flow fields that increase turbulence intensity and bed shear stress (Graf and Istiarto, 2002). These flow modifications typically induce local scour around the structure, potentially compromising structural stability. The scour pattern develops progressively over time, expanding both in depth and lateral extent. A thorough understanding of scour formation under various hydrodynamic conditions is therefore essential to mitigate these hazards (Fredsøe and Sumer, 2002).

One of the most common examples of local scour occurs around bridge piers. As the flow approaches the pier, a complex three-dimensional velocity field develops. A downward-directed flow forms at the upstream face of the pier due to stagnation pressure, generating a horseshoe vortex, while a vortex street forms downstream in the wake region (Bihs, 2011). These flow structures strongly influence both the geometry and maximum depth of the resulting scour hole.

Olsen and Melaaen (1993) developed the first three-dimensional numerical model of local scour, simulating the initial stages under steady flow conditions using a finite-volume formulation and the k–ε turbulence model. Olsen and Kjellesvig (1998) extended this work to model the complete temporal development of scour under transient flow conditions, validating their results against empirical formulations. Roulund et al. (2005) conducted combined numerical and experimental investigations of flow and scour around bridge piers under steady currents using the k–ω turbulence model.

Baykal et al. (2015, 2017) investigated flow and local scour around vertical cylinders under combined wave–current conditions; however, free-surface effects were not explicitly resolved. To incorporate free-surface dynamics, Liu and García (2008) applied the Volume-of-Fluid (VOF) method to simulate scour around a vertical pile. Bihs and Olsen (2008) performed numerical simulations of pier scour and reported good agreement between numerical predictions and experimental data. Subsequently, Bihs (2011) examined the effect of bed slope on the initiation of sediment motion. In a later study, Bihs and Olsen (2011) demonstrated that accounting for reduced bed shear stress on sloping beds improved numerical predictions of abutment scour under steady current conditions.

Afzal et al. (2015) and Ahmad et al. (2015) employed the numerical code REEF3D to simulate scour around a large-diameter pier. Their results under both wave and steady current conditions showed that scour depth and sediment deposition increase with increasing Keulegan–Carpenter number. Ahmad et al. (2018) further investigated scour around side-by-side piles, incorporating free-surface capturing to analyse wave-induced scour. They examined the influence of key parameters, including the Keulegan–Carpenter number and pile spacing, on scour development. Gautam et al. (2021) presented a fully three-dimensional CFD model in REEF3D to simulate combined wave–current-induced scour using a level-set method for free-surface tracking. Fleit et al. (2023) applied REEF3D::CFD to simulate scour around submerged bridge decks, combining the level-set method with a ghost-cell immersed boundary method.

All previous scour studies conducted with REEF3D relied on the ghost-cell immersed boundary approach. More recently, a direct-forcing immersed boundary method has been implemented in REEF3D (Larkermani et al., 2025; Soydan et al., 2024a, 2025) for flow applications, enhancing numerical stability and interface representation.

The objective of the present study is to employ a three-dimensional numerical model within the open-source CFD toolbox REEF3D (Bihs et al., 2016) to simulate complex free-surface flow patterns and local scour around marine structures under steady current conditions. The novelty of this work lies in the first implementation of the direct-forcing immersed boundary method combined with dynamic free-surface capturing for sediment transport modelling in REEF3D. The evolving free surface is resolved using a level-set approach to accurately capture the fluid–air interface. Furthermore, the density interpolation scheme used within the direct-forcing method reduces non-physical spurious velocities at the fluid–structure interface.

The numerical model is validated through detailed comparison with experimental measurements to assess its predictive capability.

# 2 NUMERICAL MODEL

## 2.1 *REEF3D::CFD*

Computational Fluid Dynamics (CFD) modelling provides a powerful framework for the numerical simulation of scour processes. In this study, the numerical framework REEF3D::CFD developed by Bihs et al. (2016) is employed to model the local scour process. The hydrodynamic model is based on the three-dimensional, incompressible Reynolds-averaged Navier–Stokes (RANS)

equations, which represent the conservation of mass and momentum:

$$\frac{\partial u_i}{\partial x_i} = 0 \quad (1)$$

$$\frac{\partial u_i}{\partial t} + u_j \frac{\partial u_i}{\partial x_j} = -\frac{1}{\rho}\frac{\partial p}{\partial x_i} + \frac{\partial}{\partial x_j}\left[(\nu + \nu_t)\left(\frac{\partial u_i}{\partial x_j} + \frac{\partial u_j}{\partial x_i}\right)\right] + g_i \quad (2)$$

where $u_i$ denotes the velocity components, $\rho$the fluid density, $p$ the pressure, $\nu$ the kinematic viscosity, $\nu_t$ the eddy viscosity, and $g_i$the gravitational acceleration. The inclusion of eddy viscosity in the diffusion term reflects the application of the Boussinesq eddy-viscosity approximation to represent turbulence effects.
The $k$–$\omega$ turbulence model (Wilcox, 1994) is used to compute the eddy viscosity $\nu_t$ by solving two additional transport equations for the turbulent kinetic energy $k$ and the specific dissipation rate $\omega$:

$$\frac{\partial \mathrm{k}}{\partial \mathrm{t}} + \mathrm{u_j}\frac{\partial \mathrm{k}}{\partial \mathrm{x_j}} = \frac{\partial}{\partial \mathrm{x_j}}\left[\left(\nu + \frac{\nu_\mathrm{t}}{\sigma_\mathrm{k}}\right)\frac{\partial \mathrm{k}}{\partial \mathrm{x_j}}\right] + \mathrm{P_k} - \beta_\mathrm{k}\mathrm{k} \quad (3)$$

$$\frac{\partial \omega}{\partial t} + u_j\frac{\partial \omega}{\partial x_i} = \frac{\partial}{\partial x_j}\left[\left(\nu + \frac{\nu_t}{\sigma_\omega}\right)\frac{\partial \omega}{\partial x_j}\right] + \frac{\omega}{k}\alpha P_k - \beta\omega^2 \quad (4)$$

where the turbulent production term $P_k$ is defined as:

$$P_k = \nu_t \frac{\partial u_i}{\partial x_j}\left[\frac{\partial u_i}{\partial x_j} + \frac{\partial u_j}{\partial x_i}\right] \quad (5)$$

and the model constant coefficients are as follows:

$$\alpha = \frac{5}{9},\ \beta = \frac{3}{40},\ \beta_k = \frac{9}{100},\ \sigma_\omega = \sigma_k = 2 \quad (6)$$

A signed distance function, referred to as the level-set function, is used to represent the air–water interface. The solid boundaries and mobile bed are also represented using the level-set method. The continuous signed-distance function $\phi(\mathbf{x}, t)$ defines the minimum distance to the interface Γ. For the free surface, the level-set function is defined as:

$$\phi(\vec{x}, t) = \begin{cases} > 0, & \text{if } \vec{x} \in \text{phase 1} \\ = 0, & \text{if } \vec{x} \in \Gamma \\ < 0, & \text{if } \vec{x} \in \text{phase 2} \end{cases} \quad (7)$$

The evolution of the interface is governed by the convection equation:

$$\frac{\partial \phi}{\partial t} + u_j\frac{\partial \phi}{\partial x_j} = 0 \quad (8)$$

To maintain the signed-distance property, the level-set function is reinitialised after each time step following (Sussman et al., 1994):

$$\frac{\partial \phi}{\partial \mathrm{t}} + \mathrm{sign}(\phi)\left(\left|\frac{\partial \phi}{\partial \mathrm{x_j}}\right| - 1\right) = 0 \quad (9)$$

where $\mathrm{sign}(\phi)$ denotes the smoothed sign function (Peng et al., 1999). For mass conservation, the Eikonal condition $|\ \partial\phi/\partial x_j\ | = 1$must be satisfied. The density and viscosity fields are defined as:

$$\rho = \rho_\omega H(\phi) + \rho_a\left(1 - H(\phi)\right) \quad (10)$$

$$\nu = \nu_\omega \mathrm{H}(\phi) + \nu_\mathrm{a}\left(1 - \mathrm{H}(\phi)\right) \quad (11)$$

where subscripts $w$ and $a$ denote water and air properties, respectively. To smooth sharp interface gradients, a regularised Heaviside function $H(\phi)$ is employed with an interface thickness$\epsilon = 2.1\ \Delta\mathrm{x}$:

$$H(\phi) = \begin{cases} 0, & \text{if } \phi < -\epsilon \\ \frac{1}{2}\left(1 + \frac{\phi}{\epsilon} + \frac{1}{\pi}\sin\left(\frac{\pi\phi}{\epsilon}\right)\right), & \text{if } |\phi| \le \epsilon \\ 1, & \text{if } \phi > \epsilon \end{cases} \quad (12)$$

A staggered rectilinear grid is employed together with high-order spatial and temporal discretisation schemes. In the staggered grid arrangement, density and viscosity are directly evaluated at cell faces, reducing unphysical oscillations associated with interpolation procedures (Bihs et al., 2016; Larkermani et al., 2024).
Convective terms in the RANS equations are discretised using a fifth-order Weighted Essentially Non-Oscillatory (WENO) scheme (Jiang and Shu, 1996). The Hamilton–Jacobi formulation of the WENO scheme is applied to the level-set equation as well as to the transport equations for turbulent kinetic energy and specific dissipation rate (Jiang and Peng, 2000). The WENO approach provides high accuracy while enhancing numerical stability.
Temporal integration is performed using a Total Variation Diminishing (TVD) Runge–Kutta scheme. A third-order TVD Runge–Kutta method is applied to the level-set convection equation, while a second-order TVD Runge–Kutta scheme is used for the momentum equations (Shu and Osher, 1988). Diffusion terms are treated implicitly, removing the diffusion restriction from the CFL stability condition (Bihs et al., 2016).
The pressure field is computed using the projection method (Chorin, 1968). The resulting Poisson equation is solved using the BiCGSTAB iterative solver (Van der Vorst, 1992) from the HYPRE high-performance preconditioner library, employing the semi-coarsening multigrid preconditioner PFMG (Ashby and Falgout, 1996).

### 2.2 *Morphological model*

Sediment transport is initiated when the bed shear stress exceeds the critical bed shear stress ($\tau_c$). The bed shear stress can be related to the turbulent kinetic energy near the bed under the assumption that turbulence production and dissipation are in equilibrium:

$$\tau_b = \sqrt{C_\mu}\rho k \tag{15}$$

where the constant $C_\mu$ has a value of 0.09. An accurate determination of the critical bed shear stress is essential for reliable scour prediction. The critical bed shear stress is calculated as:

$$\tau_c = \theta_c(\rho_s - \rho)gd \tag{16}$$

where $\theta_c$ is the critical shields parameter, $\rho_s$ is the sediment density, $\rho$ is the water density, and $d$ is the particle diameter. The classical Shields diagram (Shields, 1936) is applicable primarily to beds with small gradients under fully submerged conditions. However, steeper bed slopes promote sediment motion due to the downslope component of gravitational force (Zanke et al., 2023). As the bed slope increases, the critical bed shear stress decreases, thereby enhancing erosion. In this study, the modified critical bed shear stress proposed by Fredsøe and Deigaard (1992), which accounts for both longitudinal and transverse bed slopes through a reduction factor, is adopted.
The bedload transport rate is calculated using the formulation of Engelund and Fredsøe (1976) as:

$$q_b = \sqrt{\frac{(\rho_s-\rho)g}{\rho}}\, d \begin{cases} 0, & \text{if } \theta < \theta_c \\ 18.74(\theta - \theta_c)(\theta^{0.5} - 0.7\theta_c^{0.5}), & \text{if } \theta > \theta_c \end{cases} \tag{17}$$

where θ is the shields parameter, defined as:

$$\theta = \frac{\tau_b}{(\rho_s-\rho)gd} \tag{18}$$

The mobile bed is represented by the zero level set of the level-set function, eliminating the need for remeshing. Bed-level variations and morphological evolution are computed using the Exner equation, which ensures sediment mass conservation within each computational cell (Paola and Voller, 2005):

$$\frac{\partial z_b}{\partial t} + \frac{1}{(1-n)}\left[\frac{\partial q_{b,x}}{\partial x} + \frac{\partial q_{b,y}}{\partial y}\right] = 0 \tag{19}$$

where, $z_b$ is the bed level, $q_{b,x}$ is the bed load transport in x-direction, $q_{b,y}$ is the bed load transport in y-direction, and $n$ is the porosity of the bed sediment.

The bed slope may approach the angle of repose, particularly for non-cohesive sediments. When this threshold is exceeded, a sand-slide mechanism occurs, representing slope failure. In such cases, excess sediment collapses downslope, and the bed angle is reduced, typically by approximately 2° (Roulund et al., 2005). The present morphological model incorporates a sand-slide mechanism to prevent numerical instability, limit excessive reductions in bed shear stress, and provide a more realistic representation of sediment redistribution (Burkow and Griebel, 2016). Both slope-induced reduction of critical shear stress and the sand-slide mechanism are essential for accurate prediction of local scour (Bihs and Olsen, 2008). In contrast to the rapid evolution of the hydrodynamic field, morphological changes occur over much longer time scales. To reduce computational cost, a decoupled approach is adopted: the morphological model is updated using a larger time step than the hydrodynamic solver. Numerical stability is ensured by adaptively limiting the time step according to the Courant–Friedrichs–Lewy (CFL) condition (Griebel et al., 1998).

## 3 NUMERICAL SETUP

A pier-scour case based on the experimental study of Link (2006) under clear-water steady current conditions was used to evaluate the capability of the direct-forcing-based sediment transport module implemented in REEF3D::CFD. The experiments were conducted in the hydraulic laboratory of the Technical University of Darmstadt in a flume 37 m long, 2 m wide, and 1 m deep. Several tests were performed with varying flow velocities and water depths. The flume sidewalls were constructed of Plexiglas.
A cylindrical Plexiglas pile with a diameter of 0.2 m was installed 16 m downstream of the flume inlet. Sediment layers 1.5 m in length were placed both upstream and downstream of the pier, while the remaining sections of the flume consisted of a concrete bed. Aluminium plates sealed the interface between the sediment bed and the concrete floor to prevent horizontal seepage through the sediment layer. The scour geometry was measured using a laser distance sensor mounted inside the pier; consequently, bed topography outside the immediate scour hole was not recorded.
Natural sand was used as bed material, with a median grain diameter $d_{50} = 0.97$mm, sediment density $\rho_s = 2650$ kg/m$^3$, and an angle of repose of 29°. The selected experimental case corresponds to a flow velocity of 0.3 m/s, a still-

water depth of 0.3 m, and a total experimental duration of 21 hours.

The numerical domain represents a three-dimensional channel 4.5 m long, 2 m wide, and 0.8 m deep, with a water depth of 0.3 m. A cylindrical pier with a diameter of 0.2 m is positioned 1.5 m downstream of the inlet boundary. The bed consists of a 0.3 m thick sediment layer. The critical Shields parameter for incipient motion is set to $\theta_c = 0.035$.

At the inlet, a logarithmic velocity profile corresponding to a depth-averaged velocity of 0.3 m/s (equivalent to a discharge of 0.18 m³/s) is prescribed. A zero-gradient condition is applied to pressure at the inflow boundary. Wall functions are used for the velocity field, and the k–ω turbulence model employs rough-wall functions for the turbulence quantities $k$and $\omega$. The sidewalls are treated as no-slip boundaries. At the outlet, a zero-gradient condition is imposed for velocity, while pressure is prescribed using a Dirichlet condition consistent with the fixed water level.

Figure 1 illustrates the initial configuration of the numerical flume. The initial condition consists of still water with a depth of 0.3 m and a flat sediment bed with uniform material properties. REEF3D's initialization procedure is applied for velocity, pressure, and turbulence variables. A potential-flow solution is used to initialize the velocity field, while a hydrostatic distribution is applied for pressure. The turbulence quantities $k$ and $\omega$ are initialized according to the applied wall-function formulation.

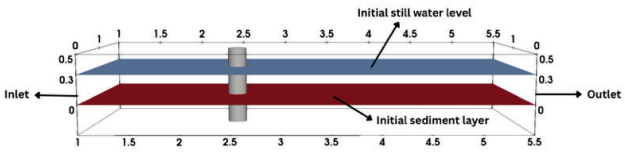


Figure 1. Numerical flume configuration used in the REEF3D simulations.

## 4 NUMERICAL RESULTS

The bed-load transport rate is calculated using the formulation proposed by Engelund and Fredsøe (1976). Bed shear stress is estimated using a turbulent kinetic energy-based formulation, incorporating an appropriate reduction coefficient to improve the prediction of sediment transport. As the primary focus of this study is the dominant mechanism of scour under clear-water steady-current conditions, suspended sediment transport is neglected.

The prescribed depth-averaged flow velocity is 0.3 m/s, corresponding to a discharge of 0.18 m³/s. The hydrodynamic module of REEF3D has been extensively validated in previous studies (e.g., Kamath et al., 2019; Ahmad et al., 2019). Therefore, the present study concentrates primarily on evaluating the performance of the morphological model.

### 4.1 *Convergence study*

A grid convergence study was performed to determine the minimum spatial resolution required for accurate simulation of the scour process. The Courant–Friedrichs–Lewy (CFL) number was fixed at 0.3 to ensure numerical stability of both the hydrodynamic and morphological models. Model performance was evaluated by comparing the time evolution of the maximum scour depth with the experimental data reported by Link (2006).

Four uniform grid resolutions were tested: $\Delta x = \Delta y = \Delta z = 0.05$ m, 0.03 m, 0.01 m, and 0.0075 m, while maintaining a constant CFL number of 0.3. Figure 2 presents the numerical results for the temporal development of the maximum scour depth around the circular pier under steady-current conditions for the four grid sizes.

The comparison indicates that coarser meshes produce significant deviations from the experimental measurements. Refining the mesh from 0.05 m to 0.03 m and subsequently to 0.01 m leads to progressively improved predictions of scour depth evolution and better agreement with the experimental data. A satisfactory match is obtained with the 0.01 m grid resolution. Further refinement to 0.0075 m increases computational cost substantially, while only marginal improvement in accuracy is observed. Therefore, a grid resolution of 0.01 m is considered sufficient for simulating local scour around a cylindrical pier under steady-current conditions.

To provide a quantitative assessment, the root-mean-square error (RMSE) between the experimental and numerical maximum scour depths was computed as:

$$\mathrm{RMSE} = \sqrt{\frac{1}{n}\sum_{i=1}^{n}(y_i - \hat{y}_i)^2} \qquad (20)$$

where $y_i$ represents the experimental values from Link (2006) and $\hat{y}_i$ denotes the corresponding numerical predictions. As shown in Figure 3, the RMSE decreases consistently with mesh refinement from 0.05 m to 0.01 m. The results confirm that the 0.01 m grid resolution provides an optimal balance between computational efficiency and predictive accuracy. For this grid, the corresponding $y^+$ value is approximately 175, which lies within the recommended range of 30–300 for wall-function-based turbulence modelling.

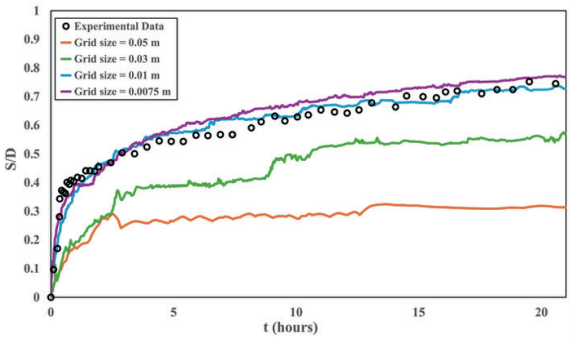


Figure 2. Convergence study showing the time evolution of the maximum scour depth around a vertical pier under steady-current conditions, compared with experimental data from Link (2006).

## 4.2 *Pier scour under steady current conditions*

In this section, the scour results obtained using the selected grid resolution of 0.01 m are presented in detail. The simulation required approximately 4.5 hours of wall-clock time to reproduce 21 hours of physical scour development, using 512 processors in parallel.

Figure 4 shows that, for an approaching flow velocity of 0.3 m/s, the velocity increases to approximately 0.43 m/s on both sides of the pile. This acceleration is caused by flow contraction due to the obstruction created by the pier. In contrast, the horizontal velocity decreases to approximately −0.14 m/s in the wake region downstream of the pier, primarily due to the shielding effect of the structure. Flow separation and the formation of wake vortices are clearly visible in Figure 4.

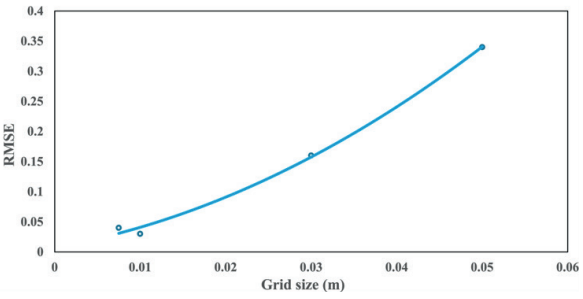


Figure 3. Root-mean-square error (RMSE) between numerical and experimental maximum scour depth for different grid resolutions.

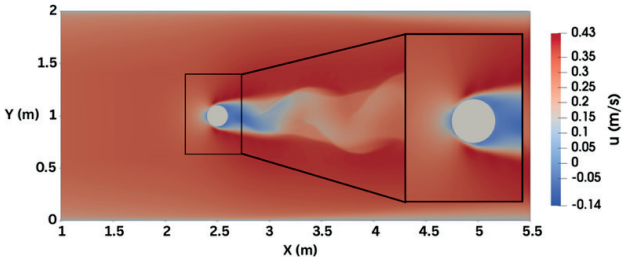


Figure 4. Contours of simulated horizontal velocity, $u$ (m/s), around the pile at $T = 21\,h$.

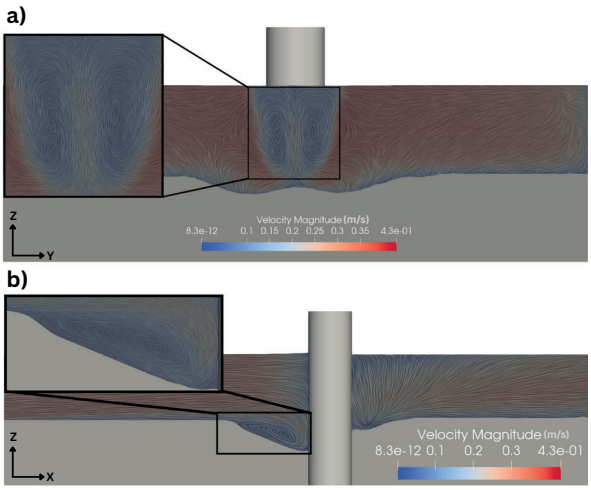


Figure 5. (a) Formation of counter-rotating vortices downstream of the pile; (b) horseshoe vortex upstream of the pile and velocity magnitude around the cylinder $(m/s)$.

Figure 5a illustrates the formation of counter-rotating vortices downstream of the pier, which enhance near-bed turbulence, while Figure 5b shows the horseshoe vortex upstream of the pier generated by the adverse pressure gradient at the bed. These results demonstrate that the numerical model is capable of accurately capturing the complex three-dimensional flow structure and separation phenomena around the pier.

Consistent with the experimental observations, the simulated temporal evolution of scour indicates that the initial maximum scour depth develops at the sides of the pier and subsequently migrates toward the upstream face. Figure 6 presents the measured scour depth contours reported by Link (2006) after 21 hours of testing. The maximum scour depth is located at the upstream face of the pier and measures 0.153 m. The corresponding simulated bed elevation from REEF3D at $T$ = 21 h is shown in Figure 7. The predicted maximum scour depth reaches 0.145 m, which is in close agreement with the experimental value.

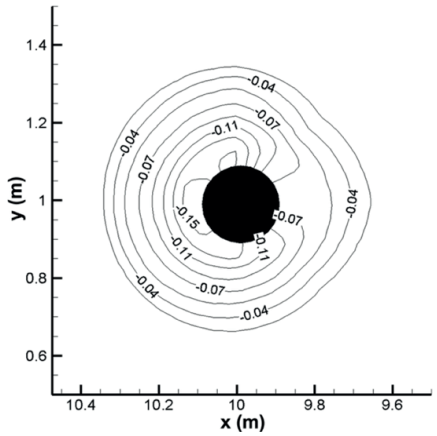


Figure 6. Experimental bed elevation contours at $T = 21$ h, with flow from left to right, as in Bihs (2011).

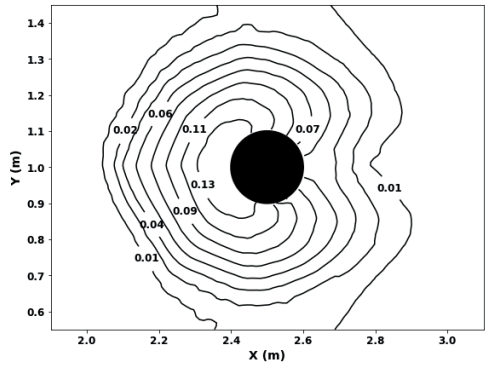


Figure 7. Numerical bed elevation contours at T = 21 h.

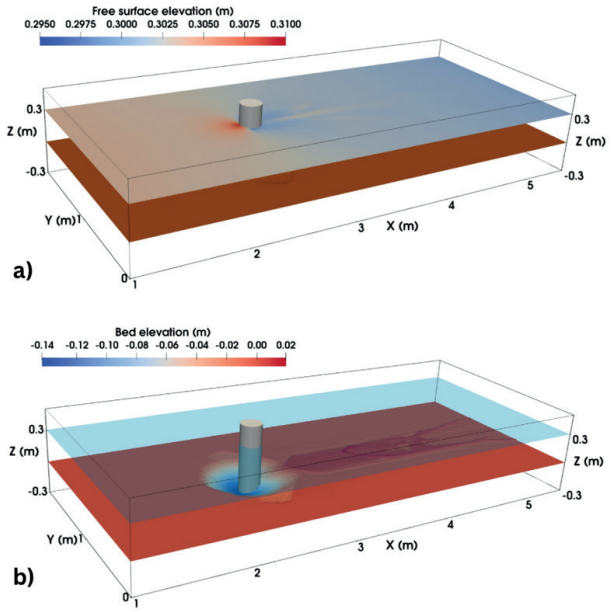


Figure 8. Three-dimensional simulated scour under steady-current conditions at $T = 21$ h: (a) free-surface elevation and (b) bed elevation.

The dynamically captured free surface, computed using the level set method, is presented together with the bed topography in Figure 8. The figure illustrates the fully three-dimensional numerical results at the end of the simulation ($T = 21\ h$).

## 5 CONCLUSIONS

In this study, a three-dimensional sediment transport module implemented in REEF3D was used to simulate local scour around a cylindrical pier under steady-current conditions using a direct-forcing immersed boundary approach. A mesh convergence study was conducted to determine the optimal grid resolution. The results indicate that a grid size of 0.01 m provides an appropriate balance between numerical accuracy and computational efficiency.

The simulated scour pattern and the temporal evolution of the maximum scour depth were validated against experimental measurements. The comparison demonstrates that the numerical model is capable of accurately reproducing the complex hydrodynamic processes and associated morphological changes in the vicinity of hydraulic structures.

Furthermore, the results confirm that the use of a decoupled hydrodynamic–morphological approach is an effective strategy for reducing the substantial computational cost associated with fully coupled three-dimensional scour simulations.

## ACKNOWLEDGEMENTS

The authors acknowledge funding from the European Union (ERC, PARTRES, Grant No. 101045646). The views and opinions expressed are solely those of the authors and do not necessarily reflect those of the European Union or the European Research Council Executive Agency. Neither the European Union nor the granting authority can be held responsible for them. The simulations were performed on the supercomputer Betzy, provided by UNINETT Sigma2 – the National Infrastructure for High-Performance Computing and Data Storage in Norway.

## REFERENCES

Afzal, S., Bihs, H., Kamath, A., Arntsen, Ø.A., (2015). Three-dimensional numerical modeling of pier scour under current and waves using level-set method. Journal of Offshore Mechanics and Arctic Engineering 137, 032001.

Ahmad, N., Afzal, S., Bihs, H., Arntsen, Ø.A., (2015). Three-dimensional numerical modeling of local scour around a non-slender cylinder under varying wave conditions, in: 36th IAHR world Congress.

Ahmad, N., Bihs, H., Myrhaug, D., Kamath, A., Arntsen, Ø.A., (2018). Three-dimensional numerical modelling of wave-induced scour around piles in a side-by-side arrangement. Coastal Engineering 138, 132–151.
Ashby, S.F., Falgout, R.D., (1996). A parallel multigrid preconditioned conjugate gradient algorithm for groundwater flow simulations. Nuclear science and engineering 124, 145–159.
Baykal, C., Sumer, B.M., Fuhrman, D.R., Jacobsen, N.G., Fredsøe, J., (2015). Numerical investigation of flow and scour around a vertical circular cylinder. Philosophical Transactions of the Royal Society A: Mathematical, Physical and Engineering Sciences 373, 20140104.
Baykal, C., Sumer, B.M., Fuhrman, D.R., Jacobsen, N.G., Fredsøe, J., (2017). Numerical simulation of scour and backfilling processes around a circular pile in waves. Coastal Engineering 122, 87–107.
Bihs, H., (2011). Three-dimensional numerical modeling of local scouring in open channel flow (Doctoral dissertation).
Bihs, H., Kamath, A., Chella, M.A., Aggarwal, A., Arntsen, Ø.A., (2016). A new level set numerical wave tank with improved density interpolation for complex wave hydrodynamics. Computers & Fluids 140, 191–208.
Bihs, H., Olsen, N.R.B., (2008). Three dimensional numerical modeling of pier scour, in: Fourth International Conference on Scour and Erosion, ICSE 4, Tokyo, Japan.
Bihs, H., Olsen, N.R.B., (2011). Numerical modeling of abutment scour with the focus on the incipient motion on sloping beds. Journal of Hydraulic Engineering 137, 1287–1292.
Burkow, M., Griebel, M., (2016). A full three dimensional numerical simulation of the sediment transport and the scouring at a rectangular obstacle. Computers & Fluids 125, 1–10.
Chorin, A.J., (1968). Numerical solution of the navier-stokes equations. Mathematics of computation 22, 745–762.
Engelund, F., Fredsøe, J., (1976). A sediment transport model for straight alluvial channels. Hydrology Research 7, 293–306.
Fleit, G., Baranya, S., Ehlers, R., Bihs, H., 2023. Cfd modeling of flow and local scour around submerged bridge decks. Journal of Coastal and Hydraulic Structures 3.
Fredsoe, J., Deigaard, R., (1992). Mechanics of coastal sediment transport. volume 3. World scientific publishing company.
Fredsoe, J., Sumer, B.M., (2002). The mechanics of scour in the marine environment. volume 17. World Scientific Publishing Company.
Gautam, S., Dutta, D., Bihs, H., Afzal, M.S., 2021. Three-dimensional computational fluid dynamics modelling of scour around a single pile due to combined action of the waves and current using level-set method. Coastal Engineering 170, 104002.
Graf, W., Istiarto, I., (2002). Flow pattern in the scour hole around a cylinder. Journal of Hydraulic Research 40, 13–20.
Griebel, M., Dornseifer, T., Neunhoeffer, T., (1998). Numerical simulation in fluid dynamics: a practical introduction. SIAM.
Jiang, G.S., Peng, D., (2000). Weighted eno schemes for hamilton–jacobi equations. SIAM Journal on Scientific computing 21, 2126–2143.
Jiang, G.S., Shu, C.W., (1996). Efficient implementation of weighted eno schemes. Journal of computational physics 126, 202–228.
Kamath, A., Fleit, G., Bihs, H., 2019. Investigation of free surface turbulence damping in rans simulations for complex free surface flows. Water 11, 456.
Larkermani, E., Bihs, H., Winckelmans, G., Duponcheel, M., Martin, T., Mu¨ller, B., Georges, L., (2024). Development of an accurate central finite-difference scheme with a compact stencil for the simulation of unsteady incompressible flows on staggered orthogonal grids. Computer Methods in Applied Mechanics and Engineering 428, 117117.
Larkermani, E., Bihs, H., Winckelmans, G., Mu¨ller, B., Georges, L., (2025). High-fidelity explicit large eddy simulations of airflows inside buildings using the immersed boundary method and orthogonal grids. Physics of Fluids 37.
Link, O., (2006). Untersuchung der kolkung an einem schlanken zylindrischen pheiler in sandigem boden. PhD thesis. Institut fr Wasserbau und Wasserwirtschaft, Technische Universitt Darmstadt.
Liu, X., Garc´ıa, M.H., (2008). Three-dimensional numerical model with free water surface and mesh deformation for local sediment scour. Journal of waterway, port, coastal, and ocean engineering 134, 203–217.
Olsen, N.R., Kjellesvig, H.M., (1998). Three-dimensional numerical flow modeling for estimation of maximum local scour depth. Journal of Hydraulic Research 36, 579–590.
Olsen, N.R., Melaaen, M.C., (1993). Three-dimensional calculation of scour around cylinders. Journal of Hydraulic Engineering 119, 1048–1054.
Paola, C., Voller, V.R., (2005). A generalized exner equation for sediment mass balance. Journal of Geophysical Research: Earth Surface 110.
Peng, D., Merriman, B., Osher, S., Zhao, H., Kang, M., (1999). A pde-based fast local level set method. Journal of computational physics 155, 410–438.
Roulund, A., Sumer, B.M., Fredsøe, J., Michelsen, J., (2005). Numerical and experimental investigation of flow and scour around a circular pile. Journal of Fluid mechanics 534, 351–401.
Shields, A., (1936). Application of similarity principles and turbulence research to bed-load movement. Technical Report. Soil Conservation Service.
Shu, C.W., Osher, S., (1988). Efficient implementation of essentially non-oscillatory shock-capturing schemes. Journal of computational physics 77, 439–471.
Soydan, A., Wang, W.W., Bihs, H., (2024a). An improved direct forcing immersed boundary method with integrated mooring algorithm for floating offshore wind turbines. Journal of Offshore Mechanics and Arctic Engineering 147, 042101.
Soydan, A., Wang, W.W., Bihs, H., (2025). An improved direct forcing immersed boundary method for floating body simulations in waves. Applied Ocean Research 158, 104523.
Sussman, M., Smereka, P., Osher, S., (1994). A level set approach for computing solutions to incompressible two-phase flow. Journal of Computational physics 114, 146–159.
Van der Vorst, H.A., (1992). Bi-cgstab: A fast and smoothly converging variant of bi-cg for the solution of nonsymmetric linear systems. SIAM Journal on scientific and Statistical Computing 13, 631–644.
Wilcox, D., (1994). Turbulence modeling for cfd, dcw industries, inc., 460 p.
Zanke, U., Roland, A., Wurpts, A., (2023). The reason for the rise in critical shear stress on sloping beds. Water 15, 2976.

DOI: https://doi.org/10.53256/COSE_250104

# MODELING OF DIFFRACTION AROUND BREAKWATERS USING THE THREE-DIMENSIONAL NON-HYDROSTATIC SOLVER REEF3D::NHFLOW

Thomas Becker[a,*], Widar Weizhi Wang[a] and Hans Bihs[a]
[a]*Norwegian University of Science and Technology (NTNU), Norway, thomas.becker@ntnu.no, widar.w.wang@ntnu.no, hans.bihs@ntnu.no*

[*]*Corresponding author*

ABSTRACT: The effectiveness of breakwaters in attenuating wave energy is largely determined by the wave heights attained leeward of the structures relative to the incoming waves. To simulate diffraction around breakwaters—both as an isolated phenomenon and under realistic site conditions—the phase-resolving, three-dimensional, non-hydrostatic model REEF3D::NHFLOW is presented. The model is validated against the analytical solution for monochromatic wave diffraction around a fully rigid, slender, semi-infinite breakwater derived by Penney and Price (1952), based on the classical Sommerfeld solution. Validation is performed through direct comparison of the simulated diffraction coefficients in the lee of the structure and their spatial distribution with the analytical reference solution. In addition, the model is applied to simulate extreme wave conditions propagating into Sirevåg Harbour, Norway, which is protected by a large breakwater. The resulting wave characteristics are compared with phase-averaged wave propagation computed using the spectral wave model SWAN, which inherently cannot accurately resolve diffraction processes. The predicted diffraction coefficients obtained with NHFLOW show good agreement with the Sommerfeld solution, yielding a root-mean-square error of 0.012 relative to the analytical diffraction coefficients. In the Sirevåg Harbour case, NHFLOW predicts greater energy dissipation as waves propagate toward the breakwater opening compared with the spectral model. However, significant wave heights inside the harbour basins are notably higher in NHFLOW, indicating that more wave energy is diffracted into these sheltered areas. This suggests that the phase-resolving model provides more physically realistic and potentially more conservative estimates of wave conditions within protected harbour zones.

KEYWORDS: Coastal hydrodynamics, harbor design, Sommerfeld solution, computational fluid dynamics

## 1 INTRODUCTION

Diffraction describes the propagation of wave energy perpendicular to the principal direction of wave travel, toward regions of lower wave energy. This process results in the bending of wave fronts into sheltered areas, for example into the lee of breakwaters. Particularly within harbour basins, diffraction is a critical mechanism influencing wave penetration, spatial energy redistribution, and wave attenuation (cf. Dean and Dalrymple, 1991; US Army Corps of Engineers, 2008).

Early analytical descriptions of diffraction were developed in optics, where wave crests were conceptualised as arrays of spherical point sources, as proposed by Huygens (1690) and later refined to account for directionality by Fresnel (1819). Subsequent formulations by Sommerfeld (1896), for diffraction by a semi-infinite screen, and by Sieger (1908), followed by Morse and Rubenstein (1938), for diffraction through slits in infinite screens, employed geometric expansions of Maxwell's equations to derive analytical solutions for diffraction coefficients.

These theoretical approaches were later adapted to water waves by Penney and Price (1952) and Carr and Stelzriede (1952), who applied analogous solution techniques to the linearised potential flow equations governing surface gravity waves. However, these analytical solutions are restricted to waves of small steepness propagating over a horizontal bed with constant still-water depth. In addition, they assume idealised, infinitely thin, fully reflective breakwaters.

In the present study, the water-wave Sommerfeld solution formulated by Penney and Price (1952)

is used to validate diffracted wave fields simulated with the three-dimensional, non-hydrostatic numerical model REEF3D::NHFLOW.

In practical applications, diffraction around breakwaters is rarely an isolated phenomenon and typically occurs in conjunction with other wave transformation processes. Wave conditions in the lee of breakwaters depend not only on the incident sea state, but also on local bathymetry, structural geometry, and additional site-specific parameters. To account for this complexity, the performance of breakwater designs may be assessed through scaled physical model tests or through high-fidelity numerical simulations capable of resolving dispersive wave characteristics and nonlinear wave transformation processes (cf. Goda, 2000; US Army Corps of Engineers, 2008). In this study, NHFLOW is applied to simulate an extreme sea state at Sirevåg Harbour in Rogaland, Norway. The resulting wave conditions inside the harbour are compared with those obtained from an equivalent simulation using the spectral wave model SWAN.

## 2 THEORY

### 2.1 *The Sommerfeld Solution for Water Waves*

The Sommerfeld solution for water waves was derived by Penney and Price (1952) for an infinitely thin, semi-infinite breakwater, with its tip located at $x = 0$and $y = 0$in a local horizontal coordinate system, as illustrated in Fig. 1. The diffraction coefficient, $k_{diff} = H_{diff} / H_{inc}$, relates the incident wave height $H_{inc}$ to the diffracted wave height $H_{diff}$ at an arbitrary point in the domain. The coefficient is evaluated based on the polar coordinates of the point of interest, for a given wave incidence angle and wavelength $L$.

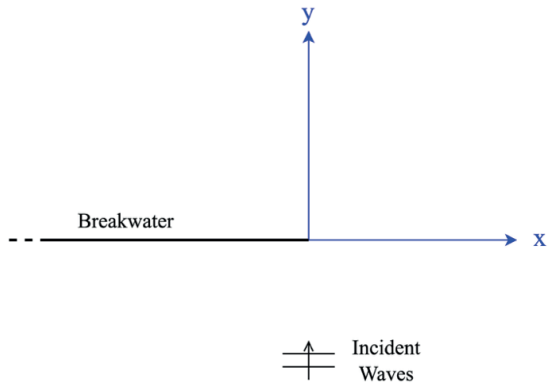


Figure 1. Geometric configuration used in the Sommerfeld solution (breakwater at $x \leq 0$; perpendicular wave incidence)

The solution is obtained by imposing additional no-flow and constant-pressure boundary conditions at the breakwater onto the classical Airy wave solution. The resulting boundary-value problem becomes tractable through the application of Sommerfeld's (1896) method, which extends the solution space using a Riemann surface formulation. The Sommerfeld solution accounts for incident and reflected wave components, their diffraction around the breakwater tip, and the interference patterns arising from their superposition in different regions of the spatial domain.

An excerpt of the solution in the lee of the breakwater ($y \geq 0$) is shown in Fig. 2.

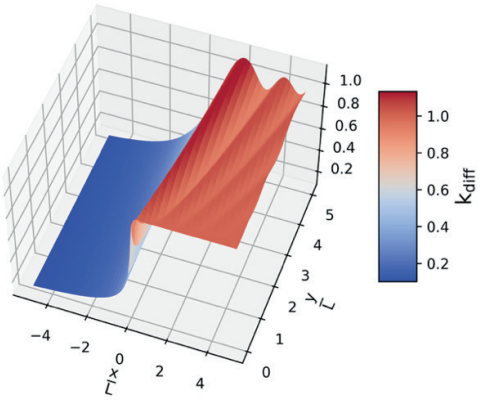


Figure 2. Sommerfeld solution for the diffraction coefficient $k_{diff}$ in the lee of a semi-infinite breakwater located at $y = 0$and $x \leq 0$ (coordinates normalised by the wavelength $L$) for perpendicular wave incidence

### 2.2 *REEF3D::NHFLOW*

NHFLOW (Bihs et al., 2024, Bihs and Wang, 2025) is one of four numerical models currently available within the open-source software framework REEF3D. Its development was preceded by a high-resolution Navier–Stokes model (Bihs et al., 2016), a non-hydrostatic shallow water equation solver (Wang et al., 2020), and a fully nonlinear potential flow model (Wang et al., 2022), each designed for different applications in water wave modelling. NHFLOW combines high-fidelity flow-field computation with large-scale applicability across a wide range of water depths and complex bathymetries.

NHFLOW solves the three-dimensional Euler equations for mass and momentum conservation (Eqs. 1 and 2), where $u$ denotes the velocity vector, $h$ the water depth, $\rho$ the water density, $p$ the pressure, and $g$ the gravitational acceleration. Viscous terms may be included in the momentum equation to extend the formulation to the full Navier–Stokes equations; however, they are not considered in the present study.

$$\frac{\partial u_i}{\partial x_i} = 0 \quad (1)$$

$$\frac{\partial hu_i}{\partial t} + u_j \frac{\partial hu_i}{\partial x_j} + \frac{h}{\rho}\frac{\partial p_i}{\partial x_i} + hg_i = 0 \quad (2)$$

The non-hydrostatic pressure field is computed using a pressure-correction method.
The governing equations are solved for the water phase on a rectilinear grid. The vertical coordinate $z$, defined over an arbitrarily shaped seabed, is transformed into a terrain-following $\sigma$-coordinate system, with relative spacing between the seabed $z_b$and the free surface $d + \eta$(where $d$is the still water depth and $\eta$ the free-surface elevation), as defined in Eq. 3. This transformation is updated at each time step after the free-surface position in the Cartesian coordinate system $(d + \eta)$ is advanced through horizontal mass-flux integration over the water column.

$$\sigma = \frac{z - z_b}{d + \eta - z_b} \quad (3)$$

For local conservation and shock-capturing capability, a finite-difference method with a Godunov-type scheme is employed, incorporating an approximate Riemann solver and WENO flux reconstruction (Jiang and Shu, 1996). Time integration is performed using adaptive time stepping based on a prescribed Courant–Friedrichs–Lewy (CFL) number and a second-order total variation diminishing (TVD) Runge–Kutta scheme (Gottlieb and Shu, 1998).
Solitary waves, monochromatic waves, and spectral wave conditions can be generated using prescribed wave-maker boundary profiles, Dirichlet boundary conditions, or relaxation zones following Jacobsen et al. (2012). Similarly, outlet boundary conditions may include active wave absorption or relaxation zones.
The model incorporates a wetting–drying algorithm for wave run-up, based on a water-depth threshold controlling the dynamic extension of the computational domain. Bihs and Wang (2025) demonstrate that the combined shock-capturing and wetting–drying schemes reproduce experimental observations of wave breaking and run-up with good accuracy.
By solving the Euler equations and representing bathymetry and structures as no-flux boundaries, NHFLOW inherently captures wave reflection and diffraction processes. This capability was validated for the case of Mehamn Harbor, Norway, by Bihs and Wang (2025).
For further details on the numerical framework and its positioning relative to other wave models, the reader is referred to Bihs and Wang (2025).

### 2.3 *SWAN*

The third-generation, fully spectral wave model SWAN (Simulating WAves Nearshore; Booij et al., 1999) solves the wave-action balance equation (Eq. 4) for the wave-action density $N$(defined as $N = E/f$, where $E$is the wave energy density of a given wave component and $f$its intrinsic frequency) using a second-order finite-difference scheme:

$$\frac{\partial N}{\partial t} + \frac{\partial (c_g + u)_i N}{\partial x_i} + \frac{\partial c_f N}{\partial f} + \frac{\partial c_\theta N}{\partial \theta} = \frac{S_{tot}}{\sigma} \quad (4)$$

Wave action is advected in physical space by the group velocity $c_g$, and in the spectral domains of frequency $f$ and direction $\theta$ by the propagation velocities $c_f$ and $c_\theta$, which primarily account for Doppler shifting and refraction, respectively. The term $S_{tot}$ represents the sum of source and sink terms, including nonlinear wave–wave interactions, bottom friction, and wave breaking. Wind input is not considered in the present study.

Because SWAN is based on phase-averaged wave-action propagation, it allows the use of coarser spatial grids compared with phase-resolving models such as NHFLOW. However, the frequency and directional dimensions must be resolved as additional spectral coordinates. SWAN supports various grid types (e.g., curvilinear grids), although only rectilinear grids are employed in this work.
Wave spectra can be prescribed at the domain boundaries using Dirichlet boundary conditions. Beaches and sheltered domain boundaries without incoming wave energy are typically represented using free-propagation (Neumann-type) boundary conditions. Consequently, wave reflection is not inherently resolved in SWAN.
A phase-decoupled diffraction approximation was introduced by Holthuijsen et al. (2003), yielding reasonable results for idealised cases such as the Sommerfeld solution. In practical applications involving full frequency spectra, however, this approach is applicable only to obstacles with negligible reflection and is explicitly not recommended for large breakwaters or harbour configurations.

## 3 VALIDATION FOR THE SOMMERFELD SOLUTION

### 3.1 *Validation Methodology*

To reproduce the Sommerfeld solution numerically, a computational setup was developed to generate, propagate, and absorb

waves around a vertical, slender breakwater. The configuration is illustrated in Fig. 3. A relaxation-zone scheme is applied for both wave generation and absorption, effectively minimising reflections of incident, reflected, and diffracted waves. At the lateral boundaries not affected by diffracted waves, symmetry-plane (Cauchy-type) boundary conditions are imposed. A Cartesian grid is employed, with equal spatial discretisation in the horizontal directions (Δx = Δy). Due to grid constraints, the minimum feasible breakwater thickness of 3Δx is adopted.

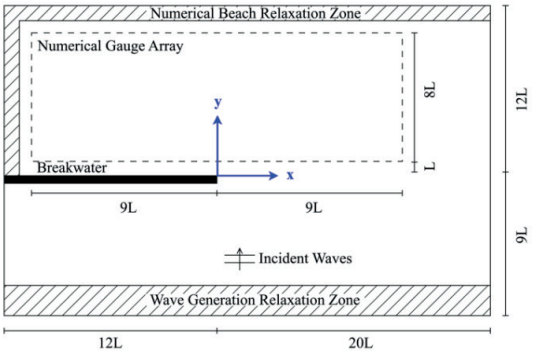


Figure 3. Numerical domain setup for the Sommerfeld validation case in NHFLOW (not to scale; dimensions relative to the incident wavelength $L$)

For wave generation, a monochromatic, long-crested incident wave field is prescribed with wave height $H = 0.2$ m and wavelength $L = 10$ m. Waves propagate over a constant still-water depth $d = 6$ m, ensuring deep-water conditions and preventing bottom effects from influencing the results. The incident wave height is verified in the fully developed region upstream of the breakwater using a numerical wave gauge positioned outside the reflection zone and analysed through a down-crossing method.

To compare the numerically obtained diffracted wave heights with the analytical Sommerfeld solution, an array of 37 × 9 numerical wave gauges is placed in the lee of the breakwater. The surface elevation time series are analysed using the down-crossing method, and the corresponding diffraction coefficients $k_{\mathrm{diff}}$ are computed and compared with analytical values at each gauge location.

The gauges are distributed along the x-axis in increments of 0.5L, spanning from $x = -9L$ to $x = 9L$, and centred about the y-axis. Along the y-axis, gauges are positioned from $y = 1L$ to $y = 9L$ in increments of 1L (see Fig. 3). Model performance is evaluated using the root-mean-square error (RMSE) of $k_{\mathrm{diff}}$ over the gauge array, as well as the mean relative deviation. Simulations are run for 240 s, and diffracted wave heights are extracted from $t = 210$ sonward to ensure a fully developed wave field.

The horizontal grid resolution is set to Δx = Δy = 0.15 m, and adaptive time stepping is applied with a Courant–Friedrichs–Lewy number of CFL = 0.5. To assess the sensitivity of the results to vertical resolution, additional simulations are conducted with varying numbers of grid layers in the vertical σ-coordinate. A hyperbolic stretching transformation is applied to the normalised σ-coordinates $\sigma_{i,\mathrm{norm}}$, mapping them to the physical vertical coordinate $z_i$ between the seabed ($z = 0$) and the free surface ($z = d + \eta$), according to:

$$z_i = (d + \eta)\frac{\sinh[\xi(\sigma_{i,\mathrm{norm}} - 1)] + \sinh(\xi)}{\sinh(\xi)} \qquad (5)$$

where the stretching factor is set to $\xi = 2.5$.

## 3.2 *Validation Results*

The recreated Sommerfeld solution is simulated in NHFLOW using 3, 5, 7, 10, and 12 σ-layers. The resulting wave field obtained with 12 σ-layers is shown in Fig. 4. Table 1 summarises the mean relative deviation of the diffraction coefficients averaged over all 333 numerical gauges, $\Delta k_{\mathrm{diff,mean}}$, and the corresponding root-mean-square error, $\mathrm{RMSE}_{k_{\mathrm{diff}}}$.

While $\Delta k_{\mathrm{diff,mean}}$ is sensitive to the magnitude of the analytical diffraction coefficients (which decrease rapidly toward zero in the sheltered region lee of the breakwater), the RMSE provides a measure of the absolute accuracy of the reproduced wave heights in the numerical model.

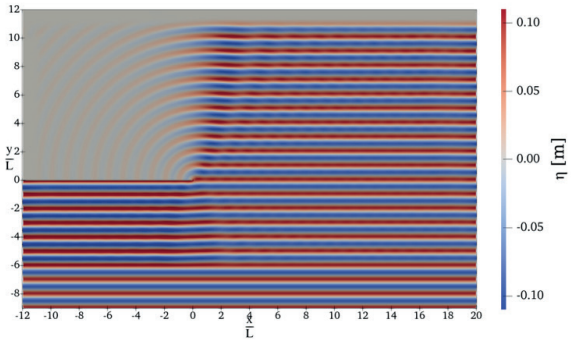


Figure 4. Water level elevation $\eta$ in the Sommerfeld case as simulated with NHFLOW (12 σ-layers)

Table 1. Mean relative diffraction coefficient deviation $\Delta k_{\mathrm{diff,mean}}$ and root-mean-square error $\mathrm{RMSE}_{k_{\mathrm{diff}}}$ for different vertical resolutions.

| σ-layers | $\Delta k_{\mathrm{diff,mean}}$ [%] | $\mathrm{RMSE}_{k\mathrm{diff}}$ [-] |
|---|---|---|
| 3 | 11.82 | 0.0573 |
| 5 | 7.39 | 0.0187 |
| 7 | 6.51 | 0.0132 |
| 10 | 6.22 | 0.0120 |
| 12 | 6.14 | 0.0118 |

These results are illustrated in Fig. 5 and show continuous convergence with increasing numbers of σ-layers. The asymptotic behaviour is approximately quantified by applying a least-squares fit of a convergence function to $\Delta k_{\mathrm{diff,mean}}$ as a function of the normalised vertical grid spacing (inverse number of σ-layers). Following the procedure proposed by Eça and Hoekstra (2014), an approximate convergence order of 2.85 is obtained. Richardson extrapolation to an infinitely fine discretisation yields a projected residual value of $\Delta k_{\mathrm{diff,mean}} = 6.02\%$, with a 95% confidence interval range of 0.10 percentage points. The results obtained with 12 σ-layers lie marginally outside this narrow confidence interval and may therefore be considered sufficiently converged. The corresponding RMSE of $k_{\mathrm{diff}}$ is 0.012.

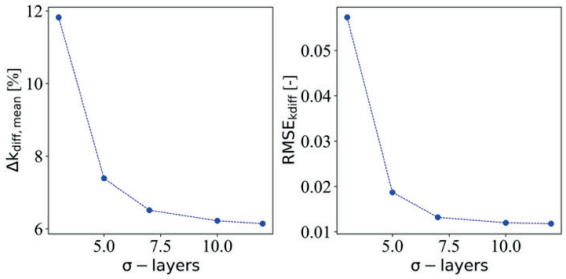


Figure 5. Mean relative diffraction coefficient deviation $\Delta k_{\mathrm{diff,mean}}$ and root-mean-square error $\mathrm{RMSE}_{k_{\mathrm{diff}}}$ as a function of vertical resolution

To assess the spatial reproduction of the diffraction coefficients and qualitatively evaluate the agreement, the individual gauge results are compared with the analytical Sommerfeld solution in Fig. 6.

The results demonstrate very good qualitative agreement with the spatial distribution predicted by the analytical solution. However, diffraction coefficients in the sheltered region (x < 0) are slightly underpredicted by the numerical model.

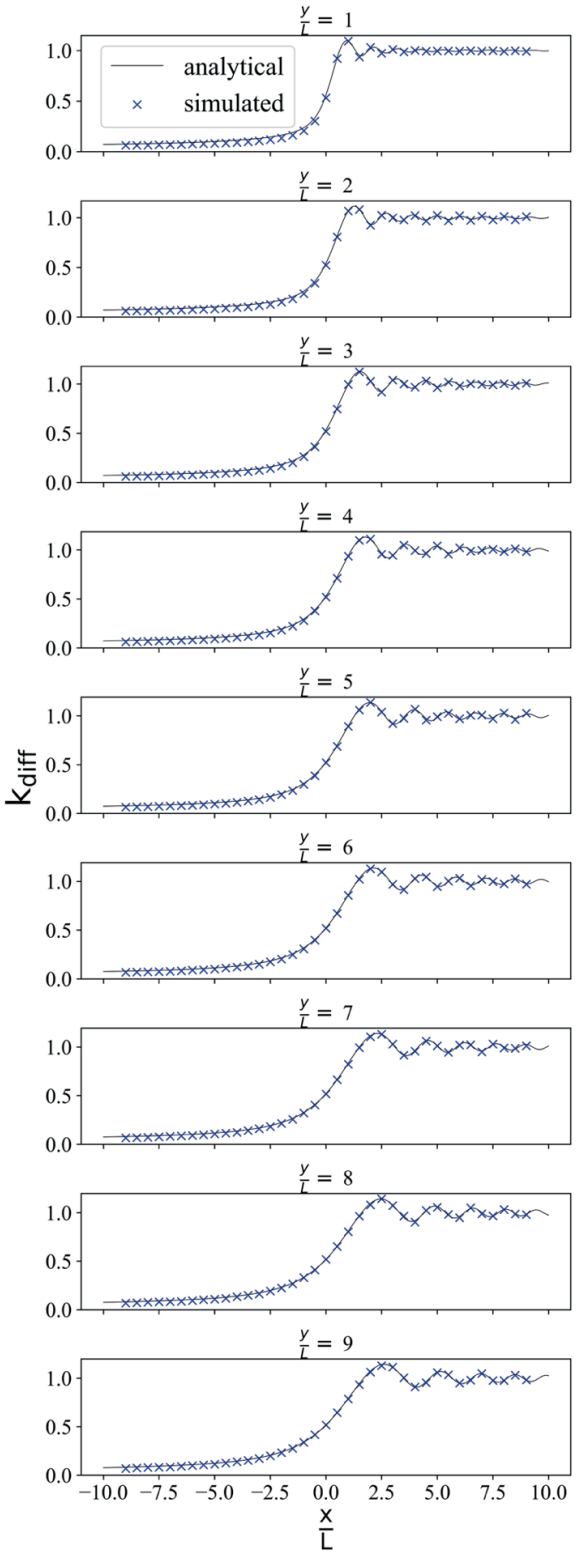


Figure 6. Diffraction coefficients $k_{\mathrm{diff}}$at numerical wave gauges for 12 σ-layers (blue) compared with the analytical Sommerfeld solution (black)

The combination of a small RMSE and a comparatively larger $\Delta k_{\mathrm{diff,mean}}$ indicates that most of the relative error originates in the strongly sheltered region, where $k_{\mathrm{diff}}$ is small. To investigate this further, four subsets of the numerical gauge array (18 gauges each) are analysed individually for the 12-layer simulation. For both the sheltered region (x < 0) and the exposed region (x > 0) lee of the breakwater, gauges located at y = 1L and y = 9L are considered separately. The resulting values of $\Delta k_{\mathrm{diff,mean}}$ and $\mathrm{RMSE}_{k_{\mathrm{diff}}}$ are summarised in Table 2. The deviations from the analytical solution are larger in the sheltered region (x < 0), where wave energy results solely from diffraction under perpendicular wave incidence. In contrast, the exposed region (x > 0) is influenced by interference between incident, reflected, and diffracted waves (Penney and Price, 1952), resulting in smaller relative deviations.

Furthermore, gauges located farther from the breakwater tip (y = 9L) show closer agreement with the analytical solution than those closer to it (y = 1L). This behaviour is interpreted as a consequence of the geometric discrepancy between the analytical and numerical representations of the breakwater.

In the analytical model, the obstacle is infinitely thin and exhibits a mathematical singularity at its tip. In contrast, the numerical representation employs a finite breakwater thickness of 3Δx, and the singularity at the tip does not exist. The observed discrepancies are therefore attributed primarily to this geometric approximation rather than to deficiencies in the numerical wave propagation scheme.

Table 2. Mean relative diffraction coefficient deviations $\Delta k_{\mathrm{diff,mean}}$ and root-mean-square errors $\mathrm{RMSE}_{\mathrm{kdiff}}$ in the gauge subsets for 12 σ-layers

| | $\Delta k_{\mathrm{diff,mean}}$ [%] | | $\mathrm{RMSE}_{\mathrm{kdiff}}$ [-] | |
|---|---|---|---|---|
| | **x < 0** | **x > 0** | **x < 0** | **x > 0** |
| **y = 1L** | 17.87 | 0.66 | 0.0222 | 0.0083 |
| **y = 9L** | 7.22 | 0.51 | 0.0090 | 0.0067 |

# 4 HARBOR APPLICATION CASE

## 4.1 *Modelling of Diffraction in Sirevåg Harbor with NHFLOW and SWAN*

To reproduce the bathymetry of Sirevåg Harbor in a numerical model, a digital elevation model (DEM) of the area was obtained from publicly available data provided by the Norwegian Mapping Authority (Kartverket). The dataset was further processed by manually correcting missing elevation values above the shoreline. The emerged sections of the main breakwater protecting the harbor were manually reconstructed based on the cross-sectional specifications reported by Sigurdarson et al. (2003), with particular attention to berm slopes and crest elevations.

To define the input wave spectrum, spectral hindcast data from the nearest offshore grid point (lon: 5.7608°, lat: 58.4902°) in NORA3 (Norwegian Reanalysis Archive 3), provided by the Norwegian Meteorological Institute (Haakenstad et al., 2021; Breivik et al., 2022), were analysed for the period between May 2023 and May 2024 to identify the most extreme sea state. The selected extreme conditions are: Significant wave height: $H_s = 7.13$m; Peak period: $T_p = 14.86$s; Mean wave direction: $\theta_m = 294.95°$(nautical convention)

The water level is set to mean sea level, and tidal effects as well as storm surge are neglected. Although this simplification would influence results in a full risk-assessment context, it is considered acceptable here for the purpose of comparing wave propagation and diffraction patterns simulated by the two models.

The selected sea state is simulated in both NHFLOW and SWAN using a rotated computational domain of 2120 m × 2070 m, oriented such that $\theta_m$ is aligned with the x-axis (Fig. 7). A uniform horizontal grid with $\Delta x = \Delta y = 5$m is applied in both models.

In NHFLOW, five σ-layers are used for vertical discretisation, with hyperbolic stretching applied as described in Section 3.1.

Six numerical wave gauges are placed at identical locations in both models (see Fig. 7 and Table 3). These positions are selected to sample: (1) Incident wave conditions offshore; (2) Propagated wave conditions approaching the harbor; (3) Wave conditions near the breakwater head at the harbor entrance; (4) The lee side of the main breakwater; (5) The first harbor basin; (6) The marina area at the rear of the second harbor basin, separated by a secondary breakwater

In both models, wave boundary conditions are prescribed only at the offshore boundary (x = 0 m). In NHFLOW, this is implemented via a relaxation zone. Absorption relaxation zones are applied at the lateral boundaries.

In SWAN, free-propagation (radiation) boundary conditions are imposed at the lateral boundaries.

A total simulation time of 12,600 s is performed in NHFLOW. The frequency spectrum at each gauge location is reconstructed using a Fast Fourier Transform (FFT), and significant wave heights $H_s$ are computed from the zero-moment wave height. A spin-up period of 1,800 s is allowed for the development of the wave field

before sampling the free-surface elevation $\eta$for spectral analysis.
In SWAN, the spectrum is imposed as a stationary boundary condition. Consequently, the model is executed in stationary mode (i.e. the unsteady term $\partial N / \partial t$ in Eq. 4 is omitted).
In SWAN, $H_s$ is extracted directly from the spectral solution at each grid point. The spatial distributions of $H_s$are plotted over the full domain for qualitative comparison between the models.
At gauge position 1, the simulated spectra from both models are matched by fitting to a JONSWAP spectrum (following Goda, 1988) to ensure comparable incident wave conditions. This step is necessary because the extreme wave parameters are expected to interact nonlinearly with the relatively shallow bathymetry.
At the remaining gauge positions, the computed $H_s$ values from NHFLOW and SWAN are compared quantitatively to assess differences in simulated wave propagation and diffraction into the harbor.

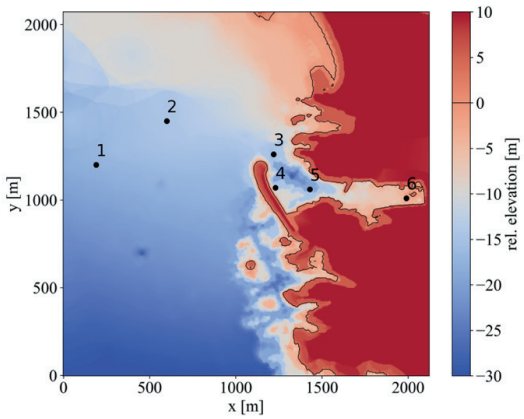


Figure 7. Computational domain showing bathymetry relative to still water level (0 m, positive upward) and the six numerical wave gauge locations

### 4.2 *Model Comparison in the Harbor Application Case*

Analysis of the simulated time series at the incident wave gauge (Gauge 1; see Fig. 7) in NHFLOW yields a JONSWAP spectrum with $H_s = 5.82\text{m}$ and $T_p = 14.86\text{s}$. The fully developed wave field is shown in Fig. 8, and the spatial distribution of significant wave heights over the full computational domain is presented in Fig. 9.
The same spectral parameters are imposed in SWAN, achieving a parameter convergence greater than 99.5%. The resulting significant wave heights are shown in Fig. 10. For improved comparison of wave conditions within the harbor, close-up views of the significant wave height distributions are provided in Fig. 11 (NHFLOW) and Fig. 12 (SWAN).

Table 3 lists the significant wave heights at the six gauge locations (see Fig. 7), allowing for quantitative comparison between the two models. The domain-wide significant wave height distributions show broadly similar large-scale behaviour in both models. In both cases, wave refraction over the bathymetry results in convergence and divergence patterns toward the shoreline. However, clear differences in wave-field representation are evident. NHFLOW exhibits standing wave patterns near solid boundaries and along the shoreline, whereas SWAN produces characteristic wave-ray patterns. These differences are also apparent at the breakwater opening and within the harbor basins.
At Gauge 2, substantial differences arise in the predicted wave propagation toward the shoreline. NHFLOW predicts considerably less wave energy at this location compared to SWAN. This discrepancy may be related to differences in the treatment of refraction and wave attenuation processes (e.g. depth-induced breaking and whitecapping) in SWAN, compared with the phase-resolved, shock-capturing formulation in NHFLOW. The effect is particularly pronounced because Gauge 2 is located near a zone of wave divergence. A similar trend is observed at Gauge 3, near the breakwater opening, where SWAN predicts higher wave energy than NHFLOW.
Despite these differences offshore of the breakwater, the models' treatment of diffraction becomes critical inside the harbor. Significant wave heights predicted in the lee of the breakwater (Gauges 4–6) are substantially higher in NHFLOW than in SWAN. In the first harbor basin (Gauge 5), the ratio between NHFLOW and SWAN results is approximately 2.3. In the second basin (Gauge 6), the ratio increases to 16.3.
These differences are consistent with the fact that diffraction-driven wave energy propagation is not accurately represented in SWAN. As shown in Fig. 12, the spectral model produces wave-energy rays inside the harbor similar to those in the refraction-dominated nearshore zone. These rays diverge toward the harbor walls, where energy is effectively dissipated due to the absence of wave reflection in the model formulation. The small amount of wave energy reaching the innermost harbor basin (Gauge 6) may result from minor ray penetration combined with numerical dispersion effects (cf. Holthuijsen et al., 2003).
In contrast, NHFLOW (Fig. 11) produces a smoother and more physically consistent distribution of wave energy within the harbor basins, including standing wave patterns generated by reflection and diffraction at structural boundaries. This results in significantly

higher and more conservative wave height predictions in sheltered areas.

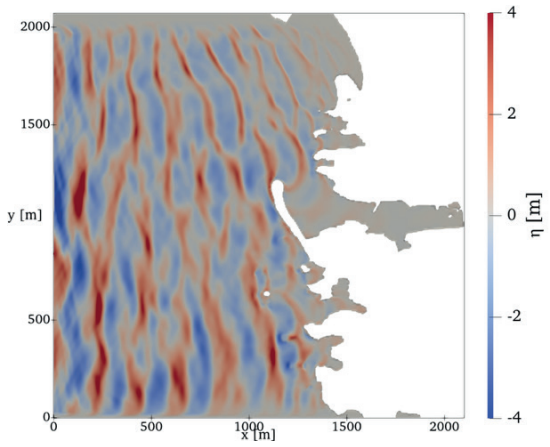


Figure 8. Water surface elevation $\eta$ simulated with NHFLOW for the Sirevåg harbor case (t = 5400s)

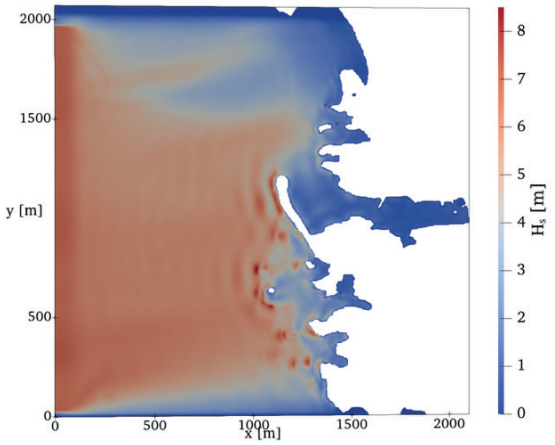


Figure 9. Significant wave heights $H_s$ simulated with NHFLOW for the Sirevåg harbor case (FFT over 3 hours)

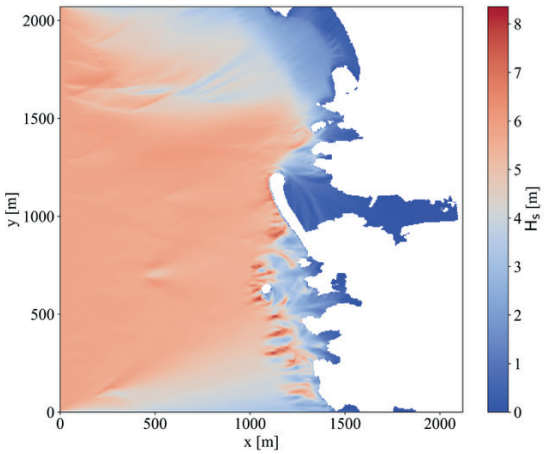


Figure 10. Significant wave heights $H_s$ simulated with SWAN for the Sirevåg harbor case (stationary model)

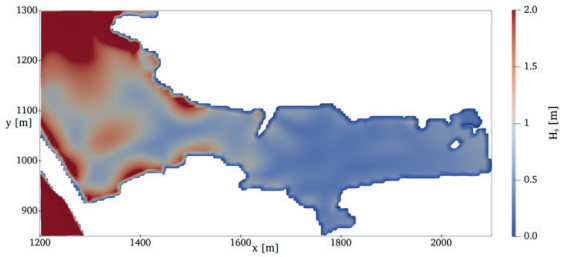


Figure 11. Harbor close-up of significant wave heights $H_s$ simulated with NHFLOW (FFT over 3 hours)

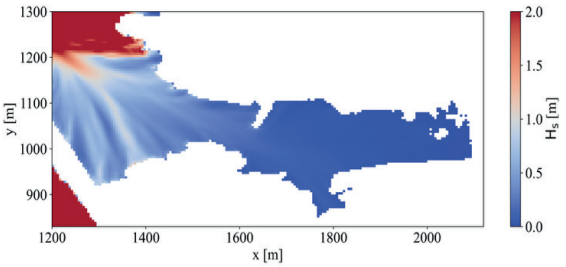


Figure 12. Harbor close-up of significant wave heights $H_s$ simulated with SWAN (stationary solution)

Table 3. Wave gauge coordinates and significant wave heights $H_s$ in NHFLOW and SWAN (relative difference expressed as SWAN vs. NHFLOW)

| Gauge No. | Pos x [m] | Pos y [m] | $H_s$ NHFLOW [m] | $H_s$ SWAN [m] | Relative Difference [%] |
|---|---|---|---|---|---|
| 1 | 190 | 1200 | 5.82 | 5.82 | 0 |
| 2 | 600 | 1450 | 4.96 | 5.48 | +10.48 |
| 3 | 1220 | 1260 | 2.56 | 3.06 | +19.53 |
| 4 | 1230 | 1070 | 1.28 | 0.48 | –62.50 |
| 5 | 1430 | 1060 | 0.75 | 0.32 | –57.33 |
| 6 | 1990 | 1010 | 0.49 | 0.03 | –93.88 |

## 5 CONCLUSIONS

Although an infinitely thin obstacle cannot presently be represented exactly in NHFLOW, the model reproduces the Sommerfeld solution of Penney and Price (1952) with high accuracy. An RMSE of 0.012 for the diffraction coefficients in the lee of a slender breakwater is achieved (using high vertical resolution) relative to the analytical solution. Most of the relative error occurs at locations where the diffraction coefficients are small, i.e. in strongly sheltered regions.

A practical application of diffraction modelling with NHFLOW is demonstrated for the Sirevåg harbor case. When matched wave spectra are imposed, NHFLOW predicts less wave energy

reaching the breakwater opening compared to the spectral wave model SWAN. However, the significant wave heights within the harbor basins are substantially higher in NHFLOW, and the resulting wave patterns exhibit more physically consistent spatial distributions than those obtained with SWAN. These findings indicate that the phase-resolving model NHFLOW provides more conservative and physically realistic predictions of wave conditions inside sheltered harbor areas.

Overall, this study demonstrates the high accuracy of REEF3D::NHFLOW in modelling diffraction processes and highlights its capability to resolve combined refraction–diffraction–reflection interactions in wave propagation toward and within harbor environments.

## ACKNOWLEDGEMENTS

The authors acknowledge funding from the European Union (ERC, PARTRES, 101045646). The views and opinions expressed are those of the authors only and do not necessarily reflect those of the European Union or the European Research Council Executive Agency. Neither the European Union nor the granting authority can be held responsible for them.

The simulations were performed on the supercomputer Betzy, provided by Sigma2 – the National Infrastructure for High-Performance Computing and Data Storage in Norway.

## REFERENCES

Bihs, H., Ehlers, R., Wang, W. (2024). A shock-absorbing non-hydrostatic navier-stokes solver on σ-grids for wave modeling over irregular topography. *OMAE 43 proceedings vol. 6*

Bihs, H., Kamath, A., Alagan Chella, M., Aggarwal, A., Arntsen, Ø.A. (2016). A new level set numerical wave tank with improved density interpolation for complex wave hydrodynamics. *Computers & Fluids 140*: 191–208.

Bihs, H., Wang, W.W. (2025). REEF3D::NHFLOW–A high-performance non-hydrostatic solver for coastal wave propagation. *Coastal Engineering 202*.

Booij, N., Ris, R.C., Holthuijsen, L.H. (1999). A third-generation wave model for coastal regions: 1. model description and validation. *J. Geophys. Res. 104*: 7649–7666.

Breivik, Ø., Carrasco, A., Haakenstad, H., Aarnes, O.J., Behrens, A., Bidlot, J., Björkqvist, J., Bohlinger, P., Furevik, B.R., Staneva, J., Reistad, M. (2022). The impact of a reduced high-wind Charnock parameter on wave growth with application to the North Sea, the Norwegian Sea, and the Arctic Ocean. *JGR Oceans 127*.

Carr, J.H., Stelzriede, M.E. (1952). Diffraction of water waves by breakwaters. *U.S. Nat. Bur. Stds 521*: 109–125.

Dean, R.G., Dalrymple, R.A. (1991). Water Wave Mechanics for Engineers and Scientists, 2nd ed. World Scientific.

Eça, L., Hoekstra, M. (2014). A procedure for the estimation of the numerical uncertainty of CFD calculations based on grid refinement studies. *Journal of Computational Physics 262: 104–130*.

Fresnel, A.-J. (1819). Mémoire sur la diffraction de la lumière [Memoir on the diffraction of light]. *Mémoires de l'Académie des Sciences de l'Institut de France 5*: 339–475.

Goda, Y. (1988). Statistical variability of sea state parameters as a function of wave spectrum. *Coastal Engineering in Japan 31*: 39–52.

Goda, Y. (2000). Random seas and design of maritime structures, 2nd ed. World Scientific.

Gottlieb, S., Shu, C.-W. (1998). Total variation diminishing Runge-Kutta schemes. *Math. Comp. 67*: 73–85.

Haakenstad, H., Breivik, Ø., Furevik, B.R., Reistad, M., Bohlinger, P., Aarnes, O.J. (2021). NORA3: A nonhydrostatic high-resolution hindcast of the North Sea, the Norwegian Sea, and the Barents Sea. *Journal of Applied Meteorology and Climatology 60*: 1443–1464.

Holthuijsen, L.H., Herman, A., Booij, N. (2003). Phase-decoupled refraction–diffraction for spectral wave models. *Coastal Engineering 49*: 291–305.

Huygens, C. (1690). Traité de la lumière [Treatise on light]. Chez Pierre van der Aa.

Jacobsen, N.G., Fuhrman, D.R., Fredsøe, J. (2012). A wave generation toolbox for the open-source CFD library: OpenFoam®. *Numerical Methods in Fluids 70*:1073–1088.

Jiang, G.-S., Shu, C.-W. (1996). Efficient implementation of weighted ENO schemes. *Journal of Computational Physics 126*: 202–228.

Kartverket. Norwegian national elevation model [Høydedata]. Retrieved April 17, 2025.

Morse, P.M., Rubenstein, P.J. (1938). The Diffraction of Waves by Ribbons and by Slits. *Phys. Rev. 54*: 895–898.

Norwegian Meteorological Institute. NORA3 - Norwegian reanalysis archive 3 [nora3_wave]. Retrieved March 25, 2025.

Penney, W.G., Price, A.T. (1952). Part I: The diffraction theory of sea waves and the shelter afforded by breakwaters. *Phil. Trans. R. Soc. Lond. A 244*: 236–253.

Sieger, B. (1908). Die Beugung einer ebenen electrischen Welle an einem Schirm von elliptischem Querschnit [Diffraction of a plane electric wave at a screen with eliptic cross section]. *Ann. Phys. 27*: 626–664.

Sigurdarson, S., Jacobsen, A., Smarason, O.B., Bjørdar, S., Viggosson, G., Urrang, C., Tørum, A. (2004). Sirevåg berm breakwater, design, construction and experience after design storm. *Coastal Structures 2003 proceedings*: 1212–1224.

Sommerfeld, A. (1896). Mathematische Theorie der Diffraction [Mathematical theory of diffraction]. *Math. Ann. 47*: 317–374.

United States Army Corps of Engineers (2008). Coastal engineering manual part II: Coastal hydrodynamics. U.S. Dept. of Transportation.

Wang, W., Martin, T., Kamath, A., Bihs, H. (2020). An improved depth-averaged nonhydrostatic shallow water model with quadratic pressure approximation. *Numerical Methods in Fluids 92*: 803–824.
Wang, W., Pákozdi, C., Kamath, A., Fouques, S., Bihs, H. (2022). A flexible fully nonlinear potential flow model for wave propagation over the complex topography of the Norwegian coast. *Applied Ocean Research 122*: 103103.

DOI: https://doi.org/10.53256/COSE_250105

# Numerical Simulation of Large-Element Interaction Using Coupled CFD–DEM in REEF3D

Elyas Larkermani[a,*], Ahmet Soydan[a], Alexander T. Hanke[a], Widar W. Wang[a] and Hans Bihs[a]
[a]*Department of Civil and Environmental Engineering, Norwegian University of Science and Technology, Trondheim, Trøndelag, Norway*

[*]*Corresponding author: elyas.larkermani@ntnu.no, Byggteknisk laboratorium Gløshaugen, S-229, Trondheim, Norway*

ABSTRACT: This study presents a high-fidelity numerical framework for simulating the interaction of large, arbitrarily shaped solid elements using a coupled CFD–DEM approach in multiphase flows. The implementation is integrated into the open-source REEF3D framework and combines a high-order finite-difference Navier–Stokes solver with a Direct Forcing Immersed Boundary Method (DF-IBM) to model fluid–structure interactions on a fixed Cartesian grid. A multi-level collision detection and response algorithm is incorporated to resolve contact dynamics between large elements using a linear viscoelastic spring–dashpot model. The coupling ensures fully two-way interaction between hydrodynamic forces and rigid-body motion in six degrees of freedom (6DOF). To demonstrate the performance of the framework, a benchmark case involving the buoyant rise and collision of three rigid spheres in a water tank is simulated. The results highlight the robustness and stability of the coupling strategy in capturing complex multi-body interactions in multiphase flow conditions.

KEYWORDS: Multi-body interaction, CFD-DEM coupling, Collision detection, Multi-phase flow

## 1 INTRODUCTION

### 1.1 *Challenges in Coastal Defence Structures*

Coastal structures such as breakwaters, revetments, and seawalls constitute critical infrastructure designed to protect shorelines from wave action, erosion, and flooding (Charlier et al., 2005); Griggs (2005). Among these, rubble-mound breakwaters—constructed from layers of quarried rock and concrete armour units—represent one of the most widely adopted coastal protection solutions worldwide (Hudson, 1958; Van der Meer, 1995). The stability and performance of these structures depend on complex interactions between hydrodynamic forces and the individual elements comprising the armour layer. Despite decades of research, reliable prediction of structural damage, armour unit displacement, and progressive failure remains a significant challenge (Davies et al., 1995; Kobayashi et al., 2013; Melby & Kobayashi, 1998). Traditional design approaches rely heavily on empirical formulations derived from physical model testing. Classic examples include Hudson's equation (Hudson, 1959) and the stability formulations proposed by Van der Meer (van der Meer, 1988), which relate wave characteristics to armour unit stability through empirical coefficients. More recent formulations incorporate additional dimensionless parameters to extend their range of applicability (Kobayashi, 2015). However, these equations cannot be reliably extrapolated beyond the experimental conditions from which they were derived.

Although practical and widely used, empirical methods do not capture the detailed mechanics governing individual element displacement, rocking behaviour, and the progressive nature of damage evolution. Consequently, detailed design assessments often require laboratory-based physical model testing, where wave–structure interactions can be investigated under controlled conditions (Kramer et al., 2005). Nevertheless, scaled physical modelling presents inherent

limitations. Material properties, geometric scaling constraints, and simplified boundary conditions can hinder accurate reproduction of prototype-scale forces. These challenges have stimulated increasing interest in near-prototype-scale flume experiments, which offer improved physical fidelity. Despite their advantages, such large-scale tests remain costly and are subject to practical constraints, including construction variability and uncertainties associated with dynamic loading conditions.

### 1.2 *Numerical Modelling of Coastal Structures*

In recent years, numerical modelling (Kelly et al., 2021) has emerged as a complementary tool capable of reducing the need for extensive physical testing while providing access to quantities that are difficult to measure experimentally. The optimal design of coastal structures can be achieved through an integrated approach that combines empirical formulations, physical model testing, and high-fidelity numerical simulations. The increasing availability of computational resources has further accelerated the adoption of numerical methods, enabling high-resolution analysis of wave–structure interactions. Several modelling paradigms have emerged in this context:

#### 1.2.1 *Computational Fluid Dynamics (CFD)*

Mesh -based Computational Fluid Dynamics (CFD) methods solve the Navier–Stokes equations using finite difference (Larkermani et al., 2024), finite volume (Moukalled et al., 2016), or finite element (Löhner, 2008) discretisation approaches. Commercial and open-source frameworks such as ANSYS (Finnegan & Goggins, 2012), and OpenFOAM (Huang et al., 2022) have demonstrated strong capabilities in modelling wave–structure interactions. However, these methods often encounter difficulties when addressing the complex geometries and moving boundaries associated with granular materials such as rock armour layers (Shinde et al., 2022).

#### 1.2.2 *Discrete Element Methods (DEM)*

Discrete Element Method (DEM) is a computational approach for modelling the motion and interaction of individual solid bodies (Cundall & Strack, 1979). DEM tracks individual particles through explicit time integration of Newton's laws of motion. It can accurately capture inter-particle collisions and frictional contact behaviour. Nevertheless, DEM simulations become computationally demanding when large numbers of elements are considered, particularly in engineering-scale applications.

#### 1.2.3 *Smoothed Particle Hydrodynamics (SPH)*

Smoothed Particle Hydrodynamics (SPH) and other meshless methods represent the system state using a collection of Lagrangian particles, which naturally accommodate complex geometries and free-surface flows (Shi et al., 2016). Each particle carries physical properties such as velocity, pressure, and mass, and interacts with neighbouring particles through smoothing kernels. Despite their flexibility, these approaches remain computationally intensive for large-scale engineering problems and may suffer from numerical diffusion and challenges in the accurate enforcement of boundary conditions.

Coupled approaches combining CFD and DEM have emerged as promising techniques for resolving fluid–solid interaction, leveraging the complementary strengths of each method (Jing et al., 2016; Mao et al., 2020; Nan et al., 2022; Zhao & Shan, 2013). Most previous CFD–DEM coupling strategies have focused on fluid–particle systems such as landslides, debris flows, or sediment transport. These approaches often rely on simplified particle geometries, unstructured meshing strategies, or computationally expensive shape representations.

In contrast, the present study introduces a resolved CFD–DEM framework specifically developed for the simulation of large, arbitrarily shaped elements subjected to hydrodynamic loading. The coupling is implemented within the REEF3D solver using a high-order finite difference scheme on a fixed Cartesian grid, combined with a Direct Forcing Immersed Boundary Method (DF-IBM) to capture fluid–structure interaction without mesh deformation or remeshing. This configuration enables accurate and numerically stable simulations of large-scale element motion and contact under wave action, effectively bridging the gap between high-resolution CFD modelling and realistic rigid-body dynamics in coastal engineering applications.

## 2 NUMERICAL METHODOLOGY

### 2.1 *Overview of the Numerical Framework*

The numerical framework is implemented in the REEF3D CFD software (Bihs et al., 2016), and extended with dedicated modules for collision handling. The overall architecture comprises five main components: (1) the CFD solver, (2) free surface capturing, (3) the immersed boundary method for representing arbitrarily complex structures, (4) six degrees of freedom rigid body motion, and (5) the collision detection and response algorithm. These components operate in

a fully coupled manner to accurately resolve the dynamic interaction between the fluid and multiple solid elements.

### 2.2 Hydrodynamic Solver (REEF3D::CFD)

REEF3D::CFD employs a structured Cartesian grid to solve the incompressible Navier–Stokes equations:

$$\frac{\partial u_i}{\partial x_i} = 0 \tag{1}$$

$$\frac{\partial u_i}{\partial t} + \frac{\partial u_i u_j}{\partial x_j} = -\frac{1}{\rho_0}\frac{\partial p}{\partial x_i} + \frac{\partial}{\partial x_j}\left[\upsilon\left(\frac{\partial u_i}{\partial x_j} + \frac{\partial u_j}{\partial x_i}\right)\right] + g_i \tag{2}$$

where $x_i$denotes the $i$-th spatial coordinate, $u_i$is the velocity component in the $x_i$ direction, $p$ is the pressure field, $\rho_0$ the reference density, $t$ time, $g_i$ the gravitational acceleration, and $\nu$the kinematic viscosity.
Spatial discretisation is performed using a high-order Weighted Essentially Non-Oscillatory (WENO) scheme (Jiang & Shu, 1996), which provides sharp resolution of flow features while minimising numerical diffusion. Temporal discretisation is achieved using a third-order Total Variation Diminishing (TVD) Runge–Kutta scheme to ensure stability and accuracy in transient simulations (Gottlieb & Shu, 1998).

### 2.3 Free-Surface Treatment

The free surface is captured using the level-set method, which represents the water–air interface as the zero level set of a signed distance function $\phi_s$ (Osher & Sethian, 1988). The interface evolution is governed by:

$$\frac{\partial \varphi_s}{\partial t} + u_j \frac{\partial \varphi_s}{\partial x_j} = 0 \tag{3}$$

The level-set function is periodically reinitialised to preserve its signed-distance property (Sussman et al., 1994).

### 2.4 Direct Forcing Immersed Boundary Method

Fluid–structure interaction is modelled using the Direct Forcing Immersed Boundary Method (DF-IBM) (Soydan et al., 2025). Operating within a one-fluid formulation of the Navier–Stokes equations (Yang, 2018), the method introduces a body-force term into the momentum equation to enforce the no-slip boundary condition at the fluid–solid interface (Larkermani et al., 2025).

$$\frac{\partial u_i}{\partial t} + \frac{\partial u_i u_j}{\partial x_j} = -\frac{1}{\rho_0}\frac{\partial p}{\partial x_i} + f_i \tag{4}$$

The forcing term $f_i$ is computed explicitly at each time step as:

$$f_i = \frac{u_i^d - u_i^n}{\Delta t} \tag{5}$$

where $u_i^d$ denotes the desired (rigid-body) velocity and $u_i^d$ the intermediate fluid velocity. Each immersed object is represented by a triangulated surface. A local signed-distance function determines whether a computational point lies within the fluid ($\varphi_s > 0$) or solid ($\varphi_s < 0$) region.
This forcing term is smoothly distributed near the interface using a smoothed Heaviside function to avoid numerical discontinuities (Soydan et al., 2024). This approach allows arbitrarily complex geometries to be embedded in the Cartesian grid without mesh deformation.
Hydrodynamic forces and moments are obtained by integrating pressure and viscous stresses over the immersed surface:

$$F_i = \oint_S (-p\delta_{ij} + \tau_{ij}) n_j dS \tag{6}$$

$$M_i = \oint_S \epsilon_{ijk} r_j (-p\delta_{kl} + \tau_{kl}) n_l dS \tag{7}$$

where $\delta_{ij}$ is the Kronecker delta, $\tau_{ij}$ is the viscous stress tensor, $n_j$ is the surface normal, $r_j$ is the position vector relative to the element's center of mass, and $\epsilon_{ijk}$ is the permutation symbol.

### 2.5 Six-Degree-of-Freedom Rigid-Body Motion

The motion of each solid object is determined by solving Newton's second law for both translational and rotational motion:

$$m\frac{d\boldsymbol{u}}{dt} = \boldsymbol{F}_{hydro} + \boldsymbol{F}_{collision} + m\boldsymbol{g} \tag{8}$$

$$\boldsymbol{I}\frac{d\boldsymbol{\omega}}{dt} + \boldsymbol{\omega} \times (\boldsymbol{I}\boldsymbol{\omega}) = \boldsymbol{M}_{hydro} + \boldsymbol{M}_{collision} \tag{9}$$

where $m$ is mass, $\boldsymbol{I}$ is the moment of inertia tensor, $\boldsymbol{\omega}$ is the angular velocity. The subscripts 'hydro' and 'collision' denote hydrodynamic and contact contributions, respectively. Rotational motion is formulated in a body-fixed coordinate system using Euler parameters. The position and orientation of each element are advanced in time using the same explicit Runge–Kutta scheme as the fluid solver (Martin et al., 2021; Shivarama & Fahrenthold, 2004).

## 2.6 Collision Detection and Response Algorithm

### 2.6.1 Multi-Level Collision Detection

Collision detection proceeds through multiple levels of increasing accuracy and computational cost. First, a spatial partitioning strategy (Golshan et al., 2023) divides the computational domain into grid cells, each tracking intersecting objects. Then, for each potential collision pair identified through spatial partitioning, an initial rapid overlap test is performed using bounding spheres to eliminate pairs of objects that cannot possibly be in contact. Each element is assigned a precomputed bounding radius $R$ that encloses its entire geometry with a small safety margin. Potential overlap is determined by comparing the distance between the object centres $c$ with the sum of their bounding radii.

This spatial hashing technique reduces the computational complexity of collision detection by restricting collision checks to objects located within neighbouring cells, using a two-step contact detection strategy (Golshan et al., 2023). At each time step, the spatial grid is updated to reflect the current positions of all objects prior to collision detection.

If the bounding spheres overlap, the penetration depth is computed as:

$$\delta = R_1 + R_2 - |\boldsymbol{c}_2 - \boldsymbol{c}_1| \tag{10}$$

and the contact normal is defined based on the object centres:

$$\boldsymbol{n} = \frac{\boldsymbol{c}_2 - \boldsymbol{c}_1}{|\boldsymbol{c}_2 - \boldsymbol{c}_1|} \tag{11}$$

### 2.6.2 Contact Force Model

The collision module implements several contact force formulations based on the soft-sphere DEM approach used in Lethe (Golshan et al., 2023). Although the framework supports both linear viscoelastic (Hookean) and nonlinear viscoelastic (Hertz–Mindlin) formulations (El-Emam et al., 2021), the present study employs the linear viscoelastic model due to its computational efficiency and numerical robustness.

In the linear spring–dashpot model, the normal contact force is proportional to the overlap distance (spring contribution) and the relative normal velocity (damping contribution):

$$\mathbf{F}_n = \left(k_n \delta_n + \gamma_n u_{rel,n}\right)\mathbf{n} \tag{12}$$

where $k_n$ is the normal stiffness coefficient, $\delta_n$ is the penetration depth, $\gamma_n$ is the normal damping coefficient, and $\mathbf{n}$ is the contact normal vector. In the numerical implementation, the normal force is constrained to be purely repulsive by enforcing $\max(\mathbf{F}_n, 0)$.

### 2.6.3 Tangential Force Components

Tangential forces are computed based on the relative tangential velocity at the contact point and are limited by the Coulomb friction criterion (El-Emam et al., 2021; Fonte et al., 2015; Vivacqua et al., 2019):

$$\mathbf{F}_t = \min\left(\mu|\mathbf{F}_n|, \left|k_t \delta_t + \gamma_t u_{rel,t}\right|\right) \cdot \mathbf{t} \tag{13}$$

where $\mu$ is the friction coefficient, $k_t$ is the tangential stiffness, $\delta_t$ is the accumulated tangential displacement since contact initiation, $\gamma_t$ is the tangential damping coefficient, and $\mathbf{t}$ is the tangential unit vector.

## 2.7 Coupling with Hydrodynamic Forces

The collision algorithm in REEF3D is tightly integrated with the DF-IBM and the 6DOF rigid-body motion solver to ensure accurate two-way coupling between the fluid and solid phases.

At each time step, the following sequence of operations is performed (see Figure *1* for a flowchart of the algorithm):

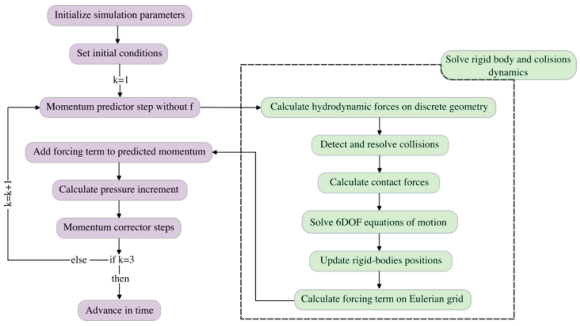


Figure 1. Flowchart of the coupled CFD–DEM algorithm implemented in REEF3D

First, incompressible Navier–Stokes equations are solved to compute the hydrodynamic forces and moments acting on each immersed object. Potential collisions between rigid bodies and/or boundaries are identified using a grid-based broad-phase search, followed by a fine-scale mesh-level intersection check. Contact forces and moments arising from these interactions are evaluated. Next, and contact contributions are aggregated to obtain the total force and moment acting on each element. The 6DOF solver then integrates the equations of motion to update the translational and rotational states of the rigid bodies. Following the motion update, the

immersed boundary forcing terms are recomputed based on the updated object positions and velocities, ensuring accurate enforcement of the no-slip boundary condition. Finally, the updated geometries are projected onto the fluid grid to maintain consistent boundary representation for the subsequent time step.

## 3 RESULTS

### 3.1 *Three-Sphere Collision in a Two-Phase Flow*

To demonstrate the capabilities of the coupled CFD–DEM algorithm implemented in the REEF3D framework for simulating complex multi-body interactions, a benchmark case involving the buoyant rise and subsequent collision of three rigid spheres in a two-phase (air–water) environment is considered.
This test case is designed to evaluate the accuracy of the collision detection and response algorithm, the robustness of the fluid–structure coupling, and the model's ability to capture free-surface dynamics during multi-body interactions.

### 3.2 *Setup*

The computational domain consists of a rectangular tank with a length of 2.0 m, a height of 1.0 m, and a width of 0.1 m. The tank is partially filled with water to a depth of 0.4 m, with the upper portion occupied by air. The air–water interface is initially defined as a sharp, horizontal surface. Gravity acts in the negative $z$-direction with $g = 9.81\ \mathrm{m\ s^{-2}}$.
Three identical rigid spheres, each with a radius $R = 0.02$ mand a density $\rho_s = 900\ \mathrm{kg\ m^{-3}}$, are positioned along the vertical centreline of the tank. Sphere 1 is initially placed at the air–water interface, floating partially submerged. Sphere 2 is fully submerged and located directly below Sphere 1, with a vertical offset of 0.1 m. Sphere 3 is positioned a further 0.1 m below Sphere 2, as illustrated in Figure 2(a).
The domain is discretised using a uniform Cartesian grid with a resolution of $\Delta x = \Delta y = \Delta z = 0.01$ m, resulting in approximately 200,000 grid cells. No-slip boundary conditions are applied at the left, right, and bottom walls. Symmetry boundary conditions are imposed at the front and back boundaries, as well as at the top boundary. The air–water interface is captured using the level-set method, and the Direct Forcing Immersed Boundary Method (DF-IBM) is employed to represent the spheres on the fixed Eulerian grid.
Inter-particle contacts are resolved using a linear spring–dashpot model. The normal stiffness coefficient is set to $k_n = 1.0 \times 10^6\ \mathrm{N\ m^{-1}}$, and the normal damping coefficient to $\gamma_n = 1.0 \times 10^4\ \mathrm{N\ s\ m^{-1}}$.
Tangential (frictional) forces are modelled using a tangential stiffness $k_t = 0.5 \times 10^6\ \mathrm{N\ m^{-1}}$and a tangential damping coefficient $\gamma_t = 0.5 \times 10^4\ \mathrm{N\ s\ m^{-1}}$. These forces are limited by the Coulomb friction criterion with a friction coefficient of 0.3. The selected parameters represent typical rigid-body interactions in water and ensure numerically stable and physically realistic collision dynamics within the two-phase flow environment.

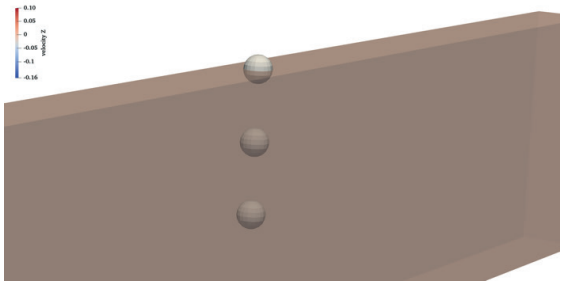
(a)$t = 0s$

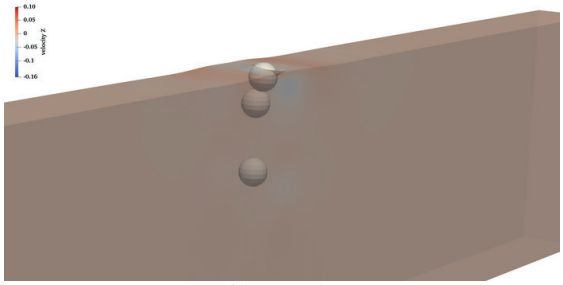
(b)$t = 0.5s$

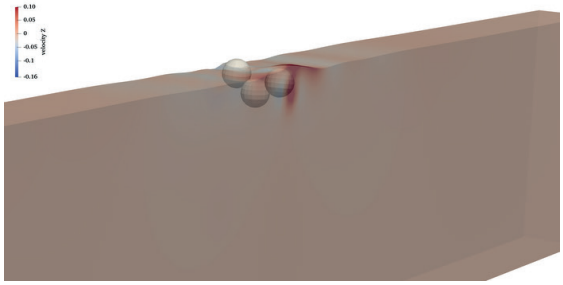
(c)$t = 1.0s$

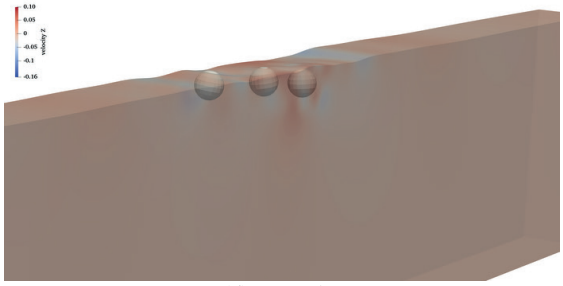
(d)$t = 1.5s$

Figure 2. Time sequence of the three-sphere collision test case in a two-phase (air–water) environment

All spheres are initially at rest (Figure 2a). Upon release, the submerged spheres experience a net upward buoyant force and begin to rise through

the water column (Figure 2b). As they accelerate upward, they interact with the surrounding fluid and eventually collide with the sphere at the surface and with each other (Figure 2c, Figure 2d).The simulation captures the kinematics and trajectories of the spheres throughout the collision events. The results demonstrate the capability of the coupled CFD–DEM framework to achieve stable and robust coupling between hydrodynamic forces and contact mechanics in a complex multi-body interaction system.

## 4 CONCLUSIONS

A fully resolved CFD–DEM coupling framework has been implemented within the REEF3D solver to simulate the hydrodynamic behaviour and collision dynamics of large rigid elements in multiphase flow. The methodology combines a high-order finite-difference CFD solver with a soft-sphere contact model, enabling robust two-way coupling between the fluid and solid phases. The framework captures both translational and rotational motion through a six-degrees-of-freedom (6DOF) rigid-body solver.

A benchmark case involving the buoyant rise and collision of three rigid spheres was simulated to evaluate the performance of the coupling algorithm in resolving contact interactions. The results demonstrate that the implemented framework can accurately reproduce momentum transfer and damping effects associated with multi-body interactions under complex hydrodynamic conditions.

Future work will focus on extending the framework to incorporate wave generation and realistic wave conditions, as well as modelling the actual geometries of rock and concrete armour units used in rubble-mound breakwaters.

## ACKNOWLEDGEMENTS

The authors acknowledge funding from the European Union (ERC, PARTRES, Grant No. 101045646). The views and opinions expressed are those of the authors only and do not necessarily reflect those of the European Union or the European Research Council Executive Agency. Neither the European Union nor the granting authority can be held responsible for them. The simulations were performed on the Betzy supercomputer provided by Sigma2 – the National Infrastructure for High-Performance Computing and Data Storage in Norway.

## REFERENCES

Bihs, H., Kamath, A., Chella, M. A., Aggarwal, A., & Arntsen, Ø. A. (2016). A new level set numerical wave tank with improved density interpolation for complex wave hydrodynamics. *Computers & Fluids*, *140*, 191–208.

Charlier, R. H., Chaineux, M. C. P., & Morcos, S. (2005). Panorama of the history of coastal protection. *Journal of Coastal Research*, *21*(1), 79–111.

Cundall, P. A., & Strack, O. D. (1979). A discrete numerical model for granular assemblies. *geotechnique*, *29*(1), 47–65.

Davies, M. H., Mansard, E. P., & Cornett, A. M. (1995). Damage analysis for rubble-mound breakwaters. In *Coastal Engineering 1994* (pp. 1001–1015).

El-Emam, M. A., Zhou, L., Shi, W., Han, C., Bai, L., & Agarwal, R. (2021). Theories and applications of CFD–DEM coupling approach for granular flow: A review. *Archives of Computational Methods in Engineering*, 1–42.

Finnegan, W., & Goggins, J. (2012). Numerical simulation of linear water waves and wave–structure interaction. *Ocean Engineering*, *43*, 23–31.

Fonte, C. B., Oliveira Jr, J., & de ALMEIDA, L. C. (2015). DEM-CFD coupling: mathematical modelling and case studies using ROCKY-DEM® and ANSYS Fluent®. Proceedings of the 11th International Conference on CFD in the Minerals and Process Industries, CSIRO, Melbourne, Australia,

Golshan, S., Munch, P., Gassmöller, R., Kronbichler, M., & Blais, B. (2023). Lethe-DEM: An open-source parallel discrete element solver with load balancing. *Computational Particle Mechanics*, *10*(1), 77–96.

Gottlieb, S., & Shu, C.-W. (1998). Total variation diminishing Runge-Kutta schemes. *Mathematics of computation*, *67*(221), 73–85.

Griggs, G. B. (2005). The impacts of coastal armoring. *Shore and beach*, *73*(1), 13–22.

Huang, L., Li, Y., Benites-Munoz, D., Windt, C. W., Feichtner, A., Tavakoli, S., Davidson, J., Paredes, R., Quintuna, T., & Ransley, E. (2022). A review on the modelling of wave-structure interactions based on OpenFOAM. *OpenFOAM® Journal*, *2*, 116–142.

Hudson, R. (1958). *Design of Quarry-stone Cover Layers for Rubble-mound Breakwaters: Hydraulic Laboratory Investigation*. Waterways Experiment Station.

Hudson, R. Y. (1959). Laboratory investigation of rubble-mound breakwaters. *Journal of the waterways and Harbors division*, *85*(3), 93–121.

Jiang, G.-S., & Shu, C.-W. (1996). Efficient implementation of weighted ENO schemes. *Journal of Computational physics*, *126*(1), 202–228.

Jing, L., Kwok, C., Leung, Y. F., & Sobral, Y. (2016). Extended CFD–DEM for free-surface flow with multi-size granules. *International journal for numerical and analytical methods in geomechanics*, *40*(1), 62–79.

Kelly, D. M., Dimakopoulos, A., & Caubilla, P. H. (2021). *Advanced numerical modelling of wave structure interaction*. CRC Press.

Kobayashi, N. (2015). Hydraulic response and armor layer stability on coastal structures. *Ocean Engineering Laboratory, University of Delaware, Newark, Delaware*.

Kobayashi, N., Pietropaolo, J., & Melby, J. A. (2013). Deformation of reef breakwaters and wave transmission. *Journal of waterway, port, coastal, and ocean engineering*, *139*(4), 336–340.

Kramer, M., Zanuttigh, B., Van der Meer, J., Vidal, C., & Gironella, F. (2005). Laboratory experiments on low-

crested breakwaters. *Coastal Engineering*, *52*(10-11), 867–885.
Larkermani, E., Bihs, H., Winckelmans, G., Duponcheel, M., Martin, T., Müller, B., & Georges, L. (2024). Development of an accurate central finite-difference scheme with a compact stencil for the simulation of unsteady incompressible flows on staggered orthogonal grids. *Computer Methods in Applied Mechanics and Engineering*, *428*, 117117.
Larkermani, E., Bihs, H., Winckelmans, G., Müller, B., & Georges, L. (2025). High-fidelity explicit large eddy simulations of airflows inside buildings using the immersed boundary method and orthogonal grids. *Physics of Fluids*, *37*(3).
Löhner, R. (2008). *Applied computational fluid dynamics techniques: an introduction based on finite element methods*. John Wiley & Sons.
Mao, J., Zhao, L., Di, Y., Liu, X., & Xu, W. (2020). A resolved CFD–DEM approach for the simulation of landslides and impulse waves. *Computer Methods in Applied Mechanics and Engineering*, *359*, 112750.
Martin, T., Tsarau, A., & Bihs, H. (2021). A numerical framework for modelling the dynamics of open ocean aquaculture structures in viscous fluids. *Applied Ocean Research*, *106*, 102410.
Melby, J. A., & Kobayashi, N. (1998). Progression and variability of damage on rubble mound breakwaters. *Journal of waterway, port, coastal, and ocean engineering*, *124*(6), 286–294.
Moukalled, F., Mangani, L., Darwish, M., Moukalled, F., Mangani, L., & Darwish, M. (2016). *The finite volume method*. Springer.
Nan, X., Hou, J., Shen, Z., Tong, Y., Li, G., Wang, X., & Kang, Y. (2022). CFD-DEM coupling with multi-sphere particles and application in predicting dynamic behaviors of drifting boats. *Ocean Engineering*, *247*, 110368.
Osher, S., & Sethian, J. A. (1988). Fronts propagating with curvature-dependent speed: Algorithms based on Hamilton-Jacobi formulations. *Journal of Computational physics*, *79*(1), 12–49.
Shi, C., An, Y., Wu, Q., Liu, Q., & Cao, Z. (2016). Numerical simulation of landslide-generated waves using a soil–water coupling smoothed particle hydrodynamics model. *Advances in Water Resources*, *92*, 130–141.
Shinde, S., Dabir, V., Khare, K., & Londhe, S. (2022). Comparison of Numerical Models for Wave Structure Interaction Studies. In *River and Coastal Engineering: Hydraulics, Water Resources and Coastal Engineering* (pp. 319–327). Springer.
Shivarama, R., & Fahrenthold, E. P. (2004). Hamilton's equations with Euler parameters for rigid body dynamics modeling. *J. Dyn. Sys., Meas., Control*, *126*(1), 124–130.
Soydan, A., Wang, W. W., & Bihs, H. (2024). An Upgraded Direct Forcing Immersed Boundary Method With Integrated Mooring Algorithm for Floating Offshore Wind Turbines. International Conference on Offshore Mechanics and Arctic Engineering,
Soydan, A., Wang, W. W., & Bihs, H. (2025). An improved direct forcing immersed boundary method for floating body simulations in waves. *Applied Ocean Research*, *158*, 104523.
Sussman, M., Smereka, P., & Osher, S. (1994). A level set approach for computing solutions to incompressible two-phase flow. *Journal of Computational physics*, *114*(1), 146–159.
van der Meer, J. W. (1988). Deterministic and probabilistic design of breakwater armor layers. *Journal of waterway, port, coastal, and ocean engineering*, *114*(1), 66–80.
Van der Meer, J. W. (1995). Conceptual design of rubble mound breakwaters. In *Advances In Coastal And Ocean Engineering: (Volume 1)* (pp. 221–315). World Scientific.
Vivacqua, V., López, A., Hammond, R., & Ghadiri, M. (2019). DEM analysis of the effect of particle shape, cohesion and strain rate on powder rheometry. *Powder technology*, *342*, 653–663.
Yang, L. (2018). One-fluid formulation for fluid–structure interaction with free surface. *Computer Methods in Applied Mechanics and Engineering*, *332*, 102–135.
Zhao, J., & Shan, T. (2013). Coupled CFD–DEM simulation of fluid–particle interaction in geomechanics. *Powder technology*, *239*, 248–258.

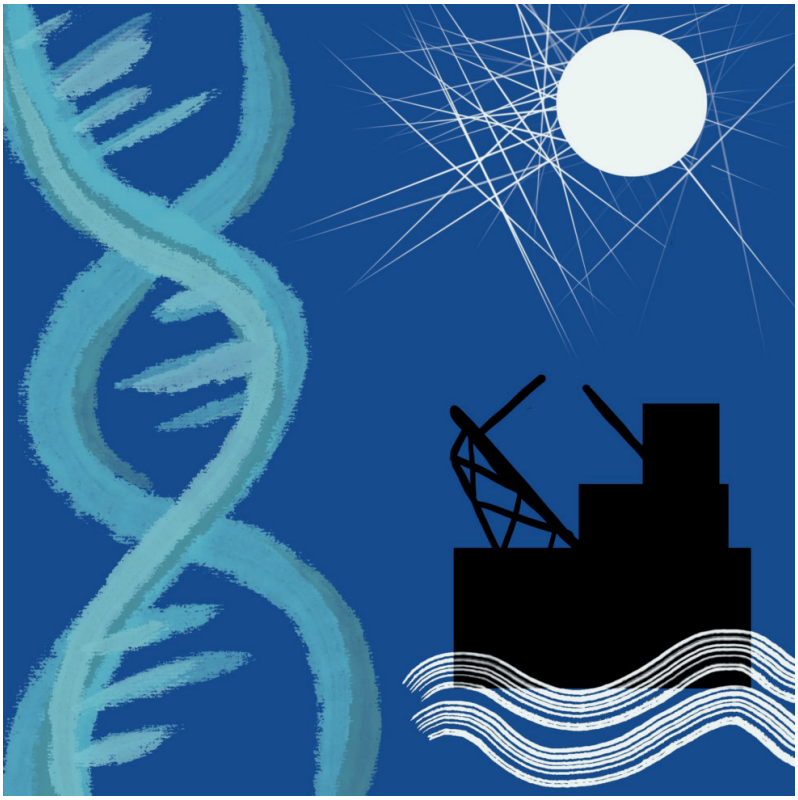

Concept:
**Stefano Pagliai**

Cover credits:
Cover image by ©**Marialuisa Sabato**

Web-site
**https://www.ecampusuniversitypress.it/riviste/coastal-and-offshore-science-and-engineering/**

Contact
**editore@uniecampus.it**

Publisher
**Studium Srl**
via Matera, 18 – 00182 – Roma
via Isimbardi, 10 – 22060 – Novedrate (CO)
www.studiumeditore.it

Registration with the Court of Como n. 2, March 7, 2022.

# Coastal and Offshore Science and Engineering

an International open-access Journal

7/2025
ISSN 2785-7972

STUDIUM EDITORE

eCAMPUS UNIVERSITÀ

eCAMPUS UNIVERSITY PRESS